# Diffusion Within Fluorite Structured Materials and the Effect of Defects

Aoife Plunkett

A thesis submitted in partial fulfillment of the requirements
for the degree of Doctor of Philosophy

at the
School of Chemistry and CRANN,
Trinity College Dublin,

Supervisor: Professor Graeme W. Watson

2018

# Declaration

I declare that this thesis has not been submitted as an exercise for a degree at this or any other university and it is entirely my own work.

I agree to deposit this thesis in the University's open access institutional repository or allow the Library to do so on my behalf, subject to Irish Copyright Legislation and Trinity College Library conditions of use and acknowledgement.

Signed: _____

Aoife Plunkett
2018

University of Dublin, Trinity College

# Summary

There is a current global movement toward renewable sources and away from non-renewable energy sources. This can be attributed to the limited resources and harmful effects, both economic and environmental, of non-renewables. In order to harness the renewable energy sources, and make their usage a feasible solution to the world's energy crisis, cheap and efficient energy conversion devices must be fabricated. The working efficiency of these devices must be improved to ensure their continued popularity and one such way to achieve this goal involves optimising the diffusion process within the multi-crystalline components.

One of the main components of an electrochemical device is the electrolyte and requires high ionic conductivity with no electronic conductivity for the device to function. The electrolyte material in many electrochemical devices has a fluorite structure, and like all materials, it contains defects, both localised and extended. These defects affect the diffusion within the material, in a manner that is not fully understood. The main motivation for the work presented in this thesis is to investigate the effect multiple defects have on the ionic diffusion within fluorite-structured materials, using molecular dynamics with a highly accurate polarisable force field.

We began by examining the diffusion properties of calcium fluoride ($CaF_2$), which was selected as a model fluorite material, due to its characteristically fast ionic diffusion. The bulk diffusion within this material was investigated to demonstrate that the method used here is capable of replicating literature results and to establish a base with which the effects of defects could be compared. Six surface orientations and seven grain boundary orientations of $CaF_2$ were investigated, and their ionic diffusion, as a function of depth, was examined for each. A peak in the diffusion, parallel to the surfaces and grain boundaries, when compared to the bulk, was observed at each surface and grain boundary, although the magnitude differed, depending on the orientation. The effect on ionic diffusion of straining the bulk system and surface slabs was investigated, as strain can be introduced into materials via lattice mismatch. An increase in tensile strain was found to increase the diffusivity of the system, while an increase in compressive strain had a detrimental effect on the ionic diffusion.

The information gained here on the structure and diffusive properties of $CaF_2$, and also the effect of defects, can be applied to other fluorite structured systems, such as in slower diffusing oxide ion materials, which are commonly used in electrochemical devices. A

popular material used for the electrolyte in these devices is yttria-stabilised zirconia (YSZ). Bulk YSZ with 8%, 10% and 12% yttria concentration were investigated. The effect of six YSZ surface orientations was compared to the bulk and to what was observed for corresponding surface orientations in $CaF_2$. Unlike $CaF_2$, most YSZ surface orientations demonstrated a decreased diffusivity at their surfaces, compared to the bulk. This was postulated to be as a result of the segregation of the charge compensating vacancies generated in YSZ. This additional layer of complexity was investigated to determine their role in the diffusion within the system. The diffusivity at the YSZ surfaces was found to be dependent on both the surface orientation and a balance between the number of $O^{2-}$ anions available for diffusion, and the number of oxygen vacancies present for these mobile anions to diffuse into.

Ionic diffusion within a material can be affected in a number of ways, and the effects must be fully understood before the diffusion process can be optimised. The knowledge of this diffusion process can then be used to generate highly efficient diffusion based electrochemical devices, that could be the answer to the world's energy crisis.

# Acknowledgements

I would like to start by thanking my supervisor, Prof. Graeme Watson, for all of the help and encouragement he has given me throughout my research. Thanks to all of the past and present members of the Watson group for making the office an enjoyable place to work: Dr. Umadevi Deivasigamani, Dr. Aoife Kehoe, Ailbhe Gavin, Aoife Lucid, Julia Savioli, Swetanshu Tandon and Douglas Temple. I would also like to thank Research IT for access to their computing facilities.

A massive thank you to my friends and family, in particular my mum, dad and sister Niamh, for their constant encouragement and confidence in me throughout my 20 years of full time education. Finally, Evan, your patience and support got me through everything, even when I thought I couldn't keep going. Thank you.

# Contents

# List of Figures

# List of Tables

# Chapter 1: Introduction

Today's scientists and engineers are faced with an ever increasing energy crisis. The U.S. Energy Information Administration predicts a 48% worldwide increase in energy demand from 2012 to 2040, with renewable sources predicted to be the world's fastest growing energy source, increasing 2.6% per year [16]. This movement toward renewable sources and away from non-renewable energy sources, such as oil, gas and coal, can be attributed to the adverse environmental and economic impact of such non-renewable sources. The emissions from these energy sources are having a severe impact on our environment, and contribute to climate change [17] and have a negative impact on human health [18]. The depletion of the non-renewable energy sources, with the limited supplies expected to be completely consumed within the next 100 years [19], has caused inflation in the cost and has triggered ongoing political turmoil. There is, therefore, a movement toward harnessing environmentally friendly power sources, such as solar, wind and geothermal, to replace these fossil fuels. This will result in an increase in demand for cheap, efficient energy conversion devices to replace those currently utilising non-renewable energy sources, that rely o the combustion of fuels.

Electrochemical fuel cells have been proposed as an answer to this issue. These fuel cells convert the chemical energy of a supplied fuel directly to electrical energy (and heat) without the use of a combustion process, and produce very little to no harmful emissions [20]. In order to ensure their future popularity, these devices must be made as cost-effective as possible. This can be done by optimising their efficiency, reducing their emissions and using cheaper, more abundant materials in their construction. Of these methods to ensure cost-effectiveness, possibly the most important is ensuring a high operating efficiency. The operation of many electrochemical devices is based on ionic diffusion, such as in solid oxide fuel cells [21–24] and gas sensors [25–30]. The diffusion process within these multi-crystalline systems, and how the presence of defects can alter the diffusion process is not well understood. This knowledge is key to unlocking the full potential of these electrochemical diffusion based devices, and for providing a viable alternative to the use of non-renewable energy sources.

## 1.1 Electrochemical Devices

### 1.1.1 Solid Oxide Fuel Cells

Solid oxide fuel cells (SOFCs) are electrochemical devices that have the ability to generate an electric current by driving ions from a porous cathode to a porous anode across a solid ceramic electrolyte [31]. These devices have seen a rise in popularity in recent years due to the depletion of fossil fuels and increasing public demand for environmentally friendly and renewable power sources. Their current popularity is due to their high efficiency (>60% [32] compared to ≈ 25 % for a combustion engine), low pollutant emissions [33], the safety of solid state components compared to liquid, and fuel flexibility (e.g. hydrogen, propane, natural gas [32]).

In a SOFC, $O_2$ gas is reduced at the cathode to produce two $O^{2-}$ ions.

$$O_2 + 4e^- \rightarrow 2O^{2-} \tag{1.1}$$

These negatively charged ions are transported through the electrolyte via a diffusion process to the anode, where they combine with the fuel, which, for this example, is taken to be $H_2$:

$$H_2 + O^{2-} \rightarrow H_2O + 2e^- \tag{1.2}$$

The electrons generated travel through an external circuit to the cathode (as demonstrated in Figure 1.1), generating an electric current. For this fuel cell to function efficiently, the electrolyte must have a high ionic conductivity, to allow for the rapid transport of oxide ions, and be an electrical insulator, so as to not short circuit the device.

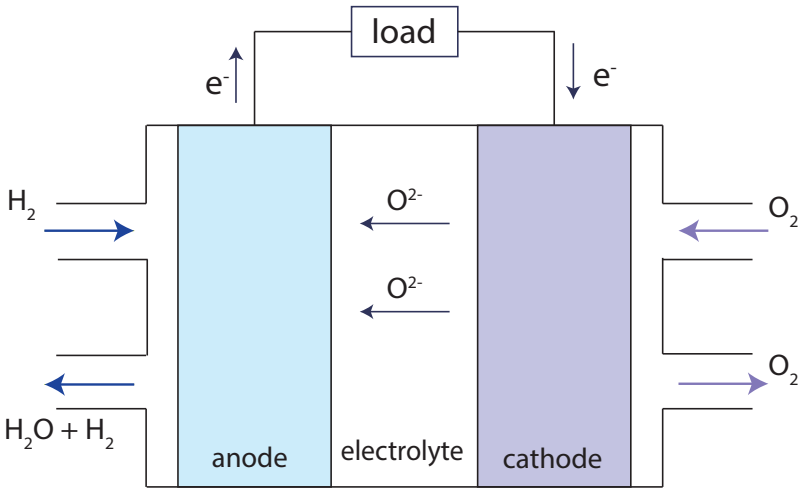


FIGURE 1.1: Schematic of a solid oxide fuel cell

The current generation of SOFCs are comprised of, a cathode that is capable of conducting both electronically and ionically, and is able to reduce $O_2$, such as $La_{1-x}Sr_xMnO_3$ (LSM); an electrolyte with a fast $O^{2-}$ conductivity, such as yttria-stabilised zirconia (YSZ); and an electronically conducting anode with the ability to oxidise the fuel, such as Ni/YSZ cermet [20, 21, 31, 34–36]. All of these components must be thermally stable and have similar thermal expansion coefficients to avoid fracturing at the component interfaces.

### 1.1.2 Gas Sensors

Gas sensors were first constructed in the 1950s for monitoring *in vivo* blood oxygen levels [37]. They are now capable of detecting and differentiating between a wide range of gases simultaneously. These sensors have many uses, including detecting the presence of toxic or combustible gases and for controlling the gas concentration emitted by car exhausts for pollution control [38].

In order to detect the presence of a gas, gas sensors utilise the driving force that gas experiences when moving from a higher pressure environment to a lower pressure one [1]. Many different gas sensors have been developed to detect different gases, such as $O_2$, $H_2$, $F_2$, $Cl_2$,

$CO_2$, $SO_x$ and $NO_x$. The schematic shown in Figure 1.2 is that of an oxygen sensor, demonstrating the regions of different pressure within the device, separated by two electrodes and an electrolyte, commonly consisting of yttria stabilised zirconia (YSZ) [26, 28].

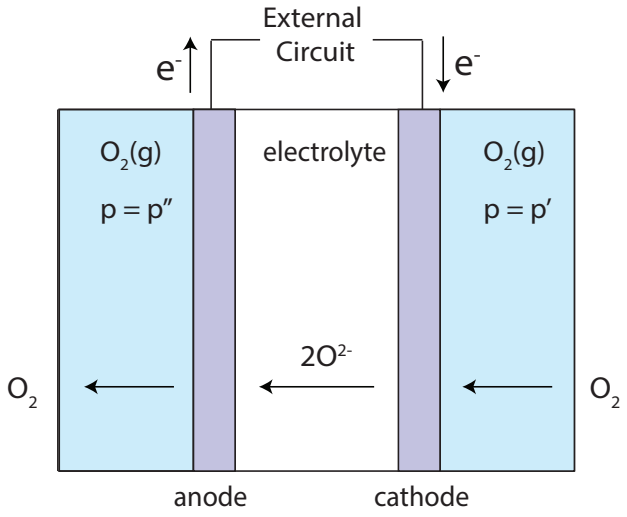


FIGURE 1.2: Schematic of an oxygen gas sensor, adapted from [1]

Provided the oxygen partial pressure at the cathode, p′, is greater than that at the anode, p″, the oxygen gas entering the sensor is reduced at the cathode, producing two $O^{2-}$ ions. These oxide ions diffuse through the electrolyte to the anode, where they are oxidised to produce oxygen gas. The equations for the reactions occurring within the cell are given by:

$$\text{Cathode:} \quad O_2(\text{p}') + 4e^- \rightarrow 2O^{2-} \tag{1.3}$$

$$\text{Anode:} \quad 2O^{2-} \rightarrow O_2(\text{p}'') + 4e^- \tag{1.4}$$

$$\text{Overall:} \quad O_2(\text{p}') \rightarrow O_2(\text{p}'') \tag{1.5}$$

As for the solid oxide fuel cell, this oxide ion diffusion generates a potential difference across the electrolyte, the magnitude of which can be measured by an external instrument. The magnitude of the chemical potential difference generated is limited by the amount of oxygen gas being oxidised at the anode, and therefore governed by the rate of diffusion across the electrolyte. This results in the output current from the sensor being linearly proportional to the gas concentration, allowing for exact measurement of low gas concentrations.

## 1.2 Fluorite Structure

The electrolyte through which the oxygen anions diffuse in solid oxide fuel cells and gas sensors is often comprised of YSZ, a fluorite structured material. Fluorite structured systems (space group Fm-3m) are formed by the cations constructing a rigid face-centered cubic (FCC) lattice, with the anions occupying tetrahedral positions within [39] (see Figure 1.3). Other examples of materials with this structure include $ZrO_2$, $UO_2$, $CeO_2$ $PbF_2$ and $CaF_2$. Fluorite structured materials are of particular interest for use as the electrolyte in electrochemical devices, as some have a "superionic", or "fast ionic" state, which they transition into above some critical temperature, $T_c$. This transition is attributed to the anion sublattice obtaining high diffusion coefficients, sometimes comparable to that of liquids [40], and results in high ionic conductivity, with no electronic conduction.

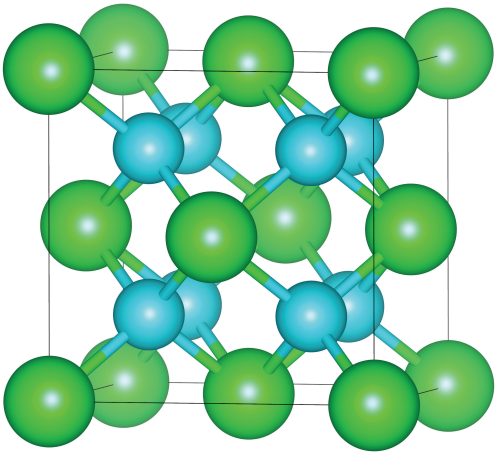

FIGURE 1.3: Fluorite structure; where the green atoms are the cations which posses cubic geometry, and the blue atoms are the tetrahedral anions

The mechanism by which diffusion, within the materials used to construct efficient electrochemical devices, occurs must be fully studied and understood. The presence of defects within a material is one of the main factors that has an effect on its diffusion. Point defects affect the microscopic diffusion mechanisms within the materials, which can have considerable macroscopic consequences on the diffusion properties. Due to the polycrystalline nature of the materials used to construct these devices, extended defects, such as surfaces and grain boundaries, can also have a substantial effect on the mechanism and rate by which ionic diffusion occurs.

## 1.3 Defects

A perfect crystal structure is one in which all atoms are located on their correct lattice sites and all sites are occupied. This perfect structure is impossible to produce in reality due to the presence of defects. There will always be a certain number of defects within the crystal lattice, the concentration of which is largely dependent on the temperature and increases with temperature. These defects can be thermodynamic, localised defects, known as point defects, or extended defects, generated during synthesis, such as surfaces, dislocations and grain boundaries. The presence of these defects within a crystal structure affects various macroscopic properties of the crystal system, including diffusion, strength, colour, and magnetic and electronic behaviour [39, 41, 42]. The concentration and effect these defects have on the properties of a material increase with temperature.

### 1.3.1 Point Defects

Point (zero-dimensional) defects can be either vacancies, interstitials or substitutional impurities and can be classified as being intrinsic or extrinsic defects. A vacancy in a crystal is defined as a missing atom or ion, and is generally portrayed as a square in a crystal lattice. An interstitial defect is an excess atom or ion that does not reside at a normal lattice site in the crystal. A substitutional atom is one of a different type that the lattice atoms, which replaces a lattice atom at its lattice site.

In some materials, especially those with weak ionic or covalent bonds, anti-site defects occur, where atoms of different types exchange sites. For example, in a compound AB, an A atom would appear on a site normally occupied by a B atom or vice versa, as demonstrated in Figure 1.4. This defect is neither a vacancy, nor an interstitial, nor an impurity. They can be formed during crystal growth, or can be generated after the crystal has formed, provided there is sufficient energy to allow for atomic movement [43].

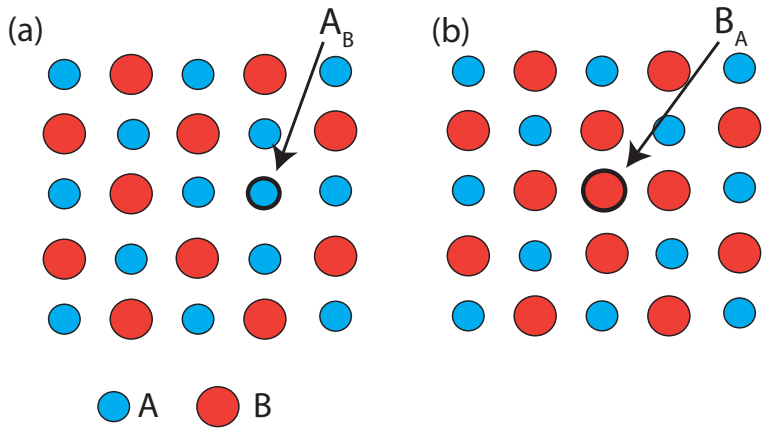


FIGURE 1.4: Schematic of anti-site point defects in an ionic crystal of AB: (a) A on B site, $A_B$ and (b) B on A site, $B_A$

#### 1.3.1.1 Intrinsic Defects

Intrinsic defects are defects that are inherent to the material, and are so called as they do not require the addition of impurities into the system, but require only thermal activation. The two most common intrinsic defects in ionic crystal structures are Schottky and Frenkel defects [44] (see Figure 1.5). Schottky defects occur as a result of the concurrent existence of anion and cation vacancies within the structure at thermal equilibration in a ratio that ensures the charge neutrality of the system is maintained. This is most prevalent in compounds with a 1:1 stoichiometry where the cations and anions have a similar size [1]. For example, the Schottky defects in NaCl is given in Kröger-Vink notation [45] by:

$$\mathrm{Na}_{\mathrm{Na}}^{\times} + \mathrm{Cl}_{\mathrm{Cl}}^{\times} \Longleftrightarrow \mathrm{v}_{\mathrm{Na}}^{\prime} + \mathrm{v}_{\mathrm{Cl}}^{\bullet} + \mathrm{NaCl} \tag{1.6}$$

where the main body of the notation represents the element, or vacancy (v); the subscript represents the site of the defect, where i would denote an interstitial site; the superscript represents the effective charge (with respect to the charge of the element that would normally occupy that site), with ($\bullet$) denoting a positive charge, ($'$) a negative charge and ($\times$) neutral.

Frenkel defects are formed by atoms becoming displaced from their original lattice sites, and moving to an interstitial site, generating pairs of vacancies and self-interstitials, known as

Frenkel pairs [46]. For a simple compound, such as AgCl, the Ag Frenkel defect formation can be given by:

$$Ag_{Ag}^{\times} + Cl_{Cl}^{\times} \Longleftrightarrow Ag_{i}^{\bullet} + V_{Ag}^{'} + Cl_{Cl}^{\times} \tag{1.7}$$

This type of defect generally only occurs in one of the sublattices of the crystal [1], and are therefore classified as being either cation or anion Frenkel defects. Anion Frenkel defects are less common, as anions are usually the larger species and so it is more difficult for them to occupy a confined, low-coordination interstitial site [1]. An exception to this general rule is the formation of anion Frenkel defects in fluorite-structured materials, such as $CaF_2$, $PbF_2$ and $CeO_2$. These structures facilitate the formation of anion Frenkel defects due to their lower anionic charge, in comparison to that of the cations, allowing them to move closer to one another. Fluorite structures also possess large, open sites that can be used as interstitial sites.

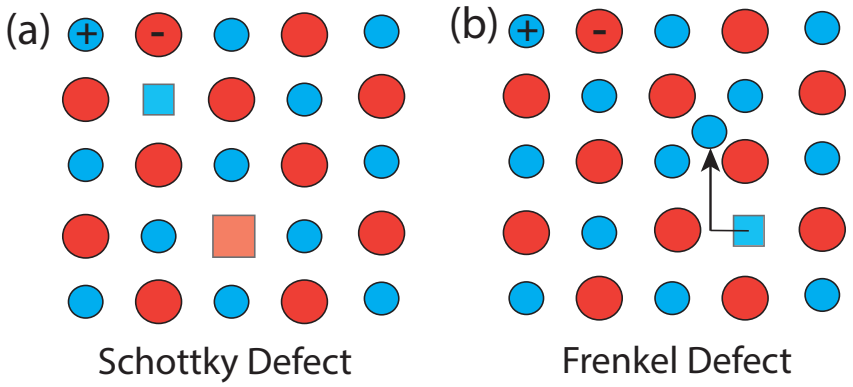


FIGURE 1.5: A schematic of (a) Schottky and (b) cationic Frenkel defect, demonstrating the vacancies (squares) and interstitials generated.

#### 1.3.1.2 Extrinsic Defects

Unlike intrinsic defects, which are present in a pure material, extrinsic defects arise as a result of a dopant being introduced into a material. Substitutional impurities are foreign atoms in a crystal lattice, present through accidental impurities or deliberate doping. They can be situated either on regular lattice sites, replacing the regular atom, or they can appear as interstitials. The substitution of atoms can be difficult due to the tightly packed nature of the atoms within a solid, and is generally only achieved if both atoms are approximately

the same size. If the defect substituent has a difference valence state to that of the host, it is known as aliovalent [46]. As with intrinsic defects, the system must always be kept charge neutral, and this can be done through the formation of charge compensating vacancies. For example, when a fluorite structured oxide, $MO_2$, is doped with a sesquioxide, $D_2O_3$, one oxygen vacancy is generated for every pair of cations in the dopant introduced [47]:

$$D_2O_3 + 2M_M^{\times} + O_O^{\times} \Longleftrightarrow 2D_M^{'} + V_O^{\bullet\bullet} + 2MO_2 \tag{1.8}$$

The deliberate insertion of a foreign species can be used to alter the properties (e.g. ionic diffusion, structure, electrical conductivity and optics) of the material [1, 42, 48, 49].

### 1.3.2 Extended Defects

Extended defects can be classified as linear (one-dimensional) or planar (two-dimensional) defects. Linear defects can be dislocations, due to the translational displacement of atoms, or disclinations, due to the rotational displacement of atoms [1, 46]. Dislocations are much more common and affect the crystal growth and mechanical properties of the material [39]. Planar defects include crystal twinning, crystallographic shear planes, intergrowth structures, and grain boundaries [1, 39].

#### 1.3.2.1 Surfaces

Surfaces are made up of atoms that do not possess a complete coordination number of neighbouring atoms for that material. The lower coordination of surface atoms than those within the bulk results in the surface and sub-surface atoms having to respond and relax into a configuration that can be significantly different to that of the bulk structure [50]. The presence of surfaces can have an impact on many properties of the crystal, such as crystal morphology, catalysis and diffusion [51, 52]. The extent of the effect is determined by the type of material and the surface termination.

Cutting a bulk crystal at different angles will result in different surface terminations being generated. These surfaces can be described using Miller indices. To determine the Miller index of a surface:

(i) Find where the plane of the surface intercepts the three basic axes in terms of lattice constants.

(ii) Take the reciprocals of the intercepts and multiply by the lowest common number that results in all three being integers. The resulting numbers are then written as (hkl) [44].

e.g. a plane that cuts the basic axes at 5, 4, 2 has reciprocals $\frac{1}{5}$, $\frac{1}{4}$, $\frac{1}{2}$ and Miller index (4 5 10). Figure 1.6 demonstrates some of the important planes in a cubic crystal and their corresponding Miller index. If the plane does not intercept one of the axes, the corresponding index is zero, as seen for the (100) and (110) surfaces. If the plane intercepts with one of the axes at a negative value, the index is calculated in the same way as before, however, the index is denoted as being negative by placing a minus sign above the number, e.g. a plane with intercepts 5, -4, 2 has a Miller index (4 $\overline{5}$ 10).

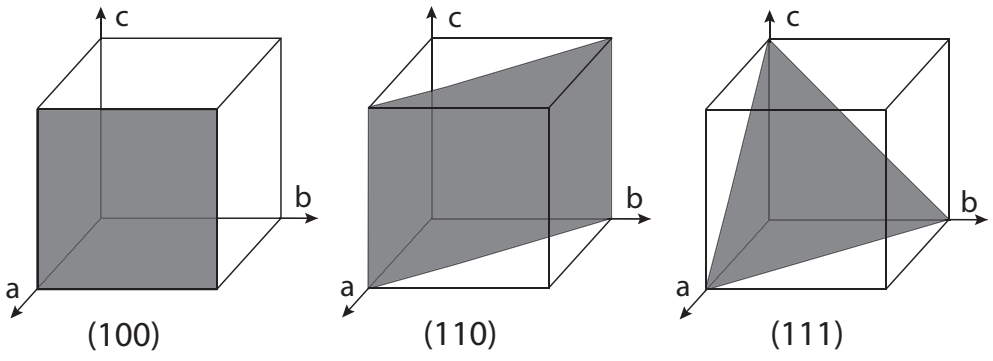


FIGURE 1.6: Some standard planes within cubic systems with their corresponding Miller index

**1.3.2.1.1 Tasker Surfaces** Tasker was one of the first investigators interested in the properties of surfaces. He grouped all ionic surfaces into three categories [53]. Type 1 surfaces consist of charge neutral repeat layers, type 2 are made up of charged planes that can be grouped to form a zero dipole repeat unit, and type 3, is comprised of charged planes that generate a net dipole moment perpendicular to the surface.

As shown in Figure 1.7, the type 3 surfaces cannot be constructed without generating a dipole moment perpendicular to the surface, which causes the surface energy to diverge [54]. This surface must therefore be reconstructed to neutralise the dipole. This can be done by transferring half of the of the top layer of atoms to the bottom surface, generating a dipole across the crystal that opposes the surface dipole moment.

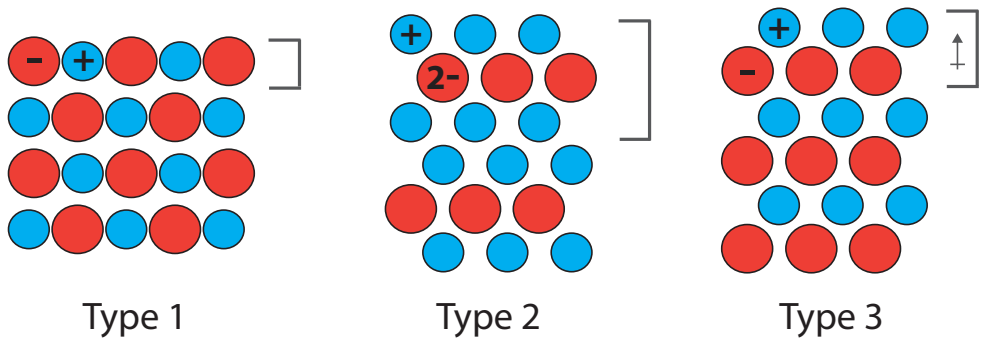


FIGURE 1.7: The three types of Tasker surfaces; indicating the charge neutral non-dipolar repeat layer in type 1, the charge neutral non-dipolar repeat unit in type 2, and the neutral dipolar repeat unit generated by type 3

**1.3.2.1.2 Surface Energy** The stability of a surface compared to bulk is determined by its surface energy. The relative surface energies for various surface orientations of the same material can be used, for example, to determine the equilibrium crystal morphology [55–57]. The surface's stability is determined by its surface energy, $\gamma$, defined as the energy required to cleave that particular surface orientation from the bulk [58], and is given by [59]:

$$\gamma = \frac{\text{(energy of crystal with surface) - (energy of same number of bulk ions)}}{\text{(surface area)}} \tag{1.9}$$

$\gamma$ has units $J/m^2$, thus allowing a ready comparison between the surface energies for all surface orientations of a material.

#### 1.3.2.2 Grain Boundaries

Grain boundaries can be described as being an interface between two crystal grains with different orientations and can be formed as either tilt or twist grain boundaries (as demonstrated in Figure 1.8), or can be comprised of a mixture of both [60]. Tilt boundaries result in open structures within ionic crystals that have densities lower than the bulk system surrounding them [61] and are generated by reflecting a surface to create its mirror image. The presence of grain boundaries within a crystal system affects the overall ionic conductivity of a crystal system. The extent of the effect is dependent on the material and the type of grain boundary.

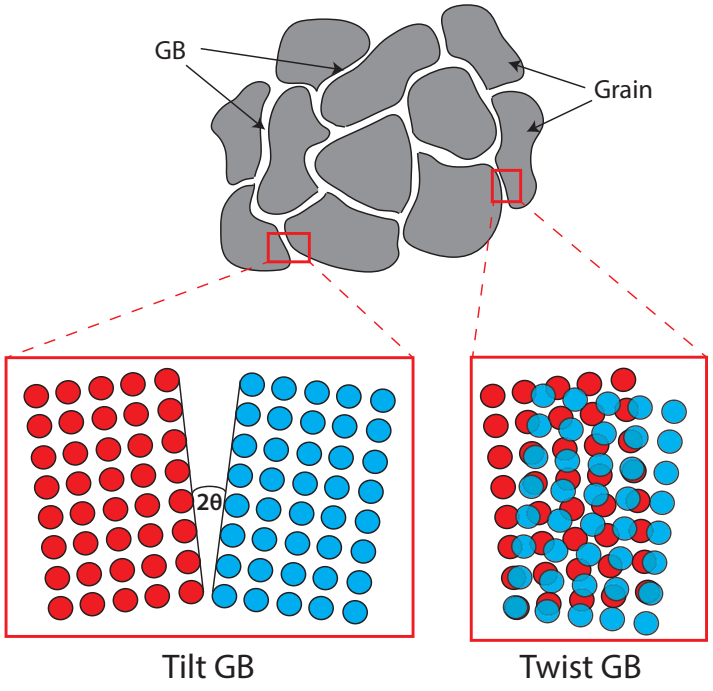


FIGURE 1.8: Schematic demonstrating the structure of a generic tilt and twist grain boundary, where $2\theta$ is the misorientation angle

**1.3.2.2.1 Coincidence Site Lattice** The identification system used to classify the various different grain boundaries is based on the coincidence site lattice (CSL), first considered by Kronberg and Wilson in 1949 [62]. When two crystals are brought into contact, some of their lattice positions will be coincident. The CSL model is based on the concept that when the number of coincident lattice positions is high, the grain boundary energy will be lowered

due to a smaller number of broken bonds across the boundary [63]. The reciprocal of the density of these coincident sites is known as Σ, which, for a chosen elementary cell, can be given as [61]:

$$\Sigma = \frac{\text{number of coincidence sites in the elementary cell}}{\text{total number of lattice sites in the elementary cell}} \tag{1.10}$$

For cubic systems, Σ can simply be given by:

$$\Sigma = \delta(\mathrm{h}^2 + \mathrm{k}^2 + \mathrm{l}^2) \tag{1.11}$$

where h, k, l are the Miller indices of the surface and $\delta$ is 1 if $(\mathrm{h}^2 + \mathrm{k}^2 + \mathrm{l}^2)$ is odd and $\frac{1}{2}$ if $(\mathrm{h}^2 + \mathrm{k}^2 + \mathrm{l}^2)$ is even [64].

**1.3.2.2.2 Grain Boundary Energy** The relative stability of grain boundaries can be determined from the grain boundary energies per surface area, defined as the energy required to generate a boundary [65], calculated using a similar method to that used to determine the surface energy (Equation 3.2):

$$\sigma_{GB} = \frac{\text{(energy of crystal with GB) - (energy of same number of bulk ions)}}{\text{(GB area)}} \tag{1.12}$$

As for $\gamma$, $\sigma_{GB}$ has units $\mathrm{J/m^2}$ which facilitates a straightforward comparison of grain boundary energies of various orientations.

### 1.3.3 Strain

Strain can be introduced into a crystal system by lattice mismatch at interfaces, and can be classed as being either tensile or compressive strain [66–68] (see Figure 1.9). Tensile strain is formed when the lattice constant of the strained system, $a_s$, is greater than that of the unstrained system, $a_0$, and compressive strain is formed when $a_s$ is smaller than $a_0$. A strained system can have different properties, such as ionic conductivity to its unstrained counterpart. The strain, $\epsilon$, applied to a system can be given by:

$$\epsilon = \frac{a_s - a_0}{a_0} \tag{1.13}$$

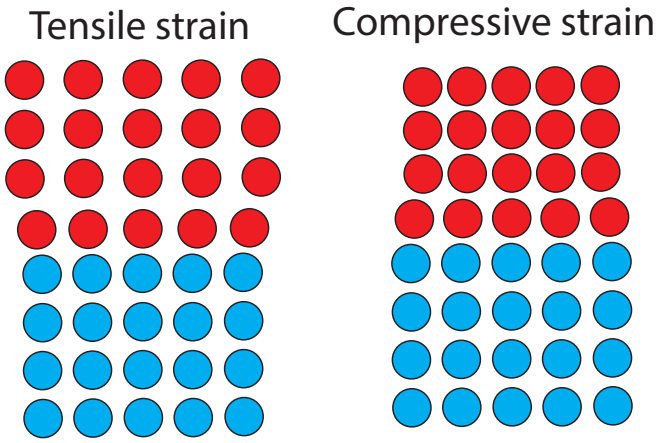


FIGURE 1.9: Schematic demonstrating tensile and compressive strain experienced (red) compared to the substrate (blue)

## 1.4 Diffusion

The study of diffusion is extremely important in materials chemistry, due to the effect it has on numerous properties of a material. Diffusion is a central process occurring in all of the aforementioned electrochemical devices and is affected by the defects previously detailed. It is measured by its diffusion coefficient (in SI units - $m^2/s$), which describes the movement of ions, atoms or molecules as a function of time. The cause of the diffusion within a system can be as a result of a concentration gradient, as for Fick's Law, or as a result of thermal motion, also known as self-diffusion, with which the work in this thesis is interested.

### 1.4.1 Fick's Law

Diffusion can be thought of using the flux of the material; that is, the rate at which atoms pass through an area of unit size in a unit of time. This diffusion process is driven by a concentration gradient present in a material, with the atoms moving from an area of high to low concentration (Figure 1.10). This mechanism was first mathematically considered by Fick in 1855 [69], who found that the flux of a material is a function of the concentration gradient. For one dimension this is given as:

$$J(x) = -D\left(\frac{\partial C}{\partial x}\right) \tag{1.14}$$

where $J(x)$ is the flux of the diffusing species, $x$ is the position, $D$ is the diffusion coefficient and $\left(\frac{\delta C}{\delta x}\right)$ is the concentration gradient.

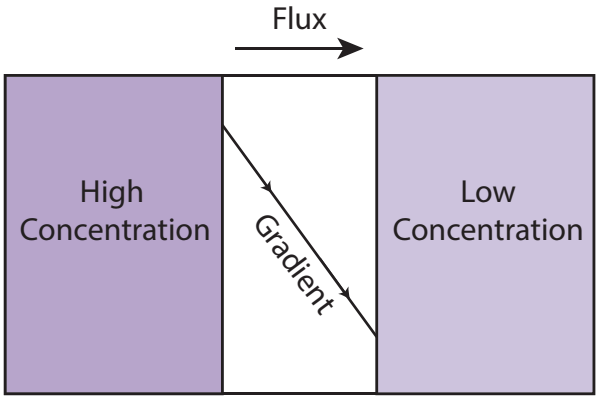


FIGURE 1.10: The flux of the diffusing species goes from high to low concentration

### 1.4.2 Random-Walk Diffusions

When there is no driving force, such as a concentration gradient, present, the random way in which atoms diffuse can be viewed as a form of Brownian motion [70], which was initially observed in 1828 in the motion of pollen grains in water. This movement was later explained by Einstein in 1905 [71] to be as a result of collisions with the water molecules, resulting in the grains moving in a random walk.

For a solid, crystal system, the random walk of the diffusion can be described by random hops of ions from one lattice site to another, as a result of thermal energy. Due to the random nature of the diffusion of individual particles and the lack of external forces or a concentration gradient, their net displacement will be zero and hence the diffusion of the system is determined using mean squared displacement calculations.

The diffusion coefficient calculated using the random-walk method can be compared to that obtained via Fick's law. Consider a collection of mobile ions, hopping along the $x$-axis to a nearest-neighbour vacant site. The hop length is denoted as $\Delta x$, the hop rate is $\frac{1}{\Delta t}$ and the number of ions at position $x$, at time $t$, is $N(x,t)$. Due to the random-walk of the particles, the net movement of all the ions will be zero, as, for a given timestep, half will move left and

the other half will move right. The half of the ions at point $x$ will move right, while the half at point $x + \Delta x$ will move left. The net movement of ions to the right is therefore:

$$-\frac{1}{2}[N(x+\Delta x,t) - N(x,t)] \tag{1.15}$$

The flux, $J$, of the ions across area $a$, along the $x$ direction during one hop ($\frac{1}{\Delta t}$) can be written as:

$$J(x) = -\frac{1}{2}\frac{1}{\Delta t}\left[\frac{N(x+\Delta x,t)}{a} - \frac{N(x,t)}{a}\right] \tag{1.16}$$

Multiplying the top and bottom of the right hand side by $(\Delta x)^2$ gives:

$$J(x) = -\frac{(\Delta x)^2}{2\Delta t}\left[\frac{N(x+\Delta x,t)}{a(\Delta x)^2} - \frac{N(x,t)}{a(\Delta x)^2}\right] \tag{1.17}$$

The diffusion coefficient in one dimension, $D$ can be defined as $\frac{(\Delta x)^2}{2\Delta t}$ and the concentration of the particles can be given as $C = \frac{N}{a\Delta x}$, the flux can therefore be rewritten as:

$$J(x) = -D\left[\frac{C(x+\Delta x,t)}{(\Delta x)} - \frac{C(x,t)}{(\Delta x)}\right] \tag{1.18}$$

As $\Delta x$ goes to zero, a first order Taylor expansion is used, giving:

$$J(x) = -D\left(\frac{\partial C}{\partial x}\right) \tag{1.19}$$

which is Fick's Law.

### 1.4.3 Diffusion Mechanisms

Diffusion can occur through a variety of different mechanisms, including interstitial, interstitialcy (also known as indirect interstitial) and vacancy diffusion [1]. Interstitial diffusion (Figure 1.11(a)) occurs when an atom moves from one interstitial position to another, without occupying a lattice position [72]. In order for appreciable diffusion to occur there must be a sufficient number of interstitial sites present in the lattice. The diffusing atom must also be small relative to the crystal lattice of the system so that it can fit into the interstitial positions and diffuse within the larger lattice structure without generating large lattice distortions [49]. Interstitialcy diffusion (Figure 1.11(b)) occurs when atoms at an interstitial position displaces an atom at a lattice site, resulting in the atom from the lattice site becoming an interstitial [73].

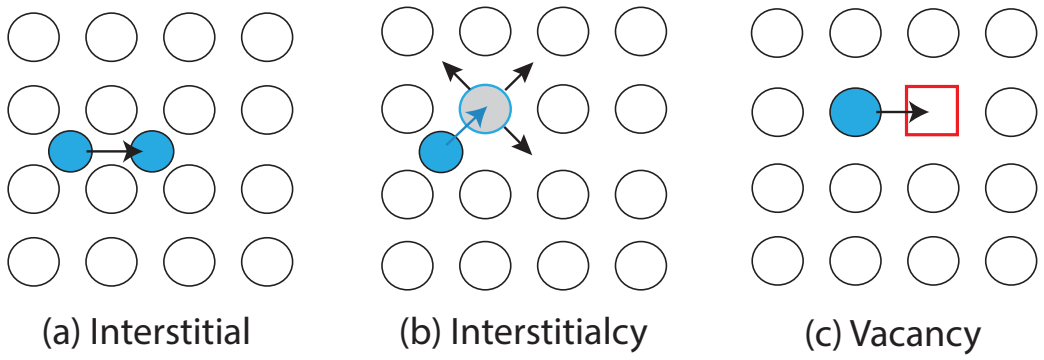


FIGURE 1.11: The interstitial, interstitialcy and vacancy diffusion mechanisms

Vacancy diffusion (Figure 1.11(c)) occurs when an atom diffuses into a neighbouring vacant site. This mechanism is prevalent in imperfect crystal structures, especially at high temperatures, due to the increased movement of ions away from their lattice sites, which results in a higher concentration of vacancies. The diffusing atom requires sufficient energy to generate distortions within the lattice in order to move to a new lattice position. The activation energy of diffusion for this mechanism originates from the sum of the vacancy formation energy and the migration energy barrier [49]. The vacancies present in the system can be an intrinsic property of the crystal or can be introduced via doping. For fluorite structured materials, vacancies can be generated as a charge compensation mechanism by doping the system with a lower valent cation.

### 1.4.4 Effects on Diffusion

Materials used in the construction of diffusion based electrochemical devices will contain defects and have strain introduced at component interfaces. It is therefore vital to understand how the presence of extended defects and strain affects diffusion.

#### 1.4.4.1 Grain Boundaries

The effect of grain boundaries on various properties, such as diffusion, has been a topic of interest for decades from both an experimental and computational perspective [8, 64, 74–76], however very few studies have focused on separating the effect of the grain boundaries from the overall diffusive effect observed. And of those that have, there has been very little consensus as to the effect these interfaces have on conductivity. Due to the fact that most diffusion based devices are constructed using polycrystalline materials, it is vital to fully understand the mechanism by which the ionic diffusion occurs both along and across these grain boundaries in order to optimise the diffusion and increase the devices' efficiency.

The diffusion of bulk systems containing these interfaces has been widely studied, however, only the collective behaviour of all grain boundary orientations has been considered, with no systematic study of the diffusion properties of specific boundaries. There is also some disagreement within literature as to whether the presence of grain boundaries hinders [11, 77] or enhances [78] the ionic diffusion along the boundary. This work will address this issue for individual grain boundary orientations.

#### 1.4.4.2 Strain

Strain induced in a system has been shown, both experimentally [68, 79] and computationally [67, 80–83], to alter the ionic conductivity of the system. There is a general consensus within literature that applying a compressive strain will inhibit diffusion, thus having a detrimental effect on the ionic conductivity of the system, whilst tensile strain aids the diffusion process [66, 67, 80, 84]. The cause of the strain effects have been postulated to be as a result of a lowering of the migration activation energy [85], attributed to an increase in the migration space and a decrease in anion-cation interactions [86].

There are, however, discrepancies within literature as to the extent of the change. The extent of the increase in ionic conductivity as a result of tensile strain has been reported to reach as high as five to eight orders of magnitude, which is known as colossal ionic conductivity [87, 88], down to no change at all being detected [89]. This immense range of values highlights the need for further investigation into the mechanism by which strain effects ionic conductivity. There is, however, a consensus that there is a value for the strain that produces the maximum diffusion coefficient, known by some as the critical strain [82, 86, 90], and any additional strain applied will have a detrimental effect on the diffusion.

## 1.5 Thesis Outline

Chapter 1 has given a brief insight into the need for clean, renewable energy sources, such as electrochemical fuel cells, and the importance of increasing their working efficiency through first fully understanding, and then optimising, the diffusion process. The methods by which ionic diffusion occurs have been discussed, along with defects within crystalline materials that can have an effect on this diffusion. The benefits of fluorite structured materials for fast ionic conductivity has been highlighted and will be expanded on in later chapters.

Chapter 2 will discuss the underlying theory used in this work. This includes the basic principles of molecular dynamics (MD), and the computational tools used to analyse the information obtained from MD will be summarised. The interatomic potential used within the MD investigation is also discussed.

The findings of this thesis are presented according to material, with calcium fluoride and yttria-stabilised zirconia being discussed in Chapters 3 and 4 respectively. Both results chapters will first detail the findings for the relevant bulk system, so as to demonstrate the ability of the potential used to generate results comparable to those within both experimental and computational literature.

Chapter 3 will continue with a discussion of the properties of various $CaF_2$ surface and grain boundaries, with a particular emphasise on the study of the ionic diffusion effects. Due to its high conductivity, the study of diffusion within $CaF_2$ enables large amounts of meaningful statistics to be gathered within a reasonable time for a range of interfaces. As a result of its cubic fluorite structure, this information can, for example, be used to construct a model of a fluorite structured system. $CaF_2$ is, therefore, an excellent material to use in order to study the effects of grain boundaries, as its macroscopic properties are well understood. It is also a stable structure, with the ability to ionically diffuse without the addition of any dopants, enabling the pure investigation into the effect of grain boundaries without the inclusion of dopant effects.

Chapter 4 will include an analysis of various YSZ surface orientations, the vacancy segregation associated with the surfaces and the diffusivity of these surfaces. This material is a popular choice for the electrolyte in many diffusion based electrochemical devices, and as such there is experimental and computational data to compare to and expand on.

To conclude, Chapter 5 will summarise and compare the findings of both fluorite structured materials studied and discuss future work made possible by the work completed here.

# Chapter 2: Theory

Molecular dynamics (MD) is used to simulate the movements of atomic scale systems by studying the time evolution of the atomic positions within the system. This approach is therefore well suited to investigate the thermal effects on time dependent properties, such as diffusion. In MD, to determine time dependent properties, the trajectories of the atoms over a period of time is calculated using Newton's equations of motion. To do this, the forces on the atoms must be calculable. MD was first developed in the late 1950s by Alder and Wainwright [91, 92] for hard sphere systems (containing up to 500 atoms), and improvements in computational power and memory have resulted in MD simulations of much larger systems being able to be carried out in a reasonable amount of time. However, despite its efficiency for larger systems, only time scales of $\approx 10^{-9}$s can feasibly be investigated.

In general, explicitly considering electrons within a system (as with *ab initio* methods) can introduce an additional level of complexity for atomic dynamics. Approximations on their interactions can be made in order to produce computationally efficient methods. Interaction potentials make these approximations by considering the attractive and repulsive forces between atoms, as described by analytical functions, which allows for large atomic systems to be examined.

## 2.1 Interaction Potential

The interaction potential used in this work is known as the DIPole Polarisable Ion Model (DIPPIM) [93]. This model consists of four elements: charge-charge interactions, short-range repulsion, dispersion interactions and polarisation:

$$U = U^{qq} + U^{rep} + U^{disp} + U^{pol} \tag{2.1}$$

### 2.1.1 Long Range Interaction

The long range interaction between point charges, $q$, on atoms $i$ and $j$, separated by distance $r_{ij}$, is given by the Coulomb potential:

$$U^{qq} = \sum_{i<j} \frac{q_i q_j}{r_{ij}} \tag{2.2}$$

However, due to the slow decay of the $\frac{1}{r}$ with distance, an Ewald sum [94, 95] is used for the long-range interactions.

### 2.1.2 Short Range Interaction

A Born-Mayer pair potential can be used to describe the short-range repulsion of calcium fluoride [96], as it gives a good fit to $CaF_2$ *ab initio* data [97]:

$$U_{ij}^{rep}(r_{ij}) = B_{ij} e^{(-b_{ij} r_{ij})} \tag{2.3}$$

where $B_{ij}$ is dependent on the radii of the ions $i$ and $j$, and $b_{ij}$ is the decay rate control constant for ions displaced by a distance $r_{ij}$.

Yttria-stabilised zirconia contains highly polarisable oxide ions. The short-range repulsion of this system is given by:

$$U_{ij}^{rep} = \sum_{i \leq j} A_{ij} \frac{e^{-a_{ij} r_{ij}}}{r_{ij}} + \sum_{i \leq j} B_{ij} e^{-b_{ij} r_{ij}^2} \tag{2.4}$$

where the first term has the form of a Yukawa potential [98] and is selected over the standard $B_{ij} e^{(-b_{ij} r_{ij})}$ potential as it gives a better fit to the YSZ *ab initio* data [93]. The second term is a Gaussian, which is included to prevent strong polarisation effects at small anion-cation interatomic distances from causing instability by acting as a steep repulsive wall at very small separation distances [99].

### 2.1.3 Dispersion

The dispersion interaction energy accounts for the mutually induced temporary multipoles between ions and is determined using:

$$U_{ij}^{disp}(r_{ij}) = -\sum_{i \leq j} \left[ \frac{C_{6,ij}}{r_{ij}^6} f_6(r_{ij}) + \frac{C_{8,ij}}{r_{ij}^8} f_8(r_{ij}) \right] \tag{2.5}$$

where $C_{6,ij}$ and $C_{8,ij}$ are the dipole-dipole and dipole-quadropole dispersion coefficients respectively. $f_6(r_{ij})$ and $f_8(r_{ij})$ are dispersion damping functions, used to reduce the magnitude of the attractive interaction at short interatomic distances where the overlap of the ion wavefunctions is non-negligible [97], and are represented by Tang-Toennies functions [100]:

$$f_n(r_{ij}) = 1 - e^{(-b_n r_{ij})} \sum_{k=0}^{n} \frac{(b_n r_{ij})^k}{k!} \tag{2.6}$$

where $b_n$ represents the damping parameters.

### 2.1.4 Polarisability

The DIPPIM, as the name suggests, is designed to include the polarisation effects generated by the dipoles induced on ions within the system. In order to determine the induced dipoles on both the cations and anions in the system, the following expression is minimised for all dipoles, $\mu_\alpha^i$, for a given configuration, at each MD timestep:

$$U^{pol} = \sum_{j \neq i} \left[ (q^i \mu_\alpha^j - q^j \mu_\alpha^i) T_\alpha^{(1)}(r_{ij}) f_{ij}^*(r_{ij}) - \mu_\alpha^i T_{\alpha\beta}^{(2)}(r_{ij}) \mu_\beta^i \right] + \sum_{i=1} \frac{1}{2\alpha^i} \mu_i^2 \tag{2.7}$$

where $q^i$ and $q^j$ are the formal charges of ions $i$ and $j$, $T_\alpha^{(1)}(r_{ij})$ and $T_{\alpha\beta}^{(2)}(r_{ij})$ are the charge-dipole and dipole-dipole interaction tensors respectively [101]. The last term of Equation 2.7 describes the energy required to polarise ion $i$, where $\alpha^i$ is the dipole polarisability of ion $i$. The polarisability damping function, $f_{ij}^*$, is described by a modified Tang-Toennies function, similar to Equation 2.6 and is used to account for the short-range induction effects on the dipoles:

$$f_{ij}^*(r_{ij}) = 1 - c_{ij} e^{(-b_{ij} r_{ij})} \sum_{k=0}^{4} \frac{(b_{ij} r_{ij})^k}{k!} \tag{2.8}$$

This includes the parameter $c_{ij}$, which determines the strength of the ion response to the polarisation effect.

The molecular dynamics code, PIMAIM (Polarisable Ion Model Aspherical Ion Model) [102], is used in this work, which utilises the DIPPIM and minimises the dipoles using the conjugate gradient method [103]. This dipole minimisation step is generally the most time consuming part of the simulation.

### 2.1.5 Periodic Boundary Conditions

Periodic boundary conditions (PBC) can be used in MD simulations to replicate bulk-like conditions without the properties of the system being influenced by surface effects. PBC repeat a unit cell (known as the primary cell), containing N atoms, in all directions to simulate an infinite lattice in order to better represent the macroscopic properties of the crystal. The movement of all atoms within the primary cell is replicated in each of the image cells. When an atom leaves the primary cell it enters into a neighbouring image cell and an atom from the opposite neighbouring cell enters the primary cell through the opposite face (this movement is demonstrated in Figure 2.1).

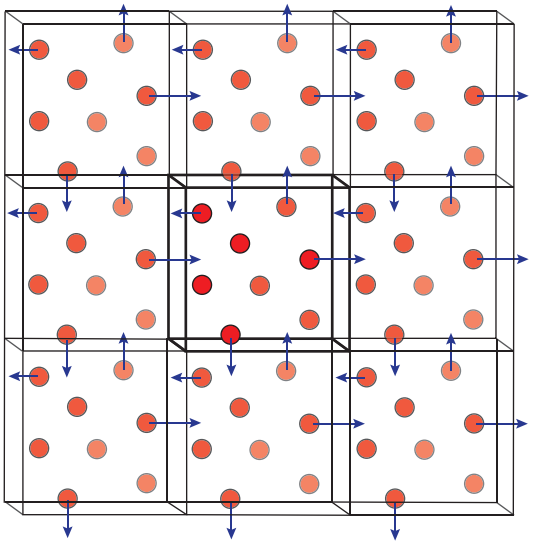

FIGURE 2.1: Periodic boundary conditions; the primary cell is shown in the centre, surrounded by identical image cells. The arrows demonstrate how, when one particle leaves the primary box, one of its images from a neighbouring cell enters through the opposite face

All of the short-range interactions within the system generated using PBC are truncated in real space using a short range cut-off in order to make the computational time required tractable. For short-range interactions the nearest image convention can be used, where each particle only interacts with the closest image of each of the other particles, which simplifies the calculation and also ensures that atoms do not interact with their own images. It is therefore a requirement that the value of the cut-off not be greater than half of the smallest width of the repeated, primary cell, to ensure that only the nearest images will be within the short-range cut off, as demonstrated in Figure 2.2.

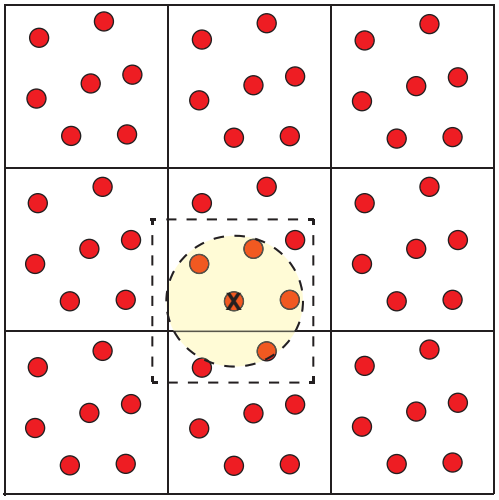

FIGURE 2.2: The primary cell is shown in the centre, surrounded by identical image cells. The large yellow circle demonstrates the short-range cut-off of the atom marked "X". Note that not all of the nearest images reside in the primary cell

Interactions that act over a longer range of ionic separations than the short-range interactions, such as ionic polarisation, must be treated separately. The most popular technique, and the one utilised within PIMAIM, for determining these long-range interactions is the Ewald summation [94, 95].

## 2.2 Classical Molecular Dynamics

### 2.2.1 Procedure

In order to carry out a MD simulation there are a number of steps which must be taken, and are demonstrated in Figure 2.3. An inital structure is determined by defining the starting atomic positions of the atoms within the system. These atoms are then assigned initial velocities so they do not start at rest. The dipoles present in the system must then be relaxed to lower and optimise the energy of the system. The next step involves calculating the forces acting on the atoms within the system. This step can be very computationally expensive. These forces are used to update changes that may have occurred to the atomic positions and velocities after a period of time, known as the timestep, $\delta$t.

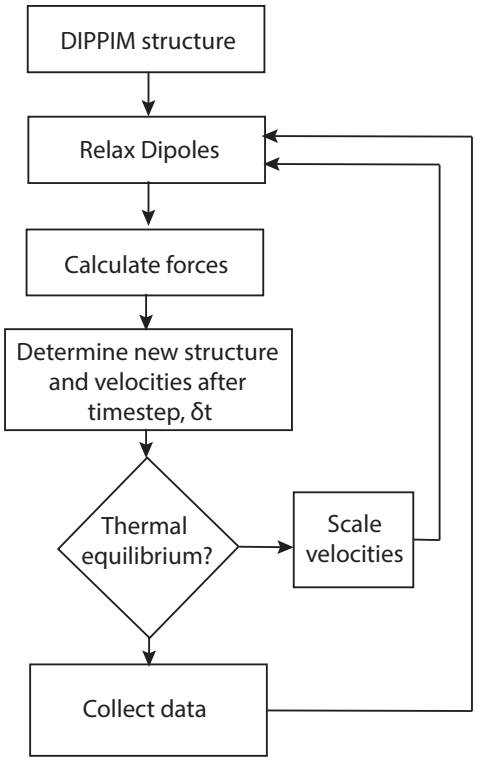


FIGURE 2.3: Flow chart demonstrating the steps taken to perform a MD simulation

Due to the fact that the inital structure and velocities were assigned, the system must be allowed to come to equilibrium before any data can be collected for analysis. To determine whether the system has reached equilibrium the potential, kinetic and total energies can be plotted as a function of time, to ensure there are not large fluctuations in energy. If

the system is determined to have not reached equilibrium, then the atomic velocities are scaled, the forces are recalculated and the process is repeated. Once thermal equilibrium has been achieved, information about the system, such as atomic postions and velocities, can be collected.

#### 2.2.1.1 Initial Set-up

For every MD simulation, an initial atomic structure must be provided, this structure is often obtained from experimental coordinates, from methods such as neutron or x-ray diffraction. Alternative methods include using the coordinates from an energy minimisation or using a template of a different material with a similar structure, edited to account for changes such as bond lengths.

Once the structure has been determined, the particles within the system are then assigned random velocities, such that the total kinetic energy of the system, $\mathrm{E}_k$, containing $N$ atoms, is equivalent to the temperature at which the simulation is to be run:

$$\langle E_k \rangle = \frac{1}{2} \sum_{i}^{N} m_i \mathbf{v}_i^2 = \frac{kT}{2}(3N - N_F) \tag{2.9}$$

where $m_i$ and $\mathbf{v}_i$ are the mass and velocity of atom $i$ respectively. $N_F$ are the degrees of freedom that are constrained to zero, for a periodic box $N_F = 3$ (translational motion) and for a molecule $N_F = 6$ (translational and rotational motion), therefore $(3N - N_F)$ is the total number of degrees of freedom.

#### 2.2.1.2 Newton's Equation of Motion

Once the initial positions and velocities have been assigned the forces acting on the particles are calculated. The force is determined by Newton's second law, given by:

$$\mathbf{F}_i = m_i \frac{\delta^2 \mathbf{r}_i}{\delta t^2} = m_i \mathbf{a}_i \tag{2.10}$$

indicating that the force, $\mathbf{F}_i$, acting on atom $i$, at position $\mathbf{r}_i$, results in an acceleration $\mathbf{a}_i$ being provided to an atom with mass $m_i$. In Newtonian mechanics, the position, $\mathbf{r}_i(t + \delta t)$, of a particle after a certain time, known as the timestep, $\delta t$, has elapsed is calculated using the initial position of the particle, $\mathbf{r}_i(t)$, its initial velocity, $\mathbf{v}_i(t)$, and its initial acceleration

$\mathbf{a}_i(t)$:

$$\mathbf{r}_i(t+\delta t) = \mathbf{r}_i(t) + \mathbf{v}_i(t)\delta t + \frac{1}{2}\,\mathbf{a}_i(t)\delta t^2 \tag{2.11}$$

$$\mathbf{v}_i(t+\delta t) = \mathbf{v}_i(t) + \mathbf{a}_i(t)\delta t \tag{2.12}$$

One issue with these equations of motion is that they assume $\mathbf{v}$ and $\mathbf{a}$ remain constant for one time step, until they are recalculated for the next timestep, which is not the case for a true, physical system case and can result in catastrophic energy drift. An integration method is therefore required to solve the equations of motion to an acceptable level of accuracy. The Verlet algorithm [104, 105] is widely used for integrating the equations of motion due to its low drift and stability. It uses the position and acceleration at time $t$ with the positions of the previous step $\mathbf{r}_i(t-\delta t)$ to predict the positions at the next time step $\mathbf{r}_i(t+\delta t)$. The previous and future positions can be written as:

$$\mathbf{r}_i(t-\delta t) = \mathbf{r}_i(t) - \mathbf{v}_i(t)\delta t + \frac{1}{2}\,\mathbf{a}_i(t)\delta t^2 \tag{2.13}$$

$$\mathbf{r}_i(t+\delta t) = \mathbf{r}_i(t) + \mathbf{v}_i(t)\delta t + \frac{1}{2}\,\mathbf{a}_i(t)\delta t^2 \tag{2.14}$$

Combining these equations gives:

$$\mathbf{r}_i(t+\delta t) = 2\mathbf{r}_i(t) - \mathbf{r}_i(t-\delta t) + \mathbf{a}_i(t)\delta t^2 \tag{2.15}$$

From this equation the algorithm can be seen to require the previous position, $\mathbf{r}_i(t-\delta t)$, which will not be available for the first step and therefore must be approximated initially. The algorithm method is illustrated Figure 2.4 (adapted from [106]).

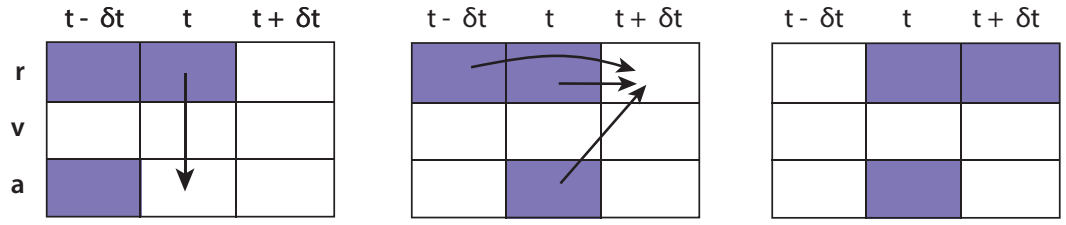


FIGURE 2.4: Schematic representation of the Verlet algorithm

The Verlet algorithm is properly centred, as $\mathbf{r}_i(t+\delta t)$ and $\mathbf{r}_i(t-\delta t)$ play symmetric roles in Equation 2.15, making this method time reversible. An algorithm that is time reversible is able to retrace the trajectories of the system by reversing the momenta of the particles. The Verlet algorithm does not evaluate velocities. They can be estimated by truncating Equation 2.15 after the second term and rearranging the variables to give:

$$\mathbf{v}_i(t) \;=\; \frac{\mathbf{r}_i(t \;+\; \delta t) - \mathbf{r}_i(t \;-\; \delta t)}{2\delta t} \tag{2.16}$$

This has a second order truncation error, which results in the kinetic energies calculated from these velocities being less accurate than the potential energies calculated using Equation 2.15.

The velocity Verlet algorithm is an alternative method and is illustrated in Figure 2.5. It is numerically equivalent to the Verlet algorithm, however it stores the velocities as well as the positions and accelerations at the same timestep. The velcoity Verlet algorithm is the integration method used within DIPPIM and can be written as [106]:

$$\mathbf{r}_i(t+\delta t) \;=\; \mathbf{r}_i(t) \;+\; \mathbf{v}_i(t)\delta t \;+\; \frac{1}{2}\,\mathbf{a}_i(t)\;\delta t^2 \tag{2.17}$$

$$\mathbf{v}_i(t+\delta t) \;=\; \mathbf{v}_i(t) \;+\; \frac{1}{2}\,[\mathbf{a}_i(t) \;+\; \mathbf{a}_i(t+\delta t)]\;\delta t \tag{2.18}$$

The new positions at $(t+\delta t)$ are determined using Equation 2.17 and the velocities are calculated at mid-step $(t+\frac{1}{2}\delta t)$ using:

$$\mathbf{v}_i(t+\frac{1}{2}\delta t) = \mathbf{v}_i + \frac{1}{2}\,\mathbf{a}_i(t)\;\delta t \tag{2.19}$$

This is used to calculate the forces and accelerations at $(t+\delta t)$ and the velocity move is then completed:

$$\mathbf{v}_i(t+\delta t) \;=\; \mathbf{v}_i(t \;+\; \frac{1}{2}\,\delta t) \;+\; \frac{1}{2}\,\mathbf{a}_i(t \;+\; \delta t)\;\delta t \tag{2.20}$$

In classical MD, the forces on each particle are determined using an interatomic potential. Once the forces have been determined, the structure and velocities are updated after the pre-defined timestep, to reflect the new atomic conditions.

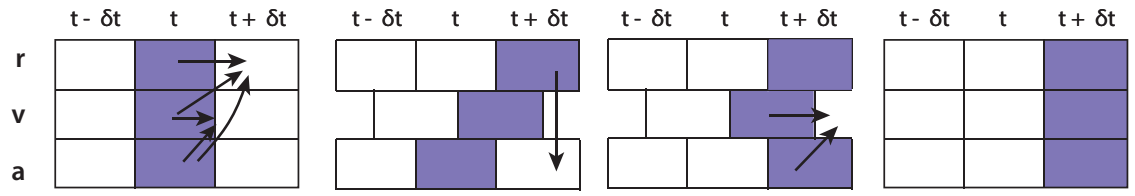


FIGURE 2.5: Schematic representation of the velocity Verlet algorithm

#### 2.2.1.3 Timestep

When selecting the timestep for the simulation a number of factors must be considered. A smaller timestep will result in a more accurate representation of the trajectory of the system, however if the timestep is too small the trajectory covered in that time will only be able to explore a small amount of the phase space (Figure 2.6(a)). The phase space for a system containing N atoms is made up of (3+3)N values that describe each combination of coordinate (3N) and momenta (3N). The timestep must be small enough to observe all atomic motion, such as vibrations. If the timestep is too large it will not be able to accurately track the motion of the atoms, which can result in atoms moving too great a distance in one timestep, causing instabilities within the system (Figure 2.6(b)). When an appropriate timestep is used, the phase space is efficiently explored and all motion is observed (Figure 2.6(c)).

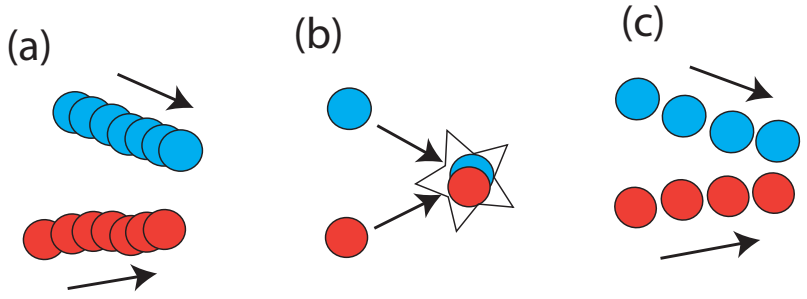


FIGURE 2.6: Selecting timestep is important, if it is (a) too small, very little of the phase space is explored, (b) too large, can result in instabilities (c) appropriate, phase space is efficiently explored and collisions occur more gently

#### 2.2.1.4 Equilibration

Due to the fact that the inital structure and velocities were assigned at the start of the simulation, it is unlikely they will resemble the true characteristics on the materials, unless they were obtained from a system that had been previously simulated. The system must therefore be allowed come to equilibrium so that the original configuration is rearranged to resemble that which is representative for the system for the given temperature. Once it is confirmed that the system has reached thermal equilibrium, by plotting the energies as a function of time, the production run can begin, and it is from this final production run that the data to be analysed is obtained.

### 2.2.2 Ensembles

An ensemble relates the microscopic information obtained from MD simulations, to macroscopic properties, such as temperature, pressure and volume. The ensemble defines the conditions under which the system will be investigated. In this study the isothermal-isobaric ($NPT$) [107] and canonical ($NVT$) [108] ensembles are used. When using the $NPT$ ensemble, the number of particles within the system and the temperature and pressure of the system remain constant. The $NVT$ ensembles ensures the number of particles, the temperature and the volume of the system remain constant.

One way to run a system using a $NPT$ ensemble is in contact with a thermostat at temperature $T$ and a barostat at pressure $P$. The system is allowed exchange heat with the thermostat in order to bring it to thermal equilibrium and is allowed exchange volume with the barostat to bring it to constant pressure. The total energy and volume of the system fluctuate at thermal equilibrium when using this ensemble.

The $NVT$ ensemble is therefore used for systems where the volume must remain fixed, such as strained bulk systems and surface slabs. Constant volume is required to prevent the system expanding or contracting to remove the strain and to keep the surface area constant. As the $NVT$ ensemble is unable to adjust the volume of atomic systems in response to temperature changes, a thermal expansion coefficient is used to scale the system to the appropriate volume for the simulation temperature and interatomic potential used.

## 2.3 Molecular Dynamics Analysis

### 2.3.1 Mean Square Displacement

The average displacement of atoms (of the species being considered) within a system at any given time during the MD simulation is given by the mean squared displacement (MSD):

$$\mathrm{MSD}(t) = \langle \Delta r(t)^2 \rangle = \frac{1}{N} \sum_{i=1}^{N} |r_i(t) - r_i(0)|^2 \tag{2.21}$$

where $N$ is the number of atoms of the species being considered in the system, and $|r_i(t) - r_i(0)|$ is the distance that the $i$'th atom travels in time, $t$. The average of the square of this distance is used (as opposed to just the distance itself) as the average distance covered by an atom is zero, due to the random walk nature of its movement.

The MSD can be used to calculate the diffusion coefficient, $D$, of the ions:

$$\langle \Delta r(t)^2 \rangle = 2SDt + C \tag{2.22}$$

where $S$ is the dimension of space being considered, so for the 3-dimensional analysis conducted on a bulk system, the plot of MSD against time has a slope, $6D$ (as demonstrated in Figure 2.7).

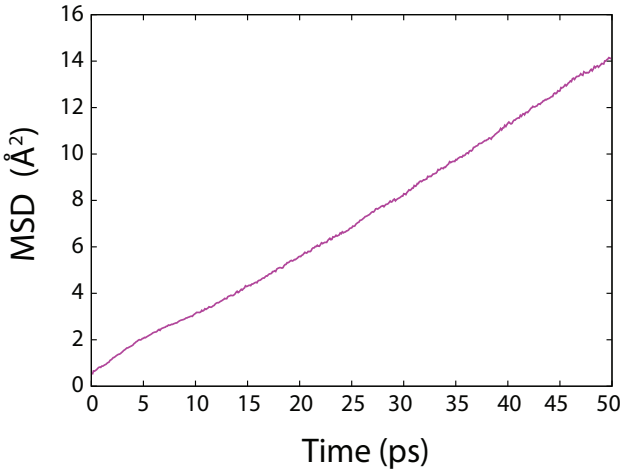


FIGURE 2.7: MSD of $F^-$ ions diffusing within the $CaF_2$ lattice at 1473K

#### 2.3.1.1 Multiple Time Origin Mean Square Displacement

An alternative to the standard, single time origin method for calculating the mean square displacement of a system is to use multiple time origins. Multiple time origin MSDs are produced by calculating the MSD at various time origins and determining the average of these MSDs. This method provides an MSD with an error $\sqrt{O}$ times smaller than the standard method, where $O$ is the number of time origins [109].

#### 2.3.1.2 Activation Energy

The diffusion coefficients of the system across a range of temperatures can be used to calculate the activation energy of the diffusing ions, $E_A$, using the equation [46]:

$$D = D_0 \exp\left(-\frac{E_A}{RT}\right) \tag{2.23}$$

where $D_0$ is the diffusion pre-exponential factor, $R$ is the universal gas constant and $T$ the temperature. Rearranging Equation 2.23 gives:

$$\ln D = \ln D_0 + \left(-\frac{E_A}{R}\right)\left(\frac{1}{T}\right) \tag{2.24}$$

which indicates that by plotting the reciprocal of the temperature along the x axis against the natural log of the diffusion coefficient on the y axis will result in a curve with intercept $D_0$ and slope $-\frac{E_A}{R}$. Figure 2.8 shows a plot of $\frac{1}{T}$ against ln $D$ for two systems. The red curve has a steeper slope than that of the purple line, indicating that the system represented by the red curve will have a higher activation energy than the purple.

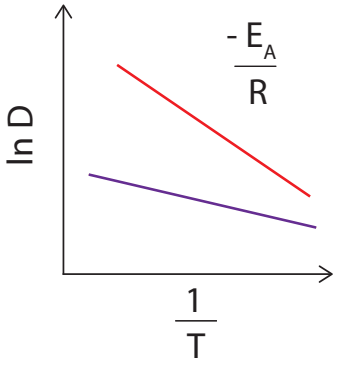


FIGURE 2.8: Plotting $\frac{1}{T}$ against ln $D$ results in curves, with slope $-\frac{E_A}{R}$. The red line has a steeper slope, indicating a higher activation energy than the purple line.

#### 2.3.1.3 Ionic Conductivity

The calculated D value can be used with the Nernst-Einstein equation to determine the ionic conductivity, $\sigma_i$, of the system:

$$\sigma_i = \frac{c_i z_i^2 e^2 D_i}{H_R k_B T} \tag{2.25}$$

where $c_i$ and $z_i$ are the concentration and ionic charge of charge carriers (for both $CaF_2$ and YSZ this refers to the anion) respectively, $e$ is the elementary charge, $k_B$ is Boltzmann's constant and $T$ is the temperature. $H_R$ is the Haven ratio, which is dependent on the mechanism of ionic transport. For vacancy diffusion within an FCC lattice this Haven ratio is equal to the tracer correlation factor, $f$ [110], where $f$ describes the correlation between the jump directions of a given atom (the tracer) and $f = 1$ means there is no correlation.

$H_R$ is defined as being the ratio of the diffusion directly measured from experiment, e.g. tracer diffusion coefficient, $D^*$, to the diffusion coefficient that is dependent on the ionic conductivity, $D_i$ [111, 112]:

$$\mathrm{H}_R = \frac{D^*}{D_i} \tag{2.26}$$

One of the origins of the difference between $D^*$ and $D_i$ arises from the fact that when the conductivity is measured experimentally the results differ depending on whether the results are being taken under an applied field or not. Ions travel in an uncorrelated fashion if under an applied field, however this motion becomes correlated if there is no field applied [112]. The degree of correlation of the successive jumps of the tracer ion is also dependent on the structure of the crystal lattice. For simulation calculations, $D^* = D_i$, therefore $H_R$ equals 1.

### 2.3.2 Radial Distribution Function

The radial distribution function (RDF), also known as the pair correlation function, provides information on the atomic structure of the system being studied, which can be compared with experimental data e.g. neutron diffraction [99]. It calculates the average distribution of atoms relative to each other by giving the probability of finding an atom a certain distance away from another atom (the atoms can be the same or different species). The RDF, $g(r)$, is described mathematically by:

$$g(r) = \frac{n(r)}{\rho 4\pi r^2 \Delta r} \tag{2.27}$$

where $n(r)$ is the number of atoms that exist in a shell of width $\Delta r$, a distance $r$ away from the atom being considered (demonstrated graphically in Figure 2.9), and $\rho$ is the number of particles per unit volume. $g(r)$ is an equilibrium property of the system, meaning that its calculated value is independent of time and the atom chosen to be the central atom [42].

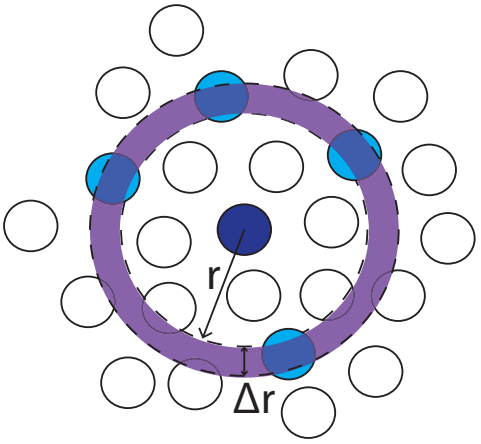


FIGURE 2.9: A schematic demonstrating that four (light blue) atoms are within the shell of width Δr at distance r from the central (dark blue) atom.

A plot of $g(r)$ against interatomic distance, $r$, enables the visualisation of shells existing within the material and allows for the determination of coordination number. These shells are signalled by the presence of peaks, which, if they persist for long range $r$ values, indicate that there is a high degree of ordering, implying that the system is crystalline. At very long range, the value of $g(r)$ tends to 1, as demonstrated in Figure 2.10, illustrating the decline in ordering with range.

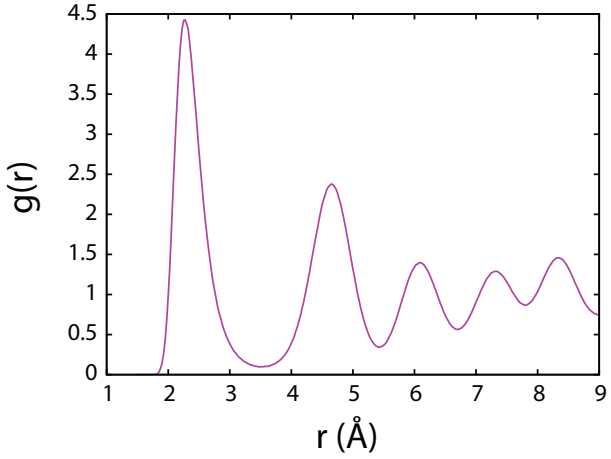


FIGURE 2.10: F-Ca RDF for bulk $CaF_2$ at 1473K

The partial RDFs can be used to determine the coordination number, $n$. The nearest neighbour coordination number is calculated by integrating the peak from 0 to the position of the first minimum, $r_c$:

$$n = 4\pi\rho \int_0^{r_c} r^2 \, g(r) \, dr \tag{2.28}$$

where $\rho$ is the density of coordinating atoms in the system.

### 2.3.3 Vacancy Analysis

Vacancies can be inherently present in a material, or can be introduced as an extrinsic defect by, for example, doping the system. These vacancies can interact with other atoms and other vacancies within the material, which can have an effect on the properties on the system. In this study, the lattice sites for the system before the simulation are defined as the base structure of the system and are used for vacancy analysis. During the simulation, at each frame (MD step) each atom within the system is assigned to one of these lattice sites, determined as being the closest site at that time. These base structure lattice sites can therefore be unoccupied, or occupied with one or more atoms, depending on the system and the simulation environment. Unoccupied lattice sites are defined as being vacant and can be used for analysis.

The effect vacancies have on the structure of a system can be investigated through examination of vacancy RDFs. Since these vacancies are always defined as being located on a lattice site and as vacancies cannot be affected by thermal vibrations, vacancy RDFs are much sharper than partial RDFs not concerned with vacancies. Vacancy RDFs allow for the local ordering of vacancies to be investigated, and the vacancy-vacancy coordination number, $n_{v-v}$, can be obtained by using an adaptation of Equation 2.28:

$$n_{v-v} = 4\pi\rho \int_0^{r_c} r^2 \, g_{v-v}(r) \, dr \tag{2.29}$$

where $\rho$ is the density of vacancies in the system.

# Chapter 3: Calcium Fluoride Analysis

## 3.1 Introduction

Calcium fluoride is a superionic conductor, where the $Ca^{2+}$ cations form a rigid lattice structure through which the $F^-$ anions, with a smaller relative electrical charge, diffuse. The temperature at which $CaF_2$ begins to transition to the superionic state has been reported experimentally to be 1100K [3]. The diffusion of $F^-$ ions in $CaF_2$ has been investigated via experimental means for decades, by measuring the ionic conductivity of $CaF_2$ crystals [113–115] and was then later investigated by molecular dynamics as one of the first bulk ionic materials [116–122].

Rahman's study of $CaF_2$ in 1976 [116] was the first demonstration that molecular dynamics could be used to investigate the superionic nature of a system. $CaF_2$ was chosen to be studied due to its relatively good approximation to a rigid-ion model. Although only a small system (108 cations and 216 anions) was analysed, it confirmed the rigid $Ca^{2+}$ sublattice with diffusing $F^-$ ions and a high diffusion coefficient at 1590K. In 1978, Rahman and Jacucci analysed the point defects within the $CaF_2$ system to further the understanding of the mechanism by which the $F^-$ anions diffuse [121]. They determined that the high diffusion coefficient of the $F^-$ anions is due to a few exceptional mobile ions jumping from their lattice site, generally as a result of generation and recombination events. In the majority of cases ($\sim$80%) these jumps occurred along the (100) direction. This was corroborated by Dixon and Gillan [123] who found that $\sim$89% of $F^-$ anions diffuse in the (100) direction as a result of a hopping mechanism.

In recent years the field of materials chemistry has become increasingly interested in the effect of grain boundaries on a crystal system. Experimentally, the presence of facile pathways through bulk $CaF_2$ has been confirmed via NMR analysis by the study of $F^-$ anion diffusion, demonstrating two distinct diffusivities, with the faster being attributed to conduction through the grain boundary while the slower diffuses through the bulk. The inclusion of these facile diffusion pathways proved to increase the overall diffusion of the $CaF_2$ system than compared to the single crystal $CaF_2$ [124].

There have been very limited computational investigations into $CaF_2$ grain boundaries, with the most recent paper demonstrating a $CaF_2$ grain boundary structure, demonstrating that of the $\Sigma5(310)$ structure, was published in 2010 [125]. The last computational work investigating the diffusion of a $CaF_2$ grain boundary was carried out in 1990 on the $\Sigma5(210)$ [126]. This study utilised a rigid-ion potential and a fluorite bicrystal containing 4320 atoms to carry out MD simulations for temperatures ranging from 250K - 1500K.

Despite the scarcity of studies into $CaF_2$ grain boundaries there have been multiple studies into the grain boundaries of other fluorite structured systems, such as $UO_2$ [127, 128], $CeO_2$ [5, 6], and yttria-stabilised cubic zirconia [129–132]. The $CaF_2$ grain boundary structures generated in this study can be compared and contrasted to these fluorite grain boundaries, due to the nature of their shared fluorite structure.

The work in this study utilises molecular dynamics to investigate the ionic diffusion in $CaF_2$. $CaF_2$ was selected as a model fluorite material, due to its characteristically fast ionic diffusion. The bulk structure of $CaF_2$ was initially modelled for a range of temperatures. The system was cleaved in various orientations, using METADISE to generate surfaces and grain boundaries. These interfaces were then investigated by studying their ionic diffusion properties, both at the surface/boundary, and examining how the surface/boundary effects of different orientations propagated into the system. The structure of all the grain boundaries constructed were compared to other experimental fluorite structured boundaries, such as YSZ and $CeO_2$, to establish the validity of the model. The ionic diffusion along the grain boundary, was investigated and compared with that of the bulk and also with the corresponding grain boundaries of other previously studied fluorite crystals. The information gained here on the structure and ionic diffusion of the grain boundaries will allow us to apply it to other fluorite structure grain boundaries, such as in slower diffusing oxide ion materials, which are commonly used in electrochemical devices.

## 3.2 Methodology

### 3.2.1 Bulk

To investigate the properties of bulk $CaF_2$, a $6 \times 6 \times 6$ supercell, with box length 33Å, containing 2592 atoms, was created. This system was examined to determine its thermal expansion and ionic conductivity. The effect that the presence of Schottky defects had on the properties of the bulk system was also investigated. 1.16% of the $Ca^{2+}$ and $F^-$ ions were randomly removed, generating Schottky defects within the $6 \times 6 \times 6$ $CaF_2$ supercell (i.e. 10 $Ca^{2+}$ and 20 $F^-$ ions removed from the 2592 atom system).

### 3.2.2 Interfaces

The materials used for constructing diffusion based devices will contain hetero-interfaces, therefore the effect that surface and grain boundaries have on the properties of $CaF_2$ were investigated. The computer simulation code METADISE [133] was used to cleave the surfaces from the bulk cell, and to generate grain boundaries. Six surfaces were generated, the (100), (110), (111), (210), (310) and (221). These surface slabs were all expanded to ensure their thickness was at least 35Å, and a vacuum gap of 40Å was inserted to prevent the surfaces from interacting with one another (as demonstrated in Figure 3.1).

Seven grain boundaries were constructed, the $\Sigma3(111)$, $\Sigma5(210)$, $\Sigma5(310)$, $\Sigma9(221)$, $\Sigma11(332)$, $\Sigma13(320)$ and the $\Sigma13(510)$, using METADISE, with previously derived shell model parameters [134]. METADISE was used to identify the most stable structures of each of the grain boundaries by generating a 2-dimensional potential energy surface (PES). Each PES was constructed by reflecting the surface slab perpendicularly to the surface and scanning across the interface in approximately 0.25Å steps. This scan was carried out at constant force, which resulted in the optimisation of the height perpendicular to the grain boundary and generated an optimised grain boundary structure. Once generated, the grain boundary slabs were expanded to give a supercell containing two grain boundaries of the same orientation, with thickness of at least 70Å (see Figure 3.1).

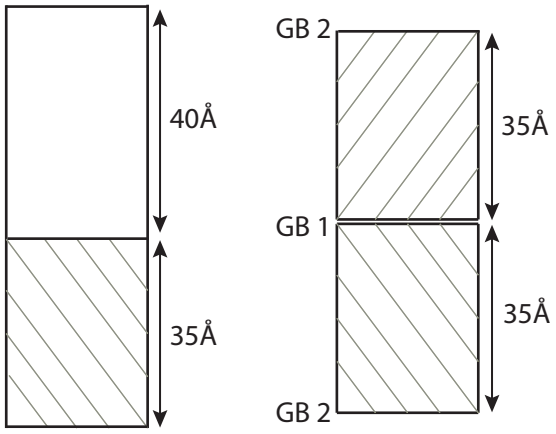


FIGURE 3.1: Left: Surface schematic showing the 35Å surface slab with the 40Å vacuum gap , Right: Grain boundary schematic showing the two grain boundaries (GB1 and GB2) separated by 35Å

### 3.2.3 Strain

The hetero-interfaces generated in diffusion based devices can introduce strain into the crystal system, which can effect the properties of the system. The bulk and surface slabs therefore had both tensile and compressive strains ($\pm1$, $\pm2$ and $\pm4\%$) applied by straining the system in two dimensions. This was done in order to obtain results that can be compared with experiment, where strain is introduced via lattice mismatch, and can therefore only be applied in two dimensions. Strains greater than 4% were not considered, due to reports of higher strains inducing lattice distortions, which have a negative effect on the ionic conductivity of the system [85].

### 3.2.4 Simulation Information

The $CaF_2$ systems were optimised using the conjugate gradient based optimiser within the PIMAIM MD code before undergoing temperature scaling. All unstrained bulk systems were investigated at 200K intervals from 273K to 1473K and at 100K intervals from 1473K to 2273K. The bulk system containing Schottky defects was investigated at 200K intervals within the 1273 - 1873K temperature range. All strained bulk systems, surfaces (both unstrained and strained), and grain boundaries were investigated at 1473K, 1573K, and 1673K. Three simulations were performed for each temperature to take the random nature of the initial ion velocities assigned to the atoms into account, and by taking the average of these three runs, the statistical significance of the result is improved, and standard error can be

calculated. Each system was initially temperature scaled to the desired temperature every 25fs for 5ps, before being equilibrated for 10ps. This was followed by a production run lasting 50ps for the unstrained bulk and 25ps for all other systems. All simulations were carried out using a timestep of 5fs, with a short range cut-off of 14Å. All unstrained bulk calculations and grain boundaries were run using the isothermal-isobaric ($NPT$) ensemble, whilst the strained bulk systems and the surface slabs used the canonical ($NVT$) ensemble (using volumes scaled by the thermal expansion coefficients calculated from the bulk).

#### 3.2.4.1 Grain Boundary Structure

The lowest energy grain boundary structure, predicted by METADISE, was optimised using the DIPPIM, implemented in PIMAIM. This optimised structure was heated to 573K, with a 5ps temperature scaling and 10ps equilibration period followed by a 1ns production run. This was done in order to provide the grain boundary with enough time and energy to potentially rearrange its atomic structure to a lower energy configuration structure, without becoming distorted as a result of temperature effects. The 573K structure was then cooled to 300K, again with a 5ps temperature scaling and 10ps equilibration, and a 200ps production run, to enable the generation of a grain boundary structure that is readily comparable with experimentally constructed boundaries at room temperature.

### 3.2.5 Potential Parameters

The potential parameters used for calcium fluoride were derived by Pyper [97], using *ab initio* data and are given in Table 3.1. They were tested by Wilson et al. [96] by demonstrating that the potential correctly predicted equilibrium crystal properties, such as anion diffusion coefficients, phonon frequencies and the transition pressure from the fluorite to the orthorhombic ($\alpha$-$PbCl_2$) structure.

TABLE 3.1: $CaF_2$ Potential parameters used, all given in atomic units

Repulsive and dispersive parameters

| | $b_{ij}$ | $B_{ij}$ | $C_6$ | $C_8$ | $b_6$ | $b_8$ |
|---|---|---|---|---|---|---|
| $F^-$ - $F^-$ | 2.164 | 122.77 | 28.337 | 477.894 | 2.4 | 2.2 |
| $Ca^{2+}$ - $F^-$ | 1.794 | 59.90 | 16.700 | 251.569 | 2.4 | 2.3 |
| $Ca^{2+}$ - $Ca^{2+}$ | 3.379 | 51240.22 | 10.574 | 144.005 | 3.0 | 2.9 |

Polarisabilities and damping parameters

| | $\alpha$ | $b_{F^--X}$ | $c_{F^--X}$ | $b_{X-F^-}$ | $c_{X-F^-}$ |
|---|---|---|---|---|---|
| $F^-$ | 6.843 | 0.00 | 0.00 | - | - |
| $Ca^{2+}$ | 3.183 | 1.77 | 2.00 | 1.77 | -0.45 |

## 3.3 Bulk

In order to ensure the reproducibility of results for the potential used, properties of bulk $CaF_2$, such as thermal expansion, ionic conductivity and activation energy, were investigated and compared to literature. This examination of bulk $CaF_2$ properties also established a base with which the various properties of strained bulk, bulk containing Schottky defects, surfaces and grain boundaries could be compared.

### 3.3.1 Thermal Expansion

The thermal expansion of the system was compared to results obtained both experimentally and computationally. The linear thermal expansion coefficient, $\alpha_L$, can be calculated for bulk $CaF_2$ using:

$$\frac{L - L_0}{L_0} = \alpha_L \Delta T \tag{3.1}$$

where the initial length of one side of the cubic system, $L_0$, increases to length, $L$, at temperature, $T$. A plot of $\frac{L-L_0}{L_0}$ against temperature for bulk $CaF_2$ demonstrates two curves with different slopes (Figure 3.2), signifying two different expansion coefficients across the temperature range 273 - 2073K. For the low temperature range (273 - 1073K), the linear expansion coefficient was calculated to be $21.9 \times 10^{-6}/K$, which increases to $38.1 \times 10^{-6}/K$ for the high temperature range (1273 - 2073K), comparing well with literature [135–139].

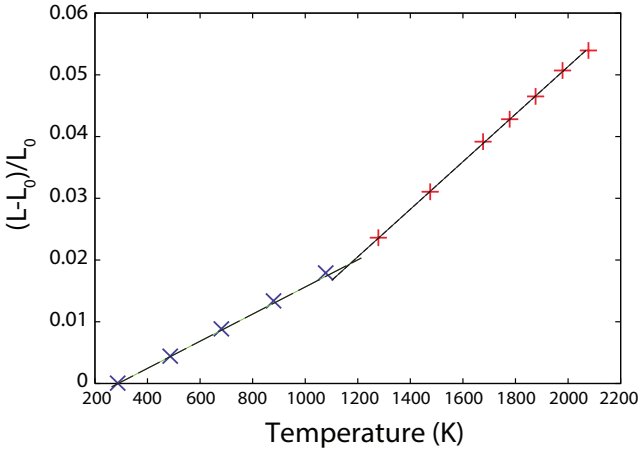


FIGURE 3.2: Bulk linear expansion for bulk $CaF_2$ for the temperature range 273-2073K, exhibiting two curves with different slopes, indicating two different expansion coefficients

The intersection of these two curves occurs at $T = 1176K$, which corresponds with the experimentally calculated temperature at which $CaF_2$ begins to transition to the superionic state at 1100K [3].

### 3.3.2 Diffusion

The mean square displacements (MSDs) obtained for the diffusion of the mobile $F^-$ ions, averaged over three simulations for each temperature, are shown for the temperature range 1473K - 2273K in Figure 3.3. Temperatures lower than 1473K did not provide significant diffusion over this time scale. From Figure 3.3, the MSD at 2173K and 2273K can be seen to have a significantly increased slope compared to the lower temperatures, indicating that the system has melted. This melting temperature is higher than reported literature values (1619-1693K [3, 122, 140, 141]), which could be a consequence of the periodic boundary conditions imposed on the bulk system, effectively generating an infinite lattice, with no surface from which the melting can originate.

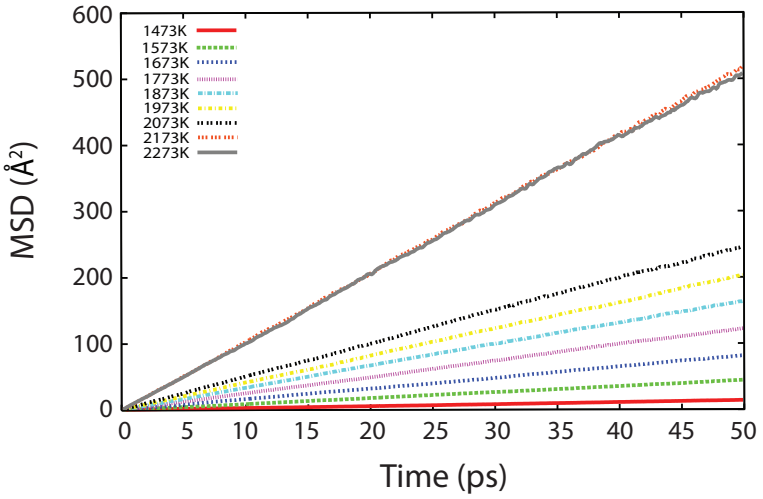


FIGURE 3.3: MSD for bulk $CaF_2$ for temperature range 1473K - 2273K

The diffusion coefficients for the $F^-$ anions for the temperature range 1473K - 2073K were calculated and are given numerically in Table 3.2. The diffusion coefficients outside of this temperature range are not provided as the diffusion was either extremely small due to insufficient ionic movement as a result of too low a temperature, or the system had melted, meaning assigning a diffusion coefficient becomes illogical. The diffusion coefficients in Table 3.2 show an increase with increasing temperature. The statistical significance of the diffusion

coefficient increases as the temperature is increased, due to the increased diffusivity of the system becoming able to overwhelm any conflicting effects present in the system.

TABLE 3.2: Diffusion coefficients of $F^-$ anions for temperature range 1473K - 2073K

| **Temperature (K)** | **Diffusion Coefficient of $F^-$ ions ($\times$ $10^{-5}cm^2/s$)** |
|---|---|
| 1473 | 0.4504 ± 0.0816 |
| 1573 | 1.4663 ± 0.4002 |
| 1673 | 2.7074 ± 0.4555 |
| 1773 | 4.0895 ± 0.1791 |
| 1873 | 5.4462 ± 0.1859 |
| 1973 | 6.7461 ± 0.1412 |
| 2073 | 8.2306 ± 0.1349 |

### 3.3.3 Structural Temperature Effects

The increase in temperature that causes the increase in diffusion coefficient also effects the structure of the system. This structural change can be observed by an examination of how the radial distribution function (RDF) changes with respect to temperature. Figure 3.4 gives the partial F-F RDF of the bulk $CaF_2$ system for the temperature range, 1473K - 2173K. It demonstrates the broadening peaks observed for higher temperature simulations, indicating that the atoms are not as rigidly confined to their lattice position and are experiencing increased thermal vibrations. Looking at the temperature at which the system has been seen to melt, 2173K, the majority of the crystal structure, particularly the long range order, has been lost.

### 3.3.4 Ionic Conductivity

The ionic conductivities of the system at various temperatures were calculated. Figure 3.5 shows the conductivities calculated in this study, both with and without Schottky defects, compared to previously obtained results from Dent et al. [2], and Voronin and Volkov [3], and Ivanov-Shitz [4].

It was found that as the temperature increased, the difference between the diffusion coefficients for the $CaF_2$ bulk system with and without added Schottky defects, decreased. The percentage increase in ionic conductivity as a result of the added Schottky defects decreased

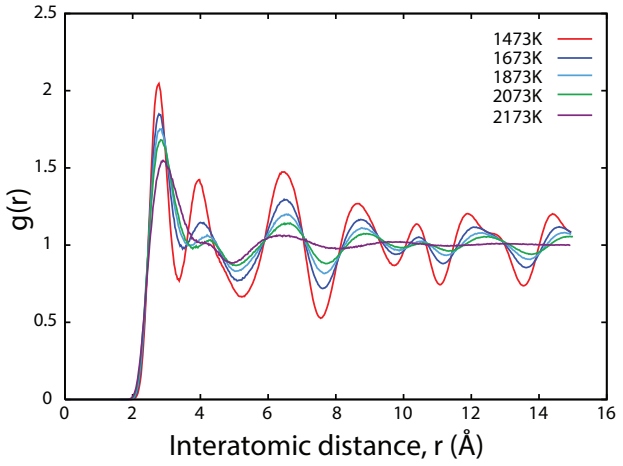


FIGURE 3.4: F-F RDF for bulk $CaF_2$ for temperature range 1473K - 2173K

dramatically from 470% at 1273K, to 4% at 1873K. This decrease is likely due to the ionic diffusion that occurs as a result of the added defects, becoming overpowered by the thermal diffusion. The overall effect that the Schottky defects have on the diffusion at higher temperatures is extremely small and these defects are consequently neglected in further investigations.

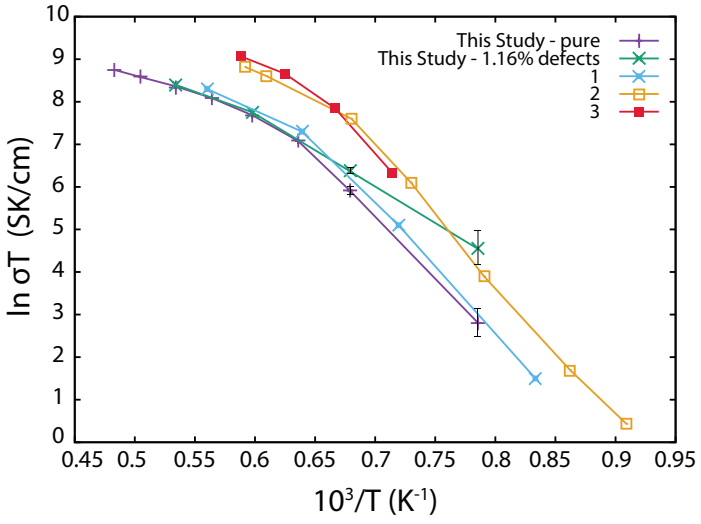


FIGURE 3.5: Comparison of ionic conductivities calculated in this study and from literature; designated as 1 [2], 2 [3] and 3 [4]

The ionic conductivity values calculated were found to be comparable with those obtained by Dent et al. [2], their results exhibited the same trend in slope of the curve, with values

approximately 3-7% higher than those determined here. Dent et al. utilised the same potential as in this study, demonstrating the reproducibility of results for the potential used. The ionic conductivities were also found to be similar to other literature results, obtained both computationally [4] and experimentally [3] (with conductivities values ≈25% higher than those determined in this work), illustrating the accuracy of the potential used. Differences between the results from this study, and those from experiment could be as a result of assuming uncorrelated atomic motion of the charge carriers in Equation 2.25.

The results obtained via simulation methods have a superior statistical quality at higher temperatures (above ≈ 1400K) than lower temperatures [2], due to the generation of more facile Frenkel defects, meaning the conductivity is calculated from the motion of a large number of Frenkel defects and any small fluctuations are overwhelmed.

#### 3.3.4.1 Activation Energy

The activation energy of the diffusing $F^-$ ions is another property that can be compared with literature values to test the ability of the potential to reproduce experimental results. In this study the activation energy was calculated using the diffusion coefficients from the MSD and the Arrhenius equation (Equation 2.23). Three activation energy regimes were found, as demonstrated by the three distinct slopes of the curve shown in Figure 3.6. The activation energies are given in Table 3.10. These values are comparable to literature [2–4, 114], further highlighting the ability of the potential to correctly simulate the properties of the $CaF_2$ system.

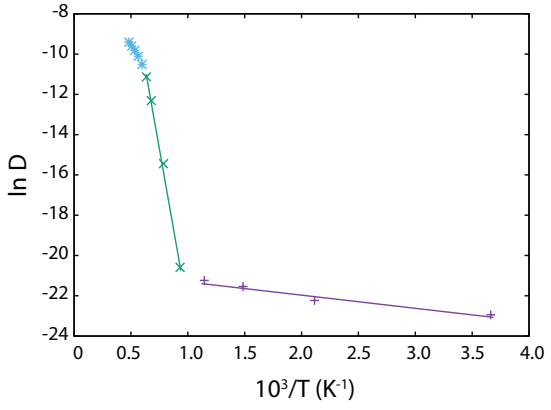


FIGURE 3.6: Arrhenius plot of the diffusion of bulk $CaF_2$, demonstrating the three distinct slopes, giving rise to three activation energies

TABLE 3.3: Activation energies calculated using Equation 2.23 and the slopes from Figure 3.6

| **Temperature range (K)** | **$E_A$ (kJ/mol)** |
|---|---|
| **273 - 873** | 5.545 ± 0.002 |
| **1073 - 1573** | 265.743 ± 18.055 |
| **1673 - 2073** | 79.153 ± 0.112 |

### 3.3.5 Strained Bulk

The materials used for constructing diffusion based devices will contain hetero-interfaces, which can induce strain into the system. A strained system can have different properties, such as ionic diffusion, to its unstrained counterpart. It is therefore vital to understand the effect of strain (both tensile and compressive) in order to be able to optimise the efficiency of these devices.

#### 3.3.5.1 Diffusion

The diffusion coefficients for bulk $CaF_2$ for a range of tensile and compressive strains ($\pm1$, $\pm2$ and $\pm4$ %) were determined by straining the bulk system in two dimensions. This was done in order to obtain results that can be compared with experiment, where strain is introduced via lattice mismatch, and can therefore only be applied in the 2-D plane of the interfaces.

The diffusion coefficients ranging for 4% tensile to 4% compressive strain at 1473K, 1573K and 1673K are given in Table 3.4. Figure 3.7 is a graphical representation of Table 3.4 and clearly demonstrates that the diffusion coefficient of the bulk system at each of the three temperatures studied increases with increasing tensile strain. The application of compressive strains was found to result in a decrease in diffusion coefficient, relative to the unstrained system. Both of these cases correlate with previous literature findings of fluorite structured systems [66, 67, 80, 81, 85, 86, 142].

TABLE 3.4: Diffusion coefficients ($\times10^{-5}$cm $^2$/s) for bulk $CaF_2$ for the strain range +4% to -4% for the temperature range 1473K - 1673K

| | **1473K** | **1573K** | **1673K** |
|---|---|---|---|
| **+4%** | 2.160 ± 0.014 | 3.357 ± 0.028 | 4.868 ± 0.120 |
| **+2%** | 1.173 ± 0.020 | 2.323 ± 0.037 | 3.676 ± 0.042 |
| **+1%** | 0.677 ± 0.007 | 1.795 ± 0.022 | 3.177 ± 0.009 |
| **0%** | 0.437 ± 0.003 | 1.303 ± 0.008 | 2.790 ± 0.121 |
| **-1%** | 0.286 ± 0.009 | 1.042 ± 0.009 | 2.406 ± 0.019 |
| **-2%** | 0.158 ± 0.008 | 0.897 ± 0.013 | 2.195 ± 0.007 |
| **-4%** | 0.087 ± 0.002 | 0.716 ± 0.023 | 2.419 ± 0.048 |

There is, however, a slight discrepancy for the 4% compressive strain at 1673K, which shows an increase in diffusion coefficient up to the 1% compressive strain value for the same temperature. Future work could investigate the diffusion of this highly compressed system for

temperatures between 1573K and 1673K to determine the temperature at which the high strain effect results in a deviation from the expected diffusive behaviour.

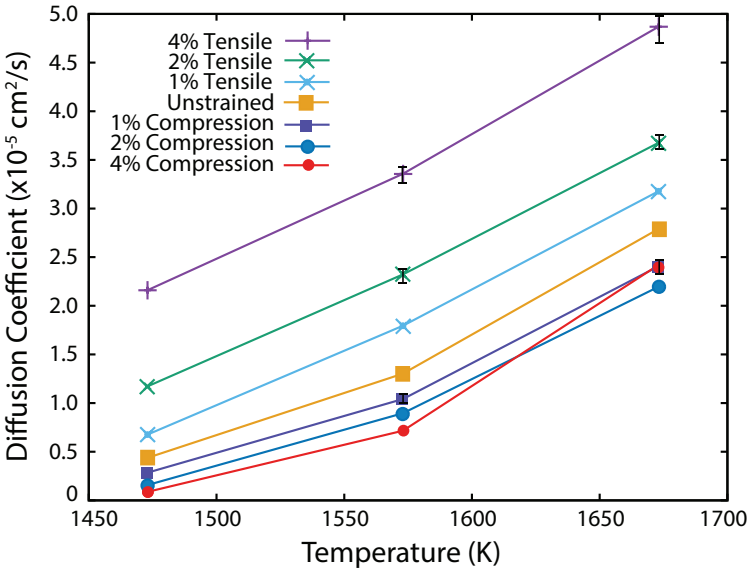


FIGURE 3.7: Comparison of diffusion coefficients for different strains on bulk $CaF_2$

Applying a tensile strain of 4% is seen to provide the largest increase in diffusion coefficient from the unstrained bulk system. This increase is quite substantial, corresponding to an increase from the unstrained bulk diffusion coefficient of 395%, 160% and 75% at 1473K, 1573K and 1673K respectively. The increase in diffusion exhibited at 4% tensile strain is equivalent to that of the unstrained system with a 150K increase in temperature i.e. the diffusion coefficient of the bulk system with 4% tensile strain applied at 1473K is approximately equal to that of the unstrained system at 1623K. The introduction of strain could therefore be feasibly used to increase the ionic conductivity of a system while utilising a lower temperature, which, in some situations, could be easier to maintain.

#### 3.3.5.2 Structure

The increase in diffusion with increasing system volume can be corroborated by examining the average structure of the bulk system over the 25ps production run. Figure 3.8 shows the average structures for the unstrained system and the systems with 4% compressive and 4% tensile strain applied, all run at 1473K. There is a clear increase in $F^-$ ion disorder as the system becomes enlarged, with very little movement observed for the system with 4% compression applied. This trend was observed for all compression and tensile strains across all three temperatures.

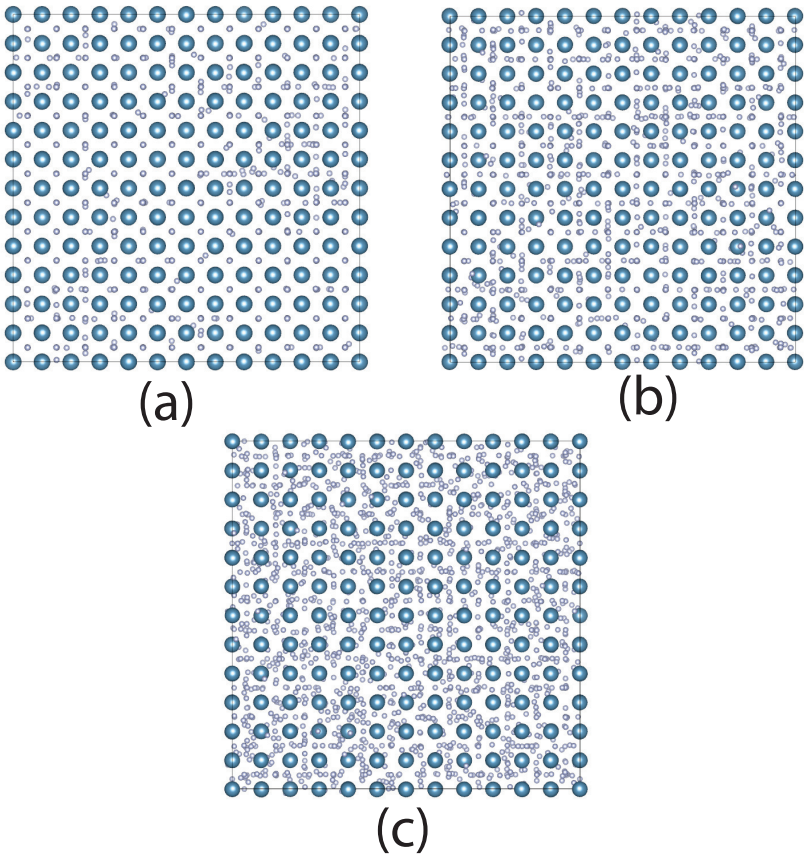


FIGURE 3.8: Average structure over 25ps 1473K production run for (a) 4% compressive strain (b) unstrained and (c) 4% tensile strain applied

The partial radial distribution functions for Ca-Ca, F-Ca and F-F were examined for all tensile and compressive strains investigated, to examine their effect on the structure of the system. Similar behaviour was found for all three temperatures studied for each strain, with

the temperature effecting only the broadness and height of the peaks (as for the unstrained bulk RDF, Figure 3.4). Figure 3.9 demonstrates the RDFs for all strains at 1673K.

The application of tensile strain results in broader, shorter peaks, indicating a more distorted structure in both sublattices, and is consistent with the crystal lattice structure being expanded, resulting in greater distances between ions. This broadening for high tensile strains can also be attributed to the increased vibration of the cations around their equilibrium positions, as observed in previous works [142]. Conversely, the highly compressed system exhibits sharper, taller peaks, indicative of a more constrained system. This is consistent with the diffusion data previously analysed.

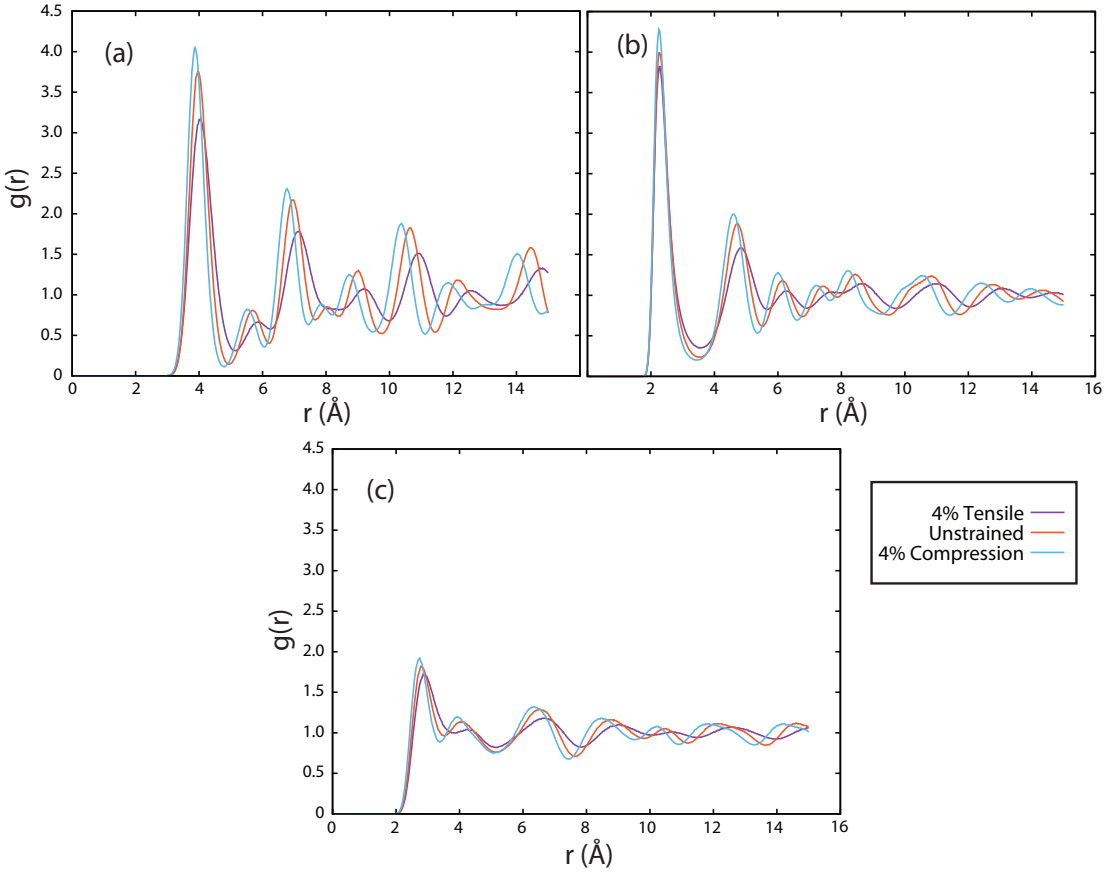


FIGURE 3.9: Transformation of radial distribution function, g(r), with tensile and compressive strain at 1673K: (a) Ca-Ca, (b) F-Ca and (c) F-F

The RDFs of both F-Ca and F-F (Figures 3.9(b) and (c) respectively) exhibit similar behaviour for both tensile and compressive strain as observed for the Ca-Ca RDFs. That is,

the peaks demonstrate a broadening with tensile strain, as the system is being expanded, and are narrower for compressive strain, as the system is being condensed.

## 3.4 Surfaces

The (100), (110), (111), (210), (221) and (310) $CaF_2$ surfaces were investigated by examining the 2-dimensional planar diffusion along slices of the surface slab, parallel to the surface plane. This enables the identification of the surface effects on the ionic diffusion, and allows a comparison of the extent of change in diffusivity at the various surface orientations, compared to that of the bulk. The six surfaces studied can be classified according to Tasker [53]; the (110) and (310) are type I, the (111) is type II and the (100), (210) and (221) are all type III.

### 3.4.1 Surface Stability

The surface energies of each $CaF_2$ surface orientation studied were calculated for the optimised surface structure, using Equation 3.2, which can be rewritten as:

$$\gamma = \frac{\mathrm{E}_{slab} - \mathrm{nE}_{bulk}}{2\mathrm{A}} \tag{3.2}$$

where $\mathrm{E}_{slab}$ is the total energy of the supercell slab containing the surfaces, n is the number of formula units in the supercell, $\mathrm{E}_{bulk}$ is the bulk energy per formula unit, A is the area of the surface plane within the supercell and 2 is the number of identical surfaces present in the supercell.

The surface energies were compared with one another in order to establish whether there was a trend in stability and whether the same trend was observed in literature surface energy values of $CaF_2$ and other fluorite-structured surfaces. Table 3.5 gives the surface energies calculated for $CaF_2$ surfaces. These values are listed according to their relative order of stability, where a low $\gamma$ indicates a high surface stability and vice versa.

TABLE 3.5: Calculated surface energies, $\gamma$, for various $CaF_2$ surfaces (in $Jm^{-2}$), listed according to their order of stability

| **Surface** | **This Work** |
|---|---|
| (111) | 0.134 |
| (110) | 0.164 |
| (210) | 0.180 |
| (100) | 0.208 |
| (221) | 0.215 |
| (310) | 0.240 |

The (111) $CaF_2$ surface is found to be the most stable surface termination, agreeing with both Maldonado et al.'s [143] and Puchin et al.'s [144] studies of $CaF_2$. An increase in $\gamma$ at the (110) surface termination was also observed in all works. The trend in stability found in this work, (111) > (110) > (210) > (100), is mirrored by the work of Maldonado et al., however there is a disagreement with the relative stability of the (310) surface termination. The Hartree-Fock results [144] found a stability order of (111) > (221) > (110) > (100) > (210). Neglecting the values found for the (210) and (221) surface terminations, due to their values being obtained from non-relaxed surfaces, this results in an order of (111) > (110) > (100), agreeing with results found in this study.

The surface energy of various surface terminations of $CeO_2$ have also been investigated, and its relative stability trend agrees closely with that determined here for $CaF_2$. Using a simple interatomic potential model calculation, Conesa [145] found a relative stability order of (111) > (110) > (100)/(210) > (310) which only slightly differs from that found by Jiang et al. [146] using density functional theory, (111) > (110) > (210) > (100) > (310), both of which agree with the order found in this study.

Williams et al. [64] calculated the surface energy of various $UO_2$ surface orientations, using a rigid ion potential. They determined the surface stability order to be (111) > (221) > (310) > (210), which, other than predicting the (111) surface termination to be the most stable, contradicts the order of stability calculated here for $CaF_2$. Their study, however, did observe a correlation between the surface energy and coordination number of the surface uranium atoms, where surfaces with higher coordination numbers had lower surface energies. This trend was observed here for the $Ca^{2+}$ surface ions, as demonstrated in Table 3.6.

TABLE 3.6: The coordination number of the surface (for cation terminated), or closest to the surface (for anion terminated) $Ca^{2+}$ ion, listed according to the order of stability determined from the surface energies calculated in this study.

| **Surface** | **Coordination Number** |
|---|---|
| (111) | 7 |
| (110) | 6 |
| (100) | 6 |
| (210) | 5 |
| (221) | 4 |
| (310) | 4 |

The MD code and potential parameters used for $CaF_2$ have been shown to generate surfaces that accurately represent the surface stability trend found within literature, both for $CaF_2$ systems, as well as other fluorite structured materials.

### 3.4.2 Depth Analysis of Diffusion

The diffusion of each surface slab was investigated as a function of depth, that is, the slab was sliced, parallel to the surfaces, and the diffusion coefficient within each slice was obtained. This allowed for the effect of the surface on diffusion to be investigated separately from the effect of the bulk-like behaviour of the ions within the centre of the slab. The magnitude of diffusion for each of the surfaces could then be compared. The depth profile of each of the surface slabs investigated demonstrated the same general trend in diffusion coefficient in response to surface effects, though the extent and range of these effects varies for each specific surface.

The (310) depth profile is examined here in detail, as it clearly demonstrates the surface effects propagating through the slab, in a manner which is representative of the other surfaces studied. In Figure 3.10 we can see a pronounced increase in the diffusion coefficient at both of the surfaces at 1473K, with a reduction to bulk diffusion levels within the centre of the slab. The average position of the calcium ions over the 25ps 1473K MD run demonstrates disruption at the surfaces, returning to a consistent, rigid, bulk-like lattice structure within the centre of the slab. There is a slightly more distorted structure observed at the top surface, which could account for the slight increase in diffusion coefficient observed in the depth profile, compared to the bottom surface.

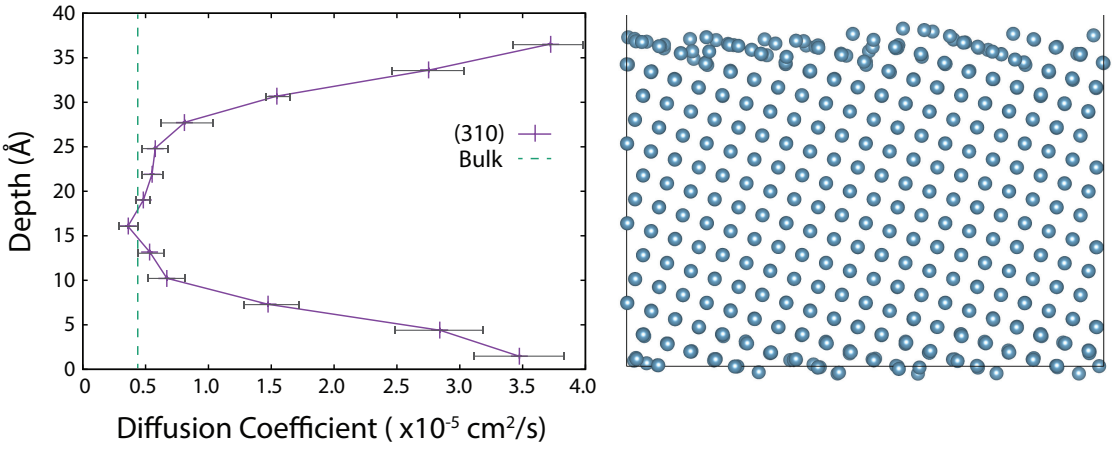


FIGURE 3.10: Depth analysis diffusion profile (left) and average $Ca^{2+}$ positions (right) of the (310) surface, at 1473K ($F^-$ anions have been removed for clarity)

Similar analysis was carried out on the (100), (110), (111), (210) and (221) surfaces. Figure 3.11 shows the depth diffusion profiles for all of the surfaces as a function of percentage depth (as the surfaces generated were not all exactly the same depth) calculated at 1473K. It was found that for all interfaces, the surface of the slab showed an increase in diffusion coefficient, ranging from approximately two to nine times that of the bulk. The diffusion coefficients at the surfaces of all surface orientations are given in Table 3.7. These values are the average of the increase observed at the top and bottom surface. The non-symmetric appearance of the diffusion coefficients at the surfaces is due to the random nature of the ionic diffusion. The inclusion of data from additional runs would therefore be expected to compensate for the statistical nature of the simulation and result in a more symmetric depth profile. The average data from three simulations for each surface and temperature were run, and presented, to attempt to account for this variability. Due to the computational time requirements for each run, it was deemed infeasible to carry out additional runs for each surface at each temperature.

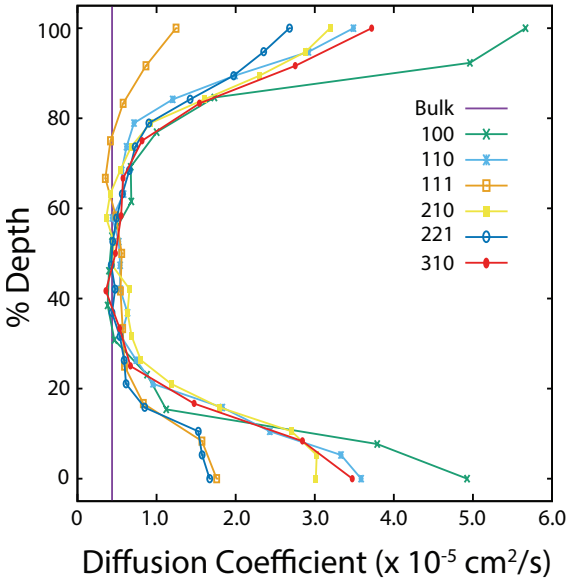


FIGURE 3.11: Comparison of depth analysis diffusion profiles for all surfaces, at 1473K

TABLE 3.7: Average diffusion coefficient, $D$, of top and bottom surface for all $CaF_2$ surface orientations, compared to that of the bulk system, all calculated at 1473K, listed by $D$ value

| **Surface Orientation** | **Diffusion Coefficient** $\times 10^{-5}$ **cm**$^2$**/s** |
|---|---|
| **(100)** | 5.2953 ± 0.3696 |
| **(310)** | 3.5974 ± 0.1222 |
| **(110)** | 3.5375 ± 0.0484 |
| **(210)** | 3.1087 ± 0.0847 |
| **(221)** | 2.1750 ± 0.5037 |
| **(111)** | 1.5035 ± 0.2570 |
| **Bulk** | 0.4375 ± 0.0026 |

The (111) surface demonstrates the lowest increase in diffusion coefficient, while the (100) demonstrates the greatest increase. The same relative increases in diffusion coefficient at the surfaces was also found for both 1573K and 1673K. All surfaces, bar the (111), also demonstrated increased disorder within the cation sublattice at the surfaces, indicating increased atomic movement. The lack of disorder at the (111) surface can be explained by it exhibiting the greatest surface stability (from its low surface energy) and is consistent with its low diffusion increase. Despite the correlation between surface energy and change in diffusion coefficient for the (111) surface, the surface energies cannot be used to explicitly determine the relative increases in diffusion coefficient for all surfaces. For example, from the calculated surface energies (Table 3.5) the (310) is found to be the least stable, and therefore could be expected to exhibit the greatest increase in diffusion coefficient at its surfaces. As seen from Figure 3.11 this is not the case. The (100) is seen to be the surface orientation that displays the greatest increase.

#### 3.4.2.1 Slab Activation Energy

The activation energy of the anions was calculated for each surface slab. The Arrhenius plots for the surfaces and bulk system for comparison are given in Figure 3.12.

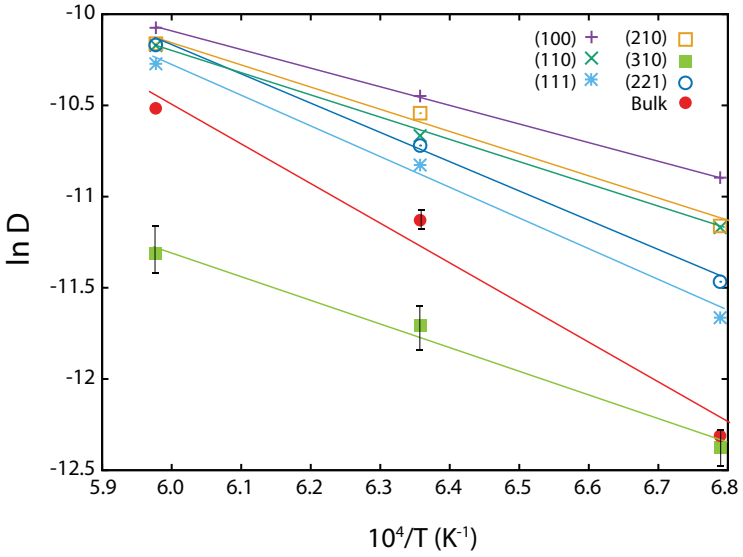


FIGURE 3.12: Arrhenius plot of the diffusion of the $CaF_2$ surfaces at 1473K, 1573K and 1673K

The surface slab activation energies for the $CaF_2$ surfaces are calculated from the slopes from Figure 3.12. These values are given numerically in Table 3.10 and are plotted with the bulk activation energy for the same temperature range in Figure 3.13. The higher activation energy of the bulk system is consistent with the fact that the surface slabs were found to possess diffusion coefficients equal to or greater than that of the bulk (Figure 3.11).

While this analysis demonstrates the decreased activation energy of all surface slabs as a whole, it must be noted that these slabs contain bulk-like regions within the centres of their slabs. As such, the activation energy calculated is not purely based off of the areas of the slab that experience surface effects. This can be explicitly observed by comparing the relative increases in diffusion coefficient at all surface orientations (given in Table 3.7) to the relative activation energies (given in Table 3.10). There is some discrepancy between the relative ordering. It is therefore advantageous to partition these surface slabs into regions that display bulk-like properties and regions that are effected by the presence of the surface.

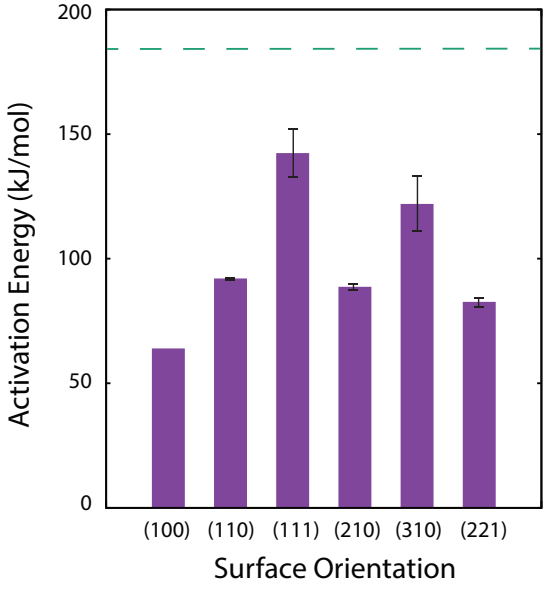


FIGURE 3.13: Activation energies of all $CaF_2$ surface slabs with the activation energy of the bulk $CaF_2$ system (green dashed line)

TABLE 3.8: Activation energies calculated from the slopes from Figure 3.12

| **Surface Orientation** | **$E_A$ (kJ/mol)** |
|---|---|
| **(100)** | 84.18 ± 0.05 |
| **(110)** | 102.15 ± 0.48 |
| **(111)** | 142.99 ± 7.58 |
| **(210)** | 102.71 ± 0.67 |
| **(310)** | 109.26 ± 8.36 |
| **(221)** | 133.25 ± 1.01 |
| **Bulk** | 184.73 ± 5.55 |

#### 3.4.2.2 Sectioned Activation Energy

The slices of the surface slabs that exhibited surface effects were classified as those slices that experienced enhanced diffusion, compared to bulk levels. The data from Figure 3.11 was analysed, and the slices that experienced diffusion greater than the bulk levels (outside the standard error) were classified as "surface slices". These slices were grouped and are hence known as the "surface section". The remaining slices of the surface slab, experiencing bulk diffusion levels were classified as the "bulk-like slices", and are grouped to form "bulk-like section". The way in which the surface slab is sectioned is demonstrated in Figure 3.14 and the number of slices used to generate both sections for each surface orientation, are given in Table 3.9.

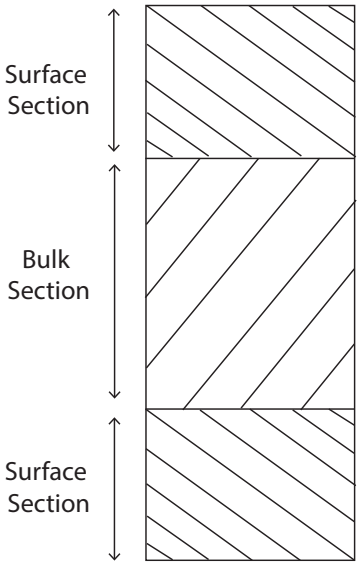


FIGURE 3.14: Schematic of surface slab, sectioned into "surface" and "bulk" regions

TABLE 3.9: Number of slices taken from the top and bottom surface used to generate the "surface section", and the number of slices from the centre of the slab, used to generate the "bulk-like section", for all surface orientations of $CaF_2$

| **Surface Orientation** | **# Surface Slices** | **# Bulk Slices** |
|---|---|---|
| **(100)** | 4 × 2 | 6 |
| **(110)** | 5 × 2 | 10 |
| **(111)** | 3 × 2 | 7 |
| **(210)** | 6 × 2 | 8 |
| **(310)** | 3 × 2 | 7 |
| **(221)** | 5 × 2 | 10 |

The activation energies of the surface and bulk-like sections of each surface slab orientation were calculated separately. The Arrhenius plot for the (310) $CaF_2$ surface is given in Figure 3.15. This plot is representative of the other surface orientations, where the bulk section exhibits a steeper slope than the surface section, signifying a higher activation energy.

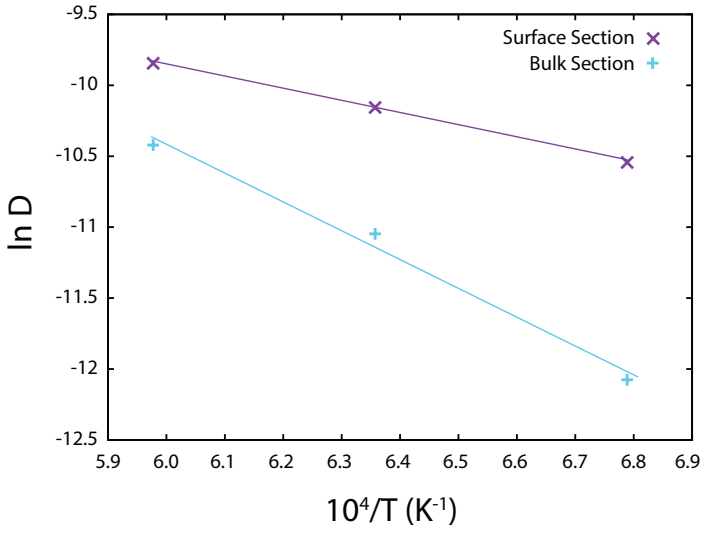


FIGURE 3.15: Arrhenius plot of the diffusion of the (310) $CaF_2$ surface, separated into "surface" and "bulk" sections, at 1473K, 1573K and 1673K. The "bulk" exhibits a steeper slope that that of the "surface" section, indicating a higher activation energy.

The activation energy of the bulk-like sections and surface sections are given numerically in Table 3.10 and are displayed graphically in Figure 3.16. The activation energy of the $CaF_2$ bulk system is provided for comparison. The activation energies calculated from the bulk section of all of the surface slabs were close to that calculated for the bulk $CaF_2$ system (the (100), (111), (210) and (221) surfaces are within the statistical error of the bulk $E_A$), indicating that the bulk section had been correctly identified and isolated.

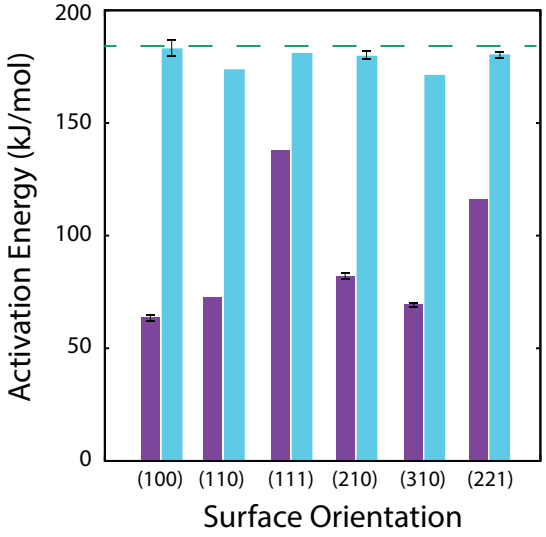


FIGURE 3.16: Activation energies of the surface sections (purple) and bulk sections (blue) of all CaF $_2$ surface slabs compared to the activation energy of the bulk $CaF_2$ system (green dashed line)

TABLE 3.10: Activation energies of the "surface" and "bulk" sections for all surface orientations for temperature range 1473K-1673K using Equation 2.23, compared to bulk $E_A$

| **Surface Orientation** | **Bulk $E_A$ (kJ/mol)** | **Surface $E_A$ (kJ/mol)** |
|---|---|---|
| **(100)** | 181.43 ± 6.20 | 63.63 ± 2.97 |
| **(110)** | 171.51 ± 0.004 | 73.33 ± 0.12 |
| **(111)** | 179.76 ± 0.24 | 128.14 ± 0.09 |
| **(210)** | 177.91 ± 3.40 | 82.26 ± 2.34 |
| **(310)** | 170.11 ± 0.19 | 71.72 ± 0.89 |
| **(221)** | 178.30 ± 2.22 | 111.74 ± 0.52 |
| **Bulk** | 184.73 ± 5.55 | |

Across all surface slab orientations, the surface sections possess lower activation energies than the bulk sections, which is consistent with the higher diffusion coefficients these sections have. Comparing the increases in diffusion coefficient at all surface orientations (from Table 3.7) to the activation energies of the surface sections of the slabs (given in Table 3.10), the relative ordering is found to be the same e.g. the (100) surface exhibits the highest surface diffusion coefficient and the lowest surface activation energy. Also of note is the relative activation energies of the surfaces. Isolating the surface regions results in a more pronounced difference in activation between the different surfaces. This is due to the removal of the effect of the bulk regions, the size of which, differed depending on the slab orientation.

### 3.4.3 Sliced RDFs

The effect the presence of a surface has on the ordering of a crystal system can be displayed by examining the RDFs of the slab as a function of depth from the surface. The surface slab is sectioned, as before for the diffusion depth profile and for the sectioned activation energy calculations. The top and bottom slice of the surface slab are examined, and classified as having a "surface" structure. Both surfaces are investigated to take into account the random nature of the ionic diffusion resulting in non-symmetric surfaces after the MD simulation. The central slice of the slab is also investigated and classified as having a "bulk-like" structure. Figure 3.17 shows the Ca-Ca, F-Ca and F-F RDFs ((a), (b) and (c) respectively) for two (310) surfaces, within the centre of the (310) surface slab, for the surface slab as a whole and for the bulk system, all at 1573K. The behaviour observed here was also seen for 1473K and 1673K.

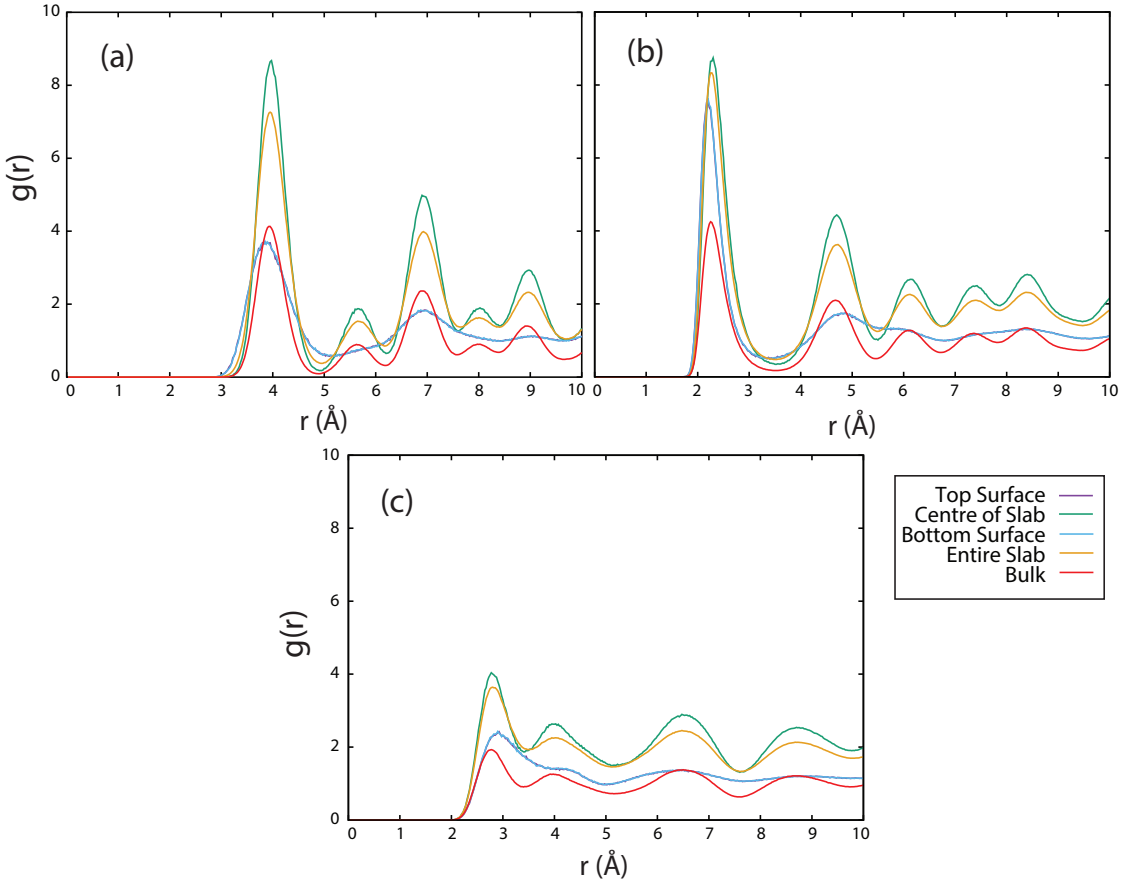


FIGURE 3.17: Partial radial distribution functions, g(r): (a) Ca-Ca, (b) F-Ca and (c) F-F, for the two $CaF_2$ (310) surfaces, the central slice of the (310) slab, for the (310) slab as a whole and for the bulk $CaF_2$ system, all at 1573K.

All three partial RDF plots exhibit a more crystalline structure within the centre of the slab, compared to the surfaces. This is seen by comparing their sharp, defined peaks to the much broader, shorter peaks of the partial RDFs for the surface layers. This loss of structure for the surface layers was found for all surface orientations studied at all temperatures. It should be noted that both surface layers of each surface slab orientation experienced the same degree of atomic vibration and as such have overlapping RDFs. For each of the surface slabs, the surface orientation influenced the extent to which the surface effects propagated. This extent corresponded to the layers that experienced an increased diffusion coefficient, compared to bulk values for the relevant temperature (refer back to Figure 3.11 and Table 3.7). The RDF calculated for the surface slab in its entirety demonstrates the same lattice positions as indicated by the central slice, however it has broader, shorter peaks. This signifies an increase in atomic vibration, which can be attributed to the fact that this RDF is comprised of both surface and bulk-like atomic structures, and the surface effects are introducing disorder into the slab.

### 3.4.4 Strained Surfaces

Straining the bulk system and introducing surfaces have both been separately shown to have an effect on diffusion when compared to an unstrained bulk crystal (both within literature and corroborated by the findings in this work). The effect of strain (both tensile and compressive) on surfaces was investigated to determine the combinatory effects of both surfaces and strain, and investigate the extent, if any, of change to the diffusivity of $CaF_2$ surface slabs. Any change observed was examined to determine whether it correlated with what was observed for strained bulk systems and unstrained surface slabs.

Figure 3.18 shows the effects of tensile and compressive strains on the diffusion profile of the (310) surface at 1473K. Tensile strain can be seen to result in an increase in diffusion coefficient from the unstrained system, with 4% tensile strain showing a substantial enhancement. This correlates with what was seen for strained bulk systems (Figure 3.7). The diffusion coefficients of the bulk regions of the strained surfaces correspond with the diffusion coefficients of the bulk system, with the comparable tensile strain applied.

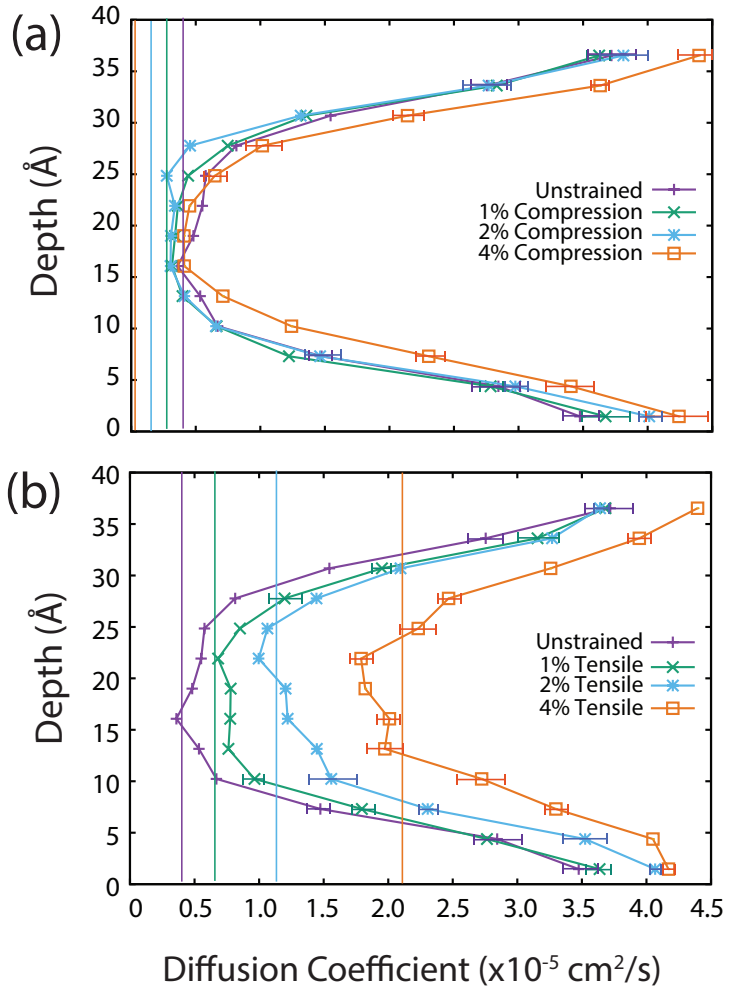


FIGURE 3.18: Depth analysis diffusion profile of $CaF_2$ (310) surface with compressive (a) and tensile (b) strain applied at 1473K. The diffusion coefficient of the bulk system of the corresponding strains (also at 1473K) have been included for comparison

The diffusion of the (310) surface slab demonstrates a weaker response to compressive strain than to the comparable degree of tensile strain. 1% and 2% compressive strains demonstrate a marginally decreased diffusion coefficient within the bulk of the slab, which increases to unstrained values at the surface. The decrease in diffusion coefficient is consistent with the effects observed for compressive strain applied to bulk $CaF_2$. The increase at the surfaces could be a result of the surface effects dictating the behaviour of the ions and its influence overwhelming the effect of strain. When 4% compressive strain is applied to the surface slab, an increase in diffusion coefficient, compared to the unstrained system, is observed. This increase is also present within the bulk regions of the surface slab, resulting in its bulk diffusion coefficients being approximately 4.5 times higher than that predicted by the

bulk system with 4% compressive strain applied. The introduction of strain into the system could be extending the surface effects to deeper depths into the surface slab than previously observed for the unstrained surface slabs, which would account for the higher then expected diffusion coefficients. The increase observed at the surfaces of the slab for 4% compressive strain are approximately the same as those observed for the increase observed for the slab with 4% tensile strain applied.

The diffusion depth profile for all six surfaces for each strain was calculated and compared. The diffusion coefficients at the surfaces of all surface orientations (average of both surfaces in slab) for the strain range 4% tensile to 4% compressive at 1473K are given in Table 3.11 and displayed in Figure 3.19.

TABLE 3.11: Average diffusion coefficient ($\times 10^{-5}$ $cm^2/s$) of top and bottom surface for all $CaF_2$ surface orientations and bulk, for the strain range +4% to -4% at 1473K

| | **(100)** | **(110)** | **(111)** | **(210)** | **(310)** | **(221)** |
|---|---|---|---|---|---|---|
| **+4%** | 4.75 ± 0.10 | 4.16 ± 0.12 | 3.12 ± 0.18 | 4.18 ± 0.23 | 4.28 ± 0.11 | 3.06 ± 0.13 |
| **+2%** | 4.80 ± 0.20 | 3.51 ± 0.01 | 1.95 ± 0.03 | 3.27 ± 0.39 | 3.85 ± 0.21 | 2.71 ± 0.07 |
| **+1%** | 4.52 ± 0.57 | 3.69 ± 0.0001 | 1.58 ± 0.05 | 3.29 ± 0.06 | 3.66 ± 0.02 | 2.26 ± 0.16 |
| **0%** | 5.30 ± 0.37 | 3.54 ± 0.05 | 1.50 ± 0.26 | 3.10 ± 0.09 | 3.60 ± 0.12 | 2.18 ± 0.50 |
| **-1%** | 4.15 ± 0.13 | 3.40 ± 0.18 | 0.90 ± 0.02 | 2.97 ± 0.02 | 3.65 ± 0.03 | 1.55 ± 0.15 |
| **-2%** | 4.39 ± 0.06 | 2.92 ± 0.32 | 0.59 ± 0.001 | 3.33 ± 0.05 | 3.91 ± 0.10 | 1.13 ± 0.09 |
| **-4%** | 4.71 ± 0.18 | 3.59 ± 0.35 | 0.20 ± 0.04 | 4.13 ± 0.17 | 4.32 ± 0.08 | 1.00 ± 0.40 |

The (310) surface diffusion coefficients can be seen to increase with both increasing tensile and compressive strain. Similar behaviour is experienced by the (110) and (210) surfaces. The (100) surface has a much higher diffusion coefficient for the unstrained system than the strained systems. The trend of diffusion coefficients experienced by the (111) and (221) surfaces correlates with the behaviour observed for bulk $CaF_2$, of increasing diffusion coefficient with increasing tensile strain and decreasing diffusion coefficient with increasing compressive strain.

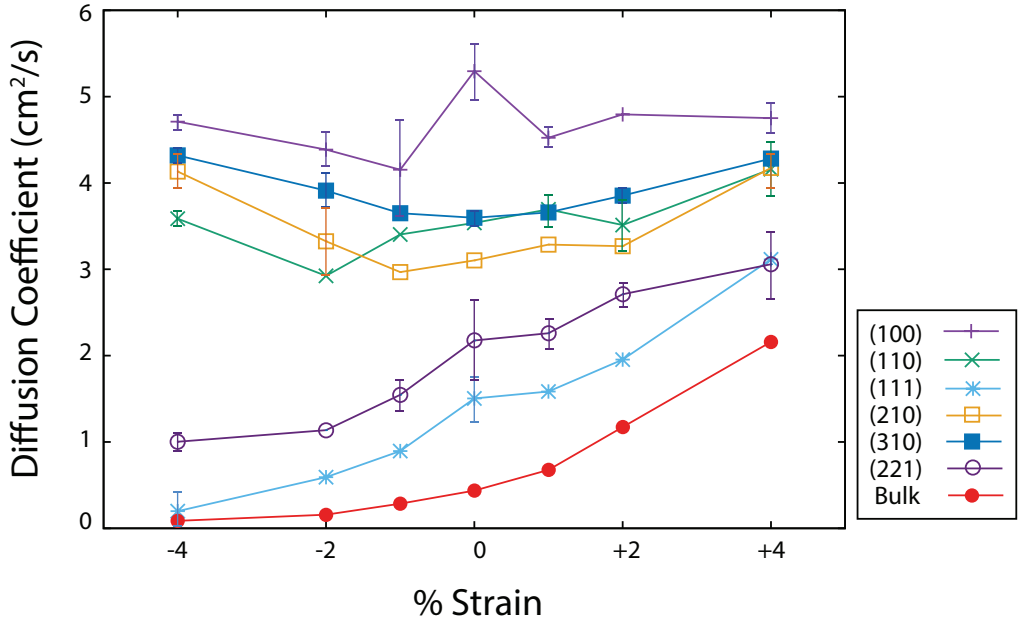


FIGURE 3.19: Average diffusion coefficient of top and bottom surface for all $CaF_2$ surface orientations and bulk, for the strain range +4% to -4% at 1473K, from Table 3.11

For the unstrained (111) surface slab, the surfaces show a definite increase in diffusion coefficient compared to that within the centre of the slab (as demonstrated in Figure 3.20(a)). When 4% compressive strain is applied to this surface slab, it results in a considerable reduction in the increase in diffusion coefficient observed at the surface. This indicates that the effect the presence of a surface has on the diffusion is becoming overwhelmed by the strain effects. This effect is observed for all temperatures studied, with the diffusion enhancement at the surface increasing with temperature as the surface effects become more pronounced.

The (221) surface displays very similar diffusive characteristics to the (111) surface when strain is applied. The diffusion depth profile of the (221) surface with 4% compressive strain exhibits the lowest diffusion coefficient across the entire slab (Figure 3.20(b)). This surface orientation shows an increase at the surfaces, unlike the (111), indicating the surface effects are still having an impact on the diffusion. The (111) surface orientation has been seen to exhibit the lowest surface energy, while the (221) orientation has been found to exhibit the second highest surface energy (from Table 3.5). The greater stability of the (111) surface could explain its tendency to lose its surface effects at high strain, with a reduction of its surface diffusion coefficient to close to bulk levels. The reduced stability of the (221) surface orientation could, in the same manner, explain its surface effects persisting with high strain.

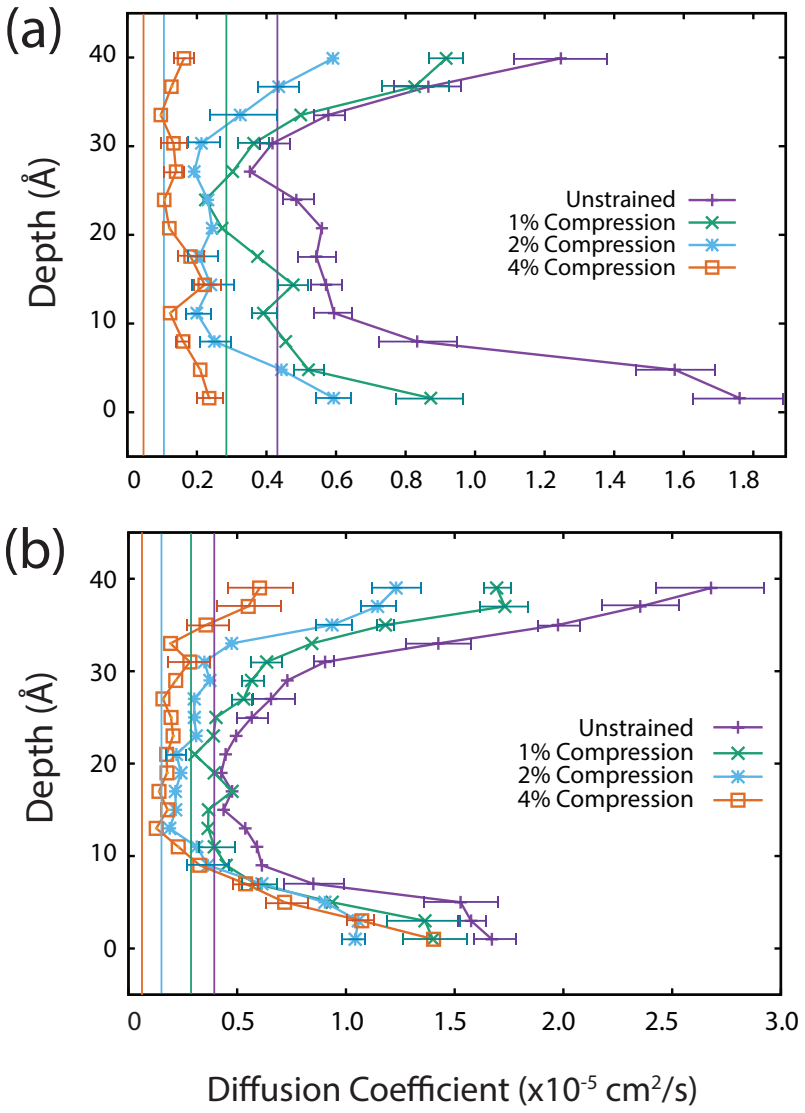


FIGURE 3.20: Depth analysis diffusion profile of $CaF_2$ (a) (111) and (b) (221) surfaces with compressive strain applied at 1473K. The diffusion coefficients of the bulk system of the corresponding strains (also at 1473K) have been included for comparison.

## 3.5 Grain Boundaries

Seven $CaF_2$ low index tilt grain boundaries, the $\Sigma3(111)$, $\Sigma5(210)$, $\Sigma5(310)$, $\Sigma9(221)$, $\Sigma11(332)$, $\Sigma13(320)$ and the $\Sigma13(510)$, were investigated in this study. They have all been previously documented in literature for other fluorite systems, although there remains extremely limited literature data available on $CaF_2$ grain boundaries.

### 3.5.1 Grain Boundary Structures

The potential energy surfaces obtained from METADISE were used to generate the lowest energy grain boundary structure. The PES for the Σ9(221) grain boundary is show in Figure 3.21.

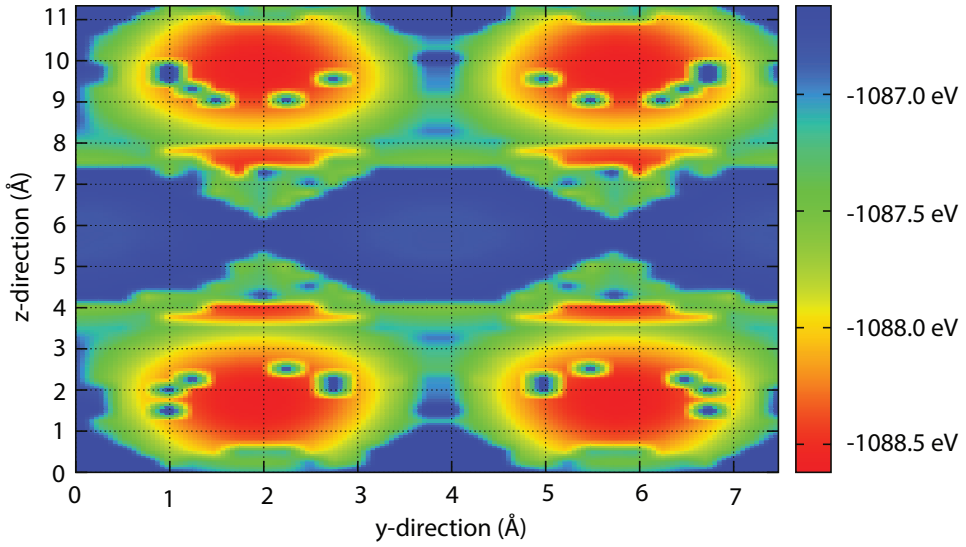


FIGURE 3.21: Potential energy surface of Σ9(221) grain boundary

The structures of the surfaces used for reflection to generate the grain boundaries are shown in Figure 3.22. The (310), (332) and (510) are type I, the (111) type II and the (210), (221) and (320) are type III, according to Tasker [53]. The (111), (221) and (320) surfaces are anion terminated, the (210) is cation terminated and the (332), (310) and (510) surfaces are cation and anion terminated.

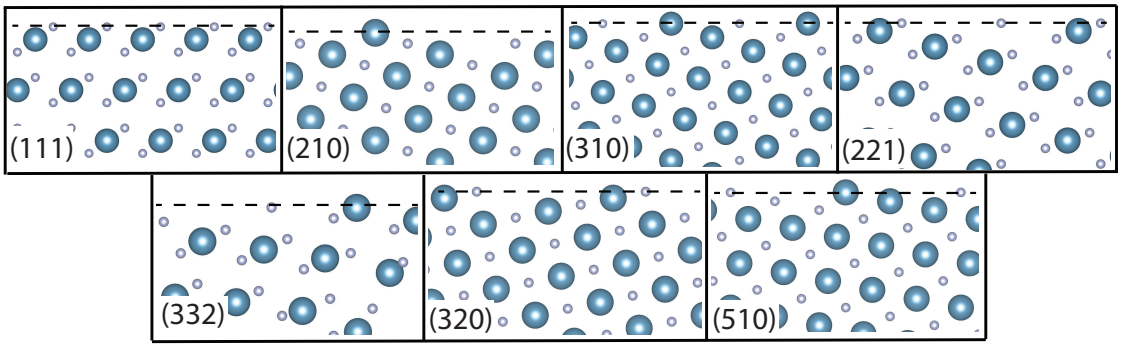


FIGURE 3.22: Atomic structure of surfaces used to generate their respective grain boundary, where the dashed line indicates the surface.

The energy minimised grain boundary structures found by temperature scaling to 573K followed by 300K are given below and are compared to literature structures of other fluorite-structured materials. The $F^-$ ions for all (except for the Σ13(320)) grain boundaries have been removed for clarity.

#### 3.5.1.1 Σ3(111)

The energy minimised Σ3 (111) grain boundary structure found for $CaF_2$ (Figure 3.23), is comparable to other fluorite systems examined both theoretically [64, 147, 148] and experimentally [5, 8]. It is visually the most 'bulk-like' grain boundary that is studied in this work.

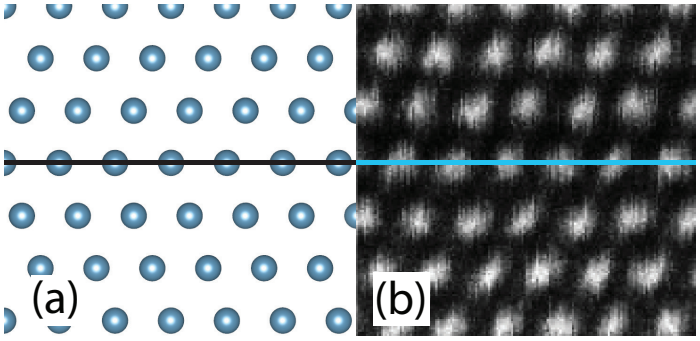


FIGURE 3.23: (a) Average Σ5 (210) $CaF_2$ grain boundary structure over 300K MD run, compared to (b) a HAADF STEM experimental image of $CeO_2$ [5]

#### 3.5.1.2 Σ5(210)

The kite shapes formed by the Σ5(210) $CaF_2$ grain boundary (Figure 3.24) are comparable to those found for fluorite structured systems analysed both theoretically and experimentally [6–8, 149–151].

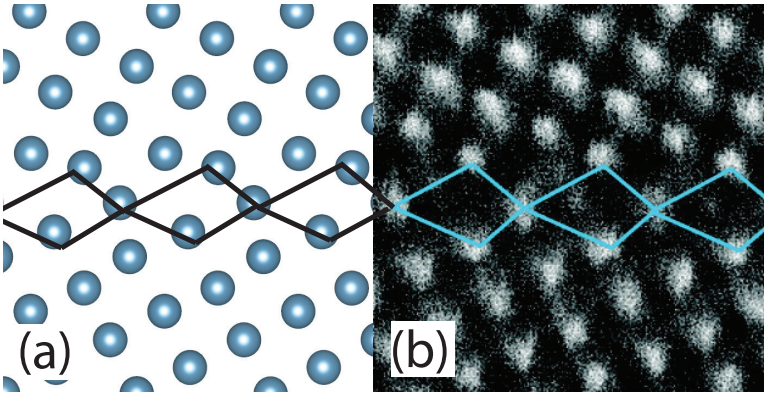


FIGURE 3.24: (a) Average Σ5 (210) $CaF_2$ grain boundary structure over 300K MD run, compared to (b) a HAADF image of a $CeO_2$ Σ5 (210) GB [6]

#### 3.5.1.3 Σ5(310)

Figure 3.25 demonstrates the similarity between the $CaF_2$ structure, and that obtained experimentally using a HAADF-STEM of $CeO_2$ [7]. This connected triangle structure has been observed in other previous studies, in fluorite materials such as YSZ, doped ceria and $UO_2$ [64, 130, 147, 149].

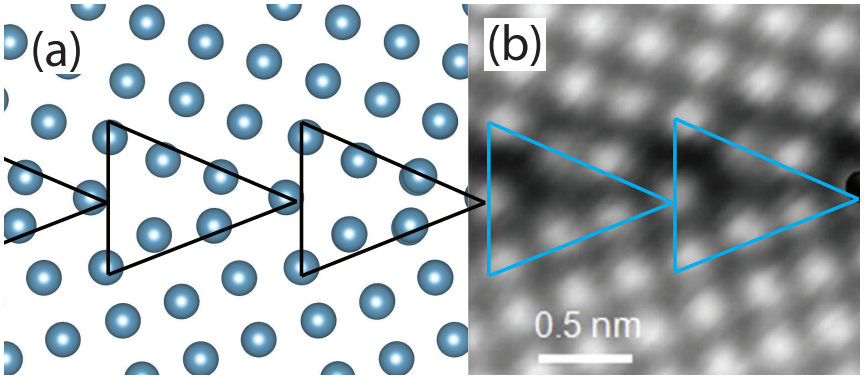


FIGURE 3.25: (a) Average Σ5 (310) $CaF_2$ grain boundary structure over 300K MD run, compared to (b) a statistically averaged STEM-HAADF image of a $CeO_2$ Σ5 (310) GB [7]

#### 3.5.1.4 Σ9(221)

Using the lowest energy point predicted by the shell model in METADISE allowed for the generation of a Σ9(221) grain boundary, whose structure correlates closely with other fluorite systems [64, 149]. Figure 3.26 demonstrates the highly comparable structures of the Σ9(221) $CaF_2$ grain boundary, and that of $CeO_2$, obtained experimentally using a HAADF-STEM [8].

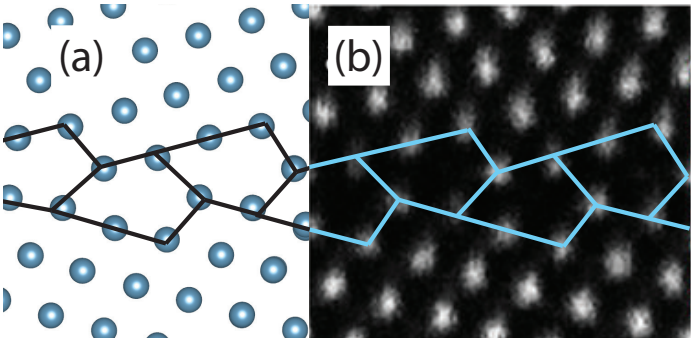


FIGURE 3.26: (a) the average Σ9 (221) grain boundary structure over 300K MD run, compared to (b) a HAADF STEM experimental image of $CeO_2$ [8]

#### 3.5.1.5 Σ11 (332)

This grain boundary has not been studied to the same extent as previous boundaries. The only clear demonstration of its structure, that this author could locate, is given by Feng et al. for $CeO_2$[8]. The Σ11 (332) grain boundary structure generated here is given in Figure 3.27, showing repeating "big - small" open areas. This structure does not correspond to that of Feng.

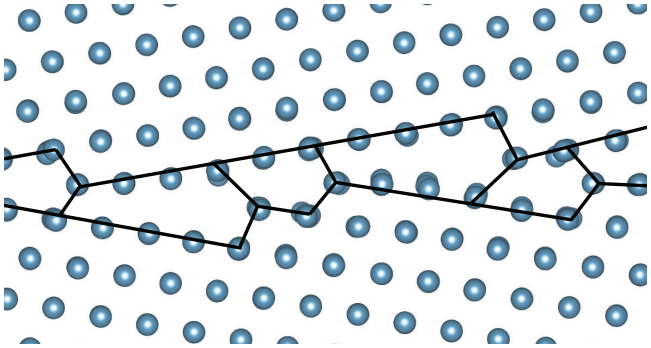

FIGURE 3.27: Average $CaF_2$ Σ11(332) grain boundary structure over 300K MD simulation

This structure underwent further investigation to determine whether the Feng structure could be simulated. The structure was heated to a high temperature (1473K) for 25ps to provide energy for rearrangement of the atomic structure. This high temperature structure was then run at 573K and 300K as before and the resulting grain boundary structure is given in Figure 3.28. This structure, with repeating open areas of the same size, however, has a higher energy than that of the "big - small" structure. There is discrepancy within literature as to the exact structure of some highly studied grain boundaries and due to this boundary being largely neglected it is possible that further studies may find structures contrasting with that of Feng.

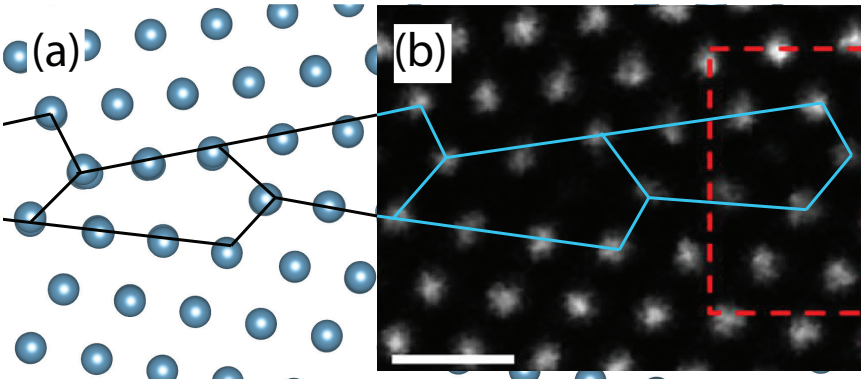


FIGURE 3.28: (a) average $CaF_2$ $\Sigma 11(332)$ grain boundary structure over 300K MD simulation (after inital high temperature scaling) compared to (b) HAADF STEM image of $CeO_2$ GB [8]

#### 3.5.1.6 Σ13 (320)

There have been limited studies carried out on the Σ13 (320) fluorite structured grain boundary. However, it was found that the Σ13 (320) $CaF_2$ grain boundary had a similar structure to the experimentally obtained structure of $CeO_2$ [7] (see Figure 3.29) and the computationally determined structure of YSZ [130].

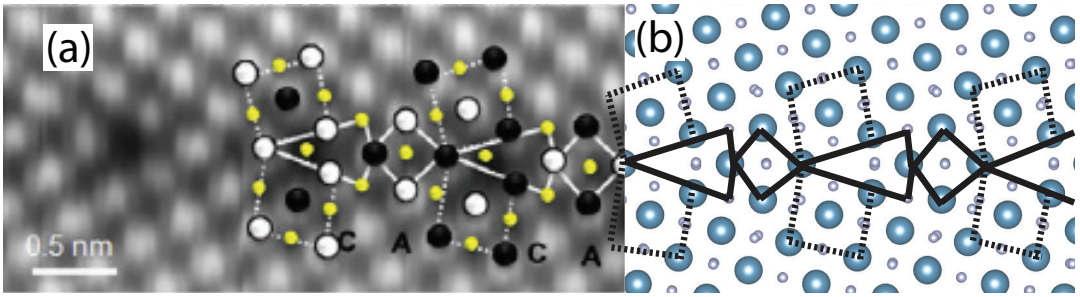


FIGURE 3.29: (a) Statistically averaged HAADF STEM image of Σ13 (320) ceria, overlaid with identified structural units [7] (black - Ce at Z=0, white - Ce at Z=0.5 and yellow - O), compared to (b) average $CaF_2$ grain boundary structure over 300K MD simulation

#### 3.5.1.7 Σ13 (510)

The Σ13 (510) fluorite grain boundary has been more intensively studied then the Σ13 (320). Its structure has been observed experimentally and computationally in YSZ [8, 9, 11, 149] and $CeO_2$ [7, 8]. In Figure 3.30 the $CaF_2$ Σ13 (510) grain boundary is compared to that of an experimentally obtained Σ13 (510) boundary of YSZ [9].

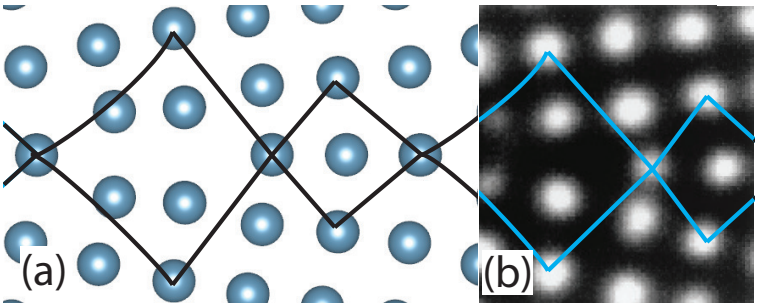


FIGURE 3.30: (a) Average Σ13 (510) $CaF_2$ grain boundary structure over 300K MD run, compared to (b) Σ13 (510) YSZ grain boundary obtained from experiment [9]

### 3.5.2 Grain Boundary Stability

The grain boundary energies were calculated for each grain boundary orientation using Equation 1.12, which can be written as:

$$\sigma_{GB} = \frac{\mathrm{E}_{slab} - \mathrm{nE}_{bulk}}{2\mathrm{A}} \tag{3.3}$$

where $\mathrm{E}_{slab}$ is the total energy of the supercell slab containing the grain-boundary, n is the number of formula units in the supercell, $\mathrm{E}_{bulk}$ is the bulk energy per formula unit, A is the area of the grain-boundary plane within the supercell and 2 is the number of identical grain boundaries present in the supercell. The grain boundary energies are shown in Table 3.12, and can be used to determine the relative stability of the grain boundaries studied.

TABLE 3.12: Grain boundary energies, $\sigma_{GB}$, calculated for various $CaF_2$ boundary orientations (in $Jm^{-2}$), listed according to their order of stability

| **Grain Boundary** | **This Work** |
|---|---|
| Σ3(111) | 0.065 |
| Σ9(221) | 0.132 |
| Σ5(210) | 0.140 |
| Σ5(310) | 0.153 |
| Σ13(510) | 0.154 |
| Σ13(320) | 0.165 |
| Σ11(332) | 0.172 |

All of the grain boundary energies are lower than the surface energies for the corresponding orientation, signifying that the grain boundary structure is more stable. This is due to the fact that, although their coordination number may be different to atoms within the bulk of the material, unlike surface atoms, the atoms that make up the grain boundary structure have atoms surrounding them in all three directions.

As for the corresponding surface energies, the Σ3(111) grain boundary is found to possess the most stable orientation, as would be expected due to it exhibiting the most 'bulk-like' structure (as demonstrated in Figure 3.23). Overall, the grain boundary surface energies increase with increasing density of coincident sites. The Σ9(221) and Σ11(332) grain boundaries, however, are an exception to this trend, indicating that the Σ value, while useful, is insufficient to determine the order of stability, as discussed by Wolf [152].

Van Brutzel and Vincent-Aublant [65] carried out a computational study on six $UO_2$ grain boundaries, the Σ5(310), Σ13(510), Σ17(530), Σ25(710), Σ29(730) and Σ41(910), and found an increase in grain boundary energy with misorientation angle. The Σ5(310) grain boundary was shown to demonstrate a significantly lower energy than the other boundary orientations, postulated to be as a result of it possessing the most favourable GB orientation out of those studied. Williams et al. [64] also calculated $UO_2$ grain boundary energies and found the order of stability to be Σ3(111) > Σ9(221) > Σ5(310) > Σ5(210). This order of stability is consisted with the order of stability they found for the corresponding $UO_2$ surfaces i.e. (111) > (221) > (310) > (210). Their grain boundary order of stability disagrees with that determined in this study, however their results show no obvious trend between stability and misorientation angle as was found here.

The coordination number of the surfaces used to generate the grain boundaries was investigated to determine whether a correlation could be made with the coordination number and grain boundary energy. The coordination number of the surface cations used for the GB construction (shown in Figure 3.22) was found to correlate somewhat with the grain boundary energies. Generally, the higher coordination numbers correspond to lower grain boundary energies. As all of the surafce cations do not have the same coordination number, the coordination number alone is insufficient to fully describe the relative stabilities of the grain boundaries.

TABLE 3.13: The coordination number of the surface $Ca^{2+}$ ions from the surfaces used to generate the GBs (Figure 3.22), listed according to the order of stability determined from the grain boundary energies calculated in this study.

| **Grain Boundary** | **Coordination Number** |
|---|---|
| Σ3(111) | 7 |
| Σ9(221) | 6, 7, 8 |
| Σ5(210) | 4, 6, 8 |
| Σ5(310) | 4, 6, 8 |
| Σ13(510) | 4, 6, 8 |
| Σ13(320) | 4, 6 |
| Σ11(332) | 3, 4, 5, 6 |

### 3.5.3 Depth Analysis of Diffusion

The diffusion of all of the grain boundary slabs was investigated as a function of depth, as was done for the surface slabs, and all of the grain boundary depth profiles were found to exhibit similar behaviour. The Σ5(310) depth profile at 1473K is presented here in detail. Figure 3.31 demonstrates a definite increase in diffusion coefficient at both grain boundaries that are present within the slab, with a reduction of diffusion coefficient within the bulk-like sections of the slab, down to near-bulk levels. The increase observed at the grain boundaries is similar, both to one another and to the increase in diffusion observed for the (310) $CaF_2$ surface (Figure 3.10).

The average structure over the 1473K simulation clearly displays an increase in disorder in the anion sublattice at the grain boundaries. The bulk-like sections of the grain boundary slab retain a more rigid structure, corresponding to the lower diffusion coefficients found for this region. The average structure of the cation sublattice does not demonstrate any enhanced disorder at the boundaries.

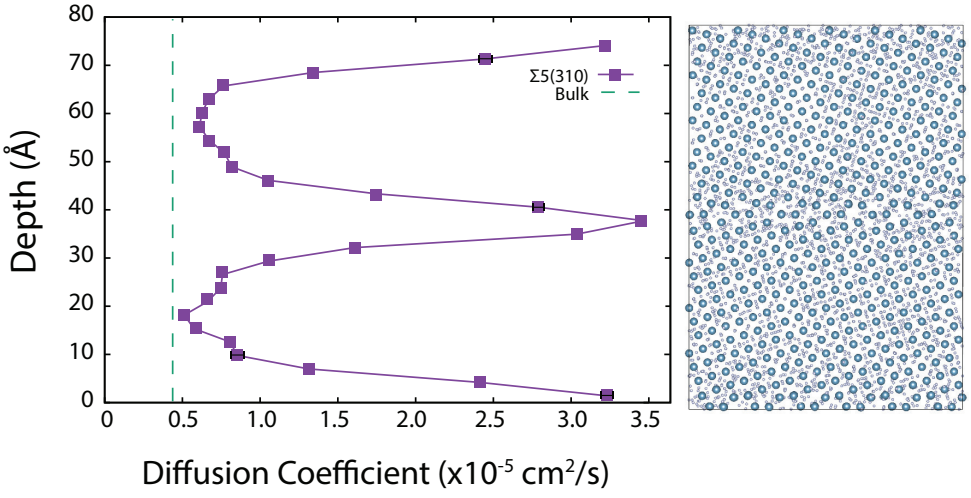


FIGURE 3.31: Depth analysis diffusion profile average $Ca^{2+}$ positions of the Σ5(310) grain boundary, at 1473K

This analysis was carried out on all of the remaining grain boundaries. Figure 3.32 compares the diffusion depth profiles of all of the boundaries at 1473K, 1573K and 1673K. For all temperatures, all structures exhibit a definite increase in diffusion coefficient at their boundaries. This increase ranges from ∼5× to 9× that of the bulk at 1473K, ∼2× to 4× at 1573K, and ∼2× to 3× at 1673K, with a return to bulk values within the centre of the slabs.

Table 3.14 shows the diffusion coefficient, calculated along each of the grain boundaries, for all boundary orientations. These values are the averages of the increases observed for both grain boundaries present in each slab, which are taken to account for the non-symmetric nature of the diffusion at the boundaries. Unlike the surface diffusion depth profile, the relative increase in diffusion coefficient for all the grain boundaries is not consistent across all temperatures studied.

TABLE 3.14: Average diffusion coefficient ($\times 10^{-5}$ cm$^2$/s) of both grain boundaries within each slab orientation at 1473K, 1573K and 1673K

| | **1473K** | **1573K** | **1673K** |
|---|---|---|---|
| **Σ3(111)** | 3.452 ± 0.950 | 4.814 ± 0.367 | 5.297 ± 0.505 |
| **Σ5(210)** | 2.852 ± 0.411 | 3.753 ± 0.497 | 5.129 ± 0.186 |
| **Σ5(310)** | 3.267 ± 0.164 | 4.384 ± 0.038 | 5.423 ± 0.455 |
| **Σ9(221)** | 3.344 ± 0.057 | 4.073 ± 0.194 | 5.625 ± 0.433 |
| **Σ11(332)** | 3.438 ± 0.075 | 4.494 ± 0.076 | 5.455 ± 0.173 |
| **Σ13(510)** | 3.241 ± 0.155 | 4.081 ± 0.075 | 5.271 ± 0.249 |
| **Σ13(320)** | 2.776 ± 0.180 | 3.772 ± 0.406 | 5.040 ± 0.287 |

At 1473K and 1573K, the Σ3(111) grain boundary demonstrated the greatest increase in diffusion coefficient at its boundaries, compared to the other grain boundaries studied. This was unexpected as, like the (111) surface, the Σ3(111) boundary orientation possessed the lowest grain boundary energy (from Table 3.12), and the (111) surface demonstrated the smallest increase in diffusion coefficient at its surface, compared to all the other surface orientations. Similar behaviour was therefore expected for the corresponding grain boundary as for the surface. The grain boundary that exhibits the smallest increase in diffusion coefficient at 1473K is the Σ11(320), which was determined to have the second highest (and therefore expected to be the second least stable) grain boundary energy of those studied. Based on its energy, this boundary structure would be expected to exhibit a large increase in diffusion coefficient.

As the temperature increases, the increase in diffusion coefficient of the Σ3(111) grain boundary, relative to the other boundaries, decreases. The Σ9(221) grain boundary becomes the orientation that produces the greatest increase in diffusion coefficient. This boundary was determined to have the second lowest grain boundary energy. The third and fourth lowest energy grain boundaries, the Σ5(210) and the Σ5(310) respectively, demonstrate contrasting

characteristics. The Σ5(210) has the smallest increase and the Σ5(310) has the second largest increase in diffusion coefficient at their boundaries. The grain boundary energies are therefore insufficient in determining the relative increase in diffusion coefficient, and temperature effects have been shown to have a significant impact on their relative diffusivities.

#### 3.5.3.1 Sectioned Activation Energy

The activation energy of the grain boundaries within the slab were calculated separately from that of the bulk-like regions using the same method as for the surfaces. The "grain boundary regions" were classified as being comprised of slices that experienced diffusion greater than (and outside statistical error from) the bulk levels (from Figure 3.32). The remaining slices were grouped and classified as being "bulk-like regions". A schematic of how the grain boundary slabs were partitioned is given in Figure 3.33. The number of slices used to generate the boundary and bulk sections for each slab orientation are given in Table 3.16.

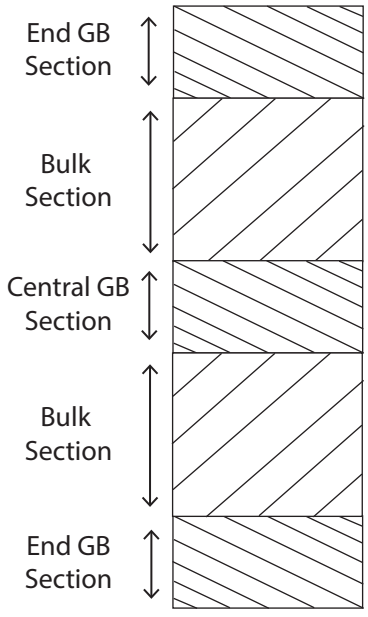


FIGURE 3.33: Schematic of grain boundary slab, sectioned into 2 "bulk" and 3 "grain boundary" (GB) regions. The GB regions can be further classified as either "end" or "central" GB regions.

TABLE 3.15: Number of slices used to generate the "grain boundary" section and the "bulk-like" section, for all grain boundary orientations of $CaF_2$

| **GB Orientation** | **End GB** | **Central GB** | **Bulk** |
|---|---|---|---|
| **Σ3(111)** | 3 × 2 | 6 | 6 × 2 |
| **Σ5(210)** | 4 × 2 | 7 | 6 × 2 |
| **Σ5(310)** | 4 × 2 | 5 | 7 × 2 |
| **Σ9(221)** | 3 × 2 | 7 | 7 × 2 |
| **Σ11(332)** | 5 × 2 | 7 | 5 × 2 |
| **Σ13(510)** | 4 × 2 | 7 | 6 × 2 |
| **Σ13(320)** | 4 × 2 | 7 | 6 × 2 |

The activation energies of the grain boundary and bulk-like sections of each orientation were calculated separately. The Arrhenius plot for the Σ5(310) $CaF_2$ grain boundary is given in Figure 3.34. This plot is representative of the other boundary orientations, where the bulk section exhibits a steeper slope than the grain boundary section, signifying a higher activation energy.

The activation energies calculated for each of both the grain boundary and bulk sections for all the grain boundary orientations are given in Table 3.16. The activation energy for the bulk system is also given for comparison. The "bulk" sections of all the grain boundaries, bar the Σ3(111), can be seen to possess an activation energy that is significantly lower than that of the bulk system, as demonstrated in Figure 3.35. This difference is much larger here than that calculated for the bulk-like sections of the $CaF_2$ surfaces (Figure 3.16). The diffusion coefficients of the bulk-section of the grain boundaries slabs are slightly increased from the true bulk value, as seen in Figure 3.32, which could be as a result of the grain boundary effects permeating within the "bulk" regions. This could account for this decreased activation energy.

The Σ3(111) grain boundary possesses the lowest grain boundary energy (values given in Table 3.12) and the most bulk-like structure, which could account for its bulk regions exhibiting the activation energy closest to that of the bulk system. Conversely, the Σ11(332) was found to posses the highest grain boundary energy. This boundary orientation exhibits the second lowest activation energy for its bulk regions, in a trend consistent with that set by the Σ3(111) boundary. Contradicting this trend is the Σ5(210), which has the lowest bulk activation energy value, yet it has the third highest grain boundary energy. There are, evidently, additional factors playing a part influencing the activation energy of the bulk-like sections of the grain boundary slabs, other than the grain boundary energy.

TABLE 3.16: Activation energies of the "grain boundary" (GB) and "bulk" sections for all boundary orientations for temperature range 1473K-1673K using Equation 2.23, compared to bulk $E_A$

| **GB Orientation** | **Bulk $E_A$ (kJ/mol)** | **GB $E_A$ (kJ/mol)** |
|---|---|---|
| **Σ3(111)** | 182.573 ± 1.916 | 72.586 ± 5.180 |
| **Σ5(210)** | 139.963 ± 1.080 | 75.943 ± 1.233 |
| **Σ5(310)** | 168.487 ± 4.865 | 73.609 ± 2.085 |
| **Σ9(221)** | 148.986 ± 2.843 | 79.791 ± 2.411 |
| **Σ11(332)** | 147.948 ± 6.906 | 67.213 ± 6.910 |
| **Σ13(320)** | 163.161 ± 6.870 | 72.414 ± 7.193 |
| **Σ13(510)** | 152.399 ± 4.676 | 69.631 ± 8.939 |
| **Bulk** | 184.73 ± 5.55 | |

### 3.5.4 Sliced RDFs

The partial RDFs of the grain boundaries were examined as a function of depth in order to examine the degree of atomic structure within the boundary compared to within the bulk sections of the slab. The analysis method is detailed for the Σ5(310) grain boundary, due to its behaviour being representative of the other grain boundary orientations studied. Its diffusion depth profile was examined to identify slices that were representative of either a grain boundary position (indicated by high diffusion coefficient) or a bulk-like region (indicated by its bulk-like diffusion coefficient). The slices selected to have their partial RDFs investigated are indicated in Figure 3.36.

Figure 3.37 shows the Ca-Ca, F-Ca and F-F partial RDFs ((a), (b) and (c) respectively) for the Σ5(310) grain boundary for the slices selected, compared to those of the bulk sections of the slab and also for the bulk system, all obtained at 1573K. Similar behaviour is also seen for the grain boundary at 1473K and 1673K. All three of the partial RDFs demonstrate higher, sharper peaks for the bulk regions of the slab compared to the shorter, broader peaks of the grain boundary regions. The bulk region peaks also persist to greater interatomic distances. This indicates that the bulk regions have a higher crystal ordering. Similar results were found for the (310) $CaF_2$ surface, however the relative change between the bulk and surface/grain boundary regions is greater for the (310) surface, indicating that the Σ5(310) grain boundary possesses a more structured, bulk-like configuration than its comparable surface.

## 3.6 Summary

The bulk results section (Section 3.3) demonstrated the ability of the method and potential used to reproduce experimental results, such as thermal expansion coefficients, diffusion coefficients, ionic conductivities and activation energies. The data obtained from the bulk simulations was then used to compare with other, more complex, systems investigated, such as strained bulk, surfaces and grain boundaries.

Section 3.3.5 investigated the effect that strain had on the diffusivity and structure of the bulk system. The effect of compressive strain was investigated, and generally resulted in a decrease in diffusion coefficient for increasing strain, as predicted by previous literature studies on other fluorite structured materials. However, there was a discrepancy observed for 4% compressive strain at 1673K, where its diffusion coefficient was higher than expected by the previous trend set out. A decrease in $F^-$ disorder from the unstrained system, observed both by examining the average structure of the system over the simulation and through the sharp peaks of the partial RDFs, was consistent with the decrease in diffusion coefficient found, compared to the unstrained system.

Across all temperatures investigated, the diffusion coefficient of the system was found to increase with increasing tensile strain, consistent with the findings reported in literature. This increase could be visually observed by the increased $F^-$ disorder averaged over the simulation, when compared to the unstrained system. The partial RDFs of the bulk $CaF_2$ systems with tensile strain exhibited broader, shorter peaks than its unstrained counterpart, consistent with the system expanding and its disorder increasing. The increase in diffusion as a result of strain is equivalent to that observed with a 150K increase in temperature. The introduction of strain into a system has, therefore, been proposed as a possible mechanism by which the operating temperature of diffusion based devices could be lowered.

In the surfaces results section (Section 3.4), the effect of six surfaces, the (100), (110), (111), (210), (310) and (221), was investigated. The relative surface stability was determined in Section 3.4.1 and found to be (111) > (110) > (210) > (100) > (221) > (310), agreeing with literature findings of other fluorite structured materials. This highlighted the ability of the method and potential used to accurately model, and simulate the atomic movement within, $CaF_2$ surfaces. The effect of surfaces on the diffusivity of the system was examined in Section 3.4.2. There was found to be an increase in the diffusion coefficient at the surfaces, with

a return to bulk-like values within the centre of the slab, for all surface orientations. The activation energies of the surface slabs, both as a whole and sectioned to isolate the regions experiencing surface effects, were studied in Sections 3.4.2.1 and 3.4.2.2. The "surface" region activation energies for all orientations were consistently found to be lower than that of the "bulk" region, in accordance with the increased diffusion coefficients at the surfaces. The partial RDFs from both the surface and from within the centre of a surface slab were compared. The surface RDFs were found to be shorter and broader than those of the bulk, consistent with the increased disorder and diffusivity in the region.

The combinatory effect of surfaces and strain was investigated by straining all the surface orientations and comparing the change in diffusivity with both unstrained surfaces and with strained bulk. Overall, increasing tensile strain was found to result in an increase in diffusion coefficient, both within the bulk of the slab and at the surfaces. Only the (111) and (221) surface orientations were found to follow the trend of consistently decreasing diffusivity with increasing compressive strain, as found for the bulk system.

Seven grain boundary structures (the $\Sigma3(111)$, $\Sigma5(210)$, $\Sigma5(310)$, $\Sigma9(221)$, $\Sigma11(332)$, $\Sigma13(320)$ and the $\Sigma13(510)$) were generated and examined in the grain boundaries results section (Section 3.5) and their relative stability was determined by calculating the grain boundary energies for all orientations. The structures and stability were found to be comparable with those from other fluorite structured systems. Section 3.5.3 investigated the diffusion of the grain boundaries as a function of depth, and the diffusivity was seen to increase at the boundary for all orientations, at all temperatures studied. However, the relative increase at the boundaries, unlike for the surfaces, was not consistent across the temperature range. The activation energy of the grain boundary regions was calculated separately from the bulk-like regions of the grain boundary slabs and found to be lower than that of the bulk regions, as was found for the surface slabs. The structure of the grain boundary slabs was also investigated as a function of depth, and the partial RDFs obtained from the boundary were more disordered than the bulk. However, the peaks of the grain boundary demonstrated more structure than those of the corresponding surface, consistent with the grain boundary energies that indicated the boundaries were more stable than the surfaces.

The information gained from this study of $CaF_2$ can be applied to other fluorite structured systems, such as yttria-stabilised zirconia, which will be under investigation in Chapter 4.

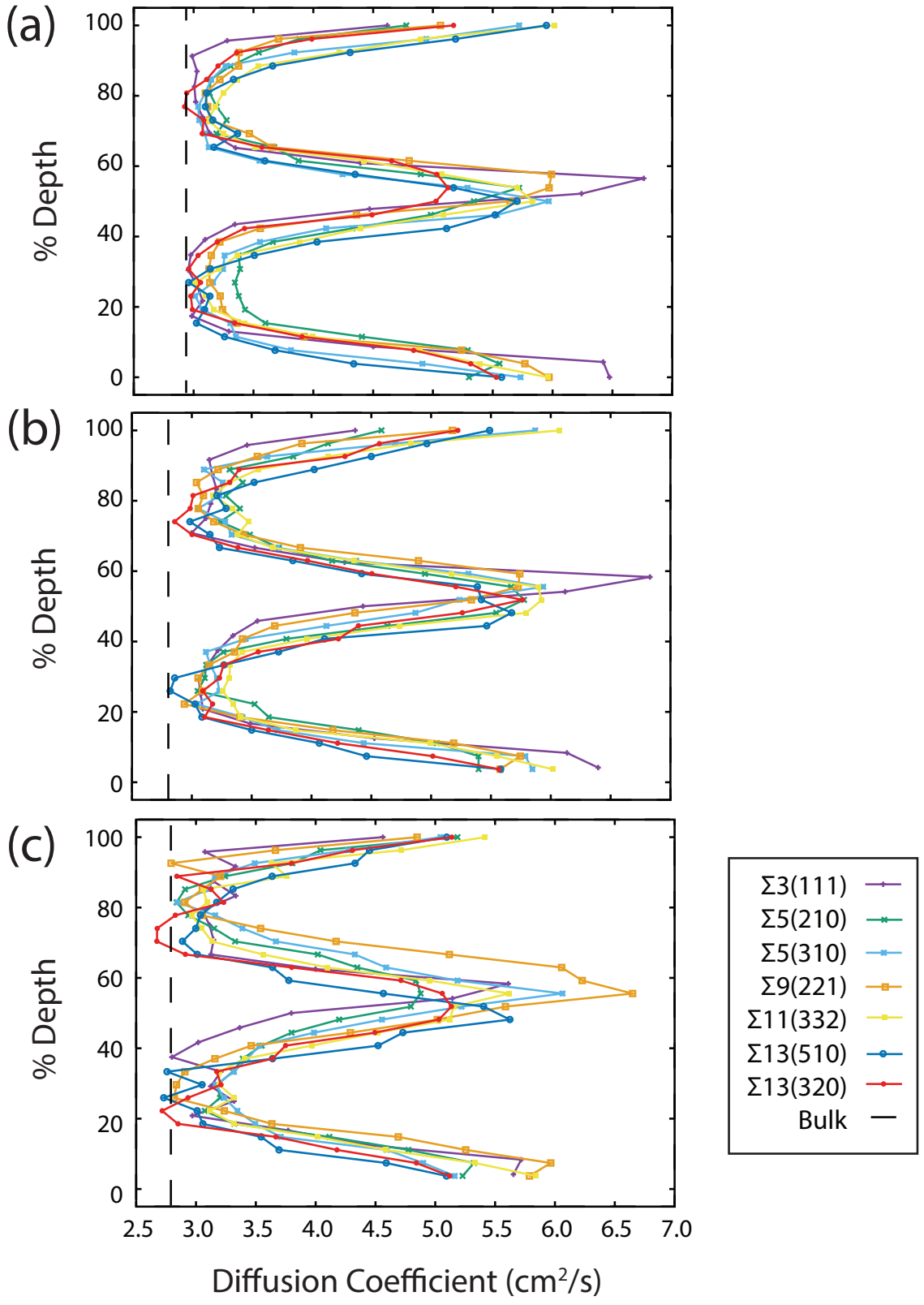


FIGURE 3.32: Comparison of depth analysis diffusion profiles for different grain boundary orientations at (a) 1473K, (b) 1573K and (c) 1673K

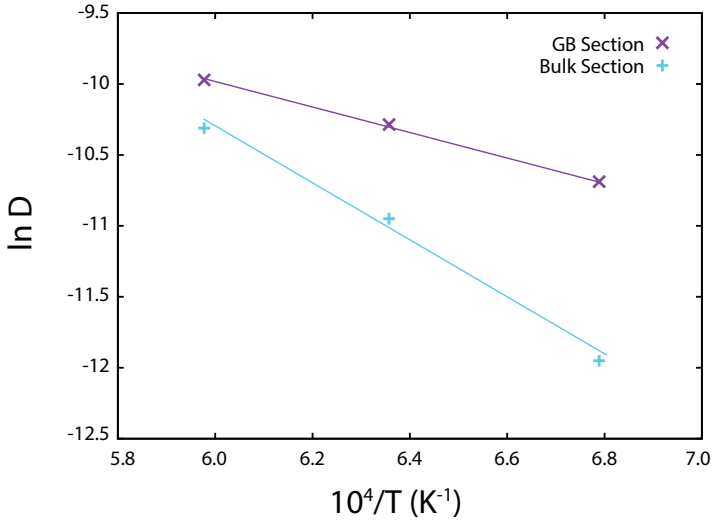


FIGURE 3.34: Arrhenius plot of the diffusion of the (310) $CaF_2$ grain boundary, separated into "grain boundary" and "bulk" sections, at 1473K, 1573K and 1673K

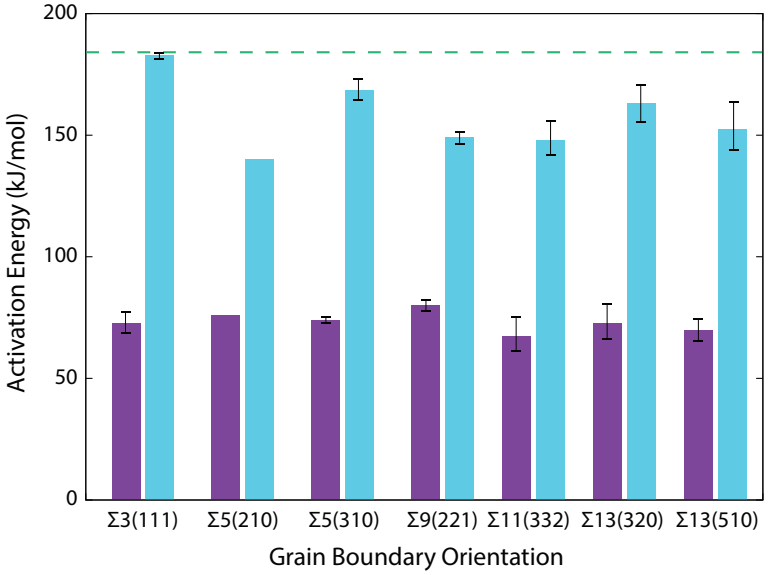


FIGURE 3.35: Activation energies of the grain boundary sections (purple) and bulk sections (blue) of all $CaF_2$ boundary slabs, compared to the activation energy of the bulk $CaF_2$ system (dashed line)

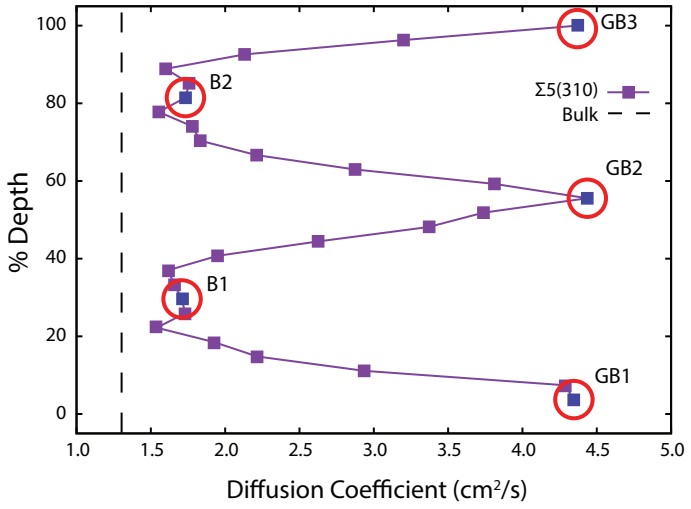


FIGURE 3.36: Positions along the Σ5(310) grain boundary depth profile that were selected to be representative of different sections (either grain boundary - GB, or bulk - B) within the slab at 1573K compared to the bulk diffusion coefficient (dashed line)

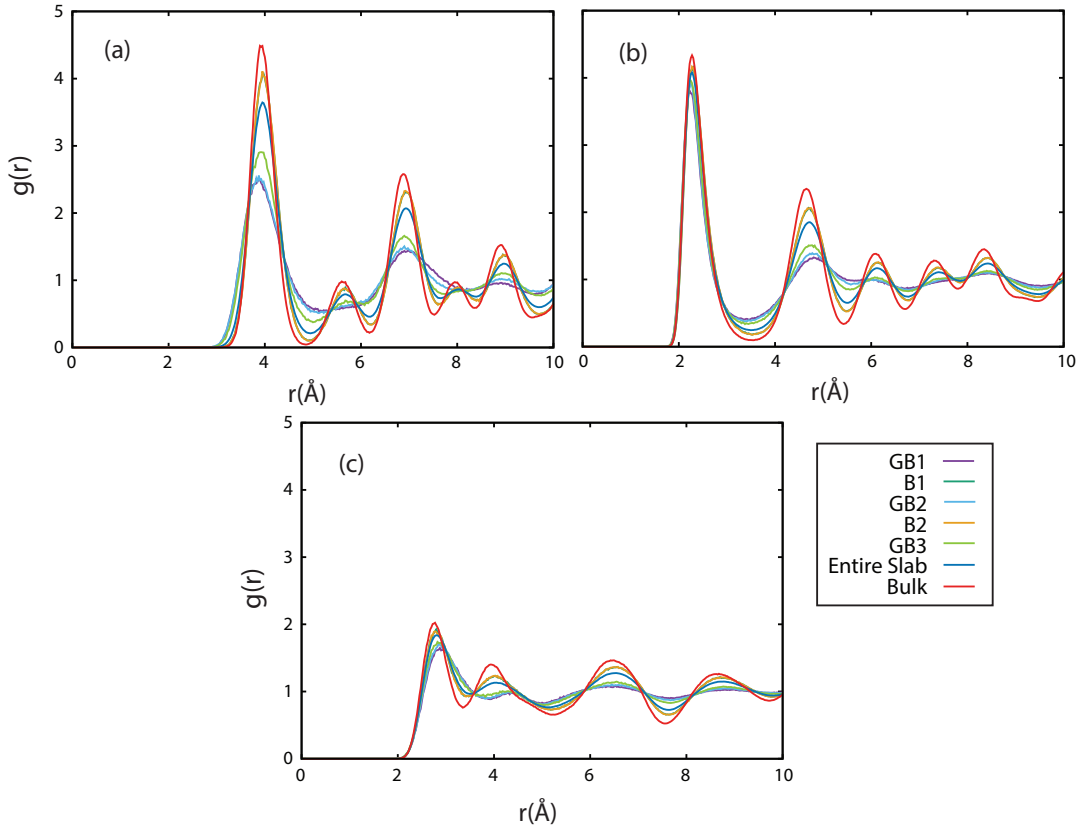


FIGURE 3.37: Transformation of radial distribution function, g(r), with distance from the $CaF_2$ Σ5(310) grain boundary at 1573K: (a) Ca-Ca, (b) F-Ca and (c) F-F, compared with the corresponding partial RDFs for entire grain boundary slab and for the bulk $CaF_2$ system, all at 1573K

# Chapter 4: Yttria-Stabilised Zirconia Analysis

## 4.1 Introduction

$ZrO_2$ exhibits three phases, monoclinic, tetragonal and cubic. At room temperature, under ambient pressure, zirconia's thermodynamic stable phase is monoclinic. This phase transforms into tetragonal upon heating to 1443K and then into the cubic phase at 2643K, which is stable up to the melting point (2953K) [153–155]. These phase changes have large volume changes ($c \rightarrow t \approx 2.3\%$ and $t \rightarrow m \approx 4.5\%$ [156]). Pure zirconia is unsuitable for utilisation in devices, as volume changes of this extent will result in fracturing at the interfaces of components, it therefore requires stabilisation to prevent these volume changes.

One of the ways to achieve stabilisation of the cubic phase is through doping, either with a suitable divalent (e.g. $Ca^{2+}$, $Mg^{2+}$) or trivalent (e.g. $Y^{3+}$, $Sc^{3+}$, $Nd^{3+}$) cation. In these doped system, the dopant cations are located substitutionally on the $Zr^{4+}$ sites and oxygen vacancies are generated to preserve the charge neutrality of the system. It is this vacancy generation that is responsible for the high ionic conductivity of YSZ, as the vacancies facilitate the conduction of the $O^{2-}$ ions through the material and make the material a fast ionic conductor (FIC). The high ionic conductivity, coupled with low electronic conductivity, makes stabilised zirconia a highly attractive material for application within numerous devices, such as solid oxide fuel cells and gas sensors.

Yttria-stabilised zirconia (YSZ) is a commonly used electrolyte in these diffusion based devices, due to its good ionic conductivity over a wide range of oxygen partial pressures and its chemical stability in oxidising and reducing atmospheres [157]. It also benefits from a relatively high melting point ($\approx$ 2973K [158]). In YSZ, a dopant cation, $Y^{3+}$, will replace a zirconium cation, $Zr^{4+}$. As a result of the lower valence state, an oxygen vacancy is generated to preserve charge neutrality. In Kröger-Vink notation this substitution is given by:

$$Y_2O_3 + 2Zr_{Zr}^{\times} + O_O^{\times} \Longleftrightarrow 2Y_{Zr}^{'} + V_O^{\bullet\bullet} + 2ZrO_2 \tag{4.1}$$

The maximum conductivity of a doped-zirconia system has been found to be when the dopant concentration is the minimum required to stabilise the cubic structure [159–161]. There is some debate within literature as to the exact yttria concentration required to achieve this stabilisation, however there is wide-spread agreement, within both theoretical and experimental reports, that it is between 8 and 10 mol% [13, 157, 162–164] ($Y_xZr_{1-x}O_{2-x/2}$, where $x$ = 0.16, 0.20 respectively). This concentration strikes a balance between factors that enhance and hinder the ionic conductivity. An increase in the number of vacancies generated has a beneficial effect on conductivity, due to there being additional sites for the oxygen ions to diffuse into. However, further increase in yttria concentration has been shown to hinder the ionic conductivity.

This conductivity decrease has been postulated to be due to an increase in the association between the oxygen vacancies and $Y^{3+}$ dopant ions [13] and the rate of diffusion of the oxide ions reducing in the vicinity of the dopant ions [14]. It has also been suggested that, as a result of the ionic diffusion within YSZ being associated with atomic defects within the material, interactions between these defects could impact the conductivity the system [165]. The resultant vacancy ordering within the system due to these interaction has been suggested to be determined by vacancy-vacancy > dopant-vacancy >> dopant-dopant interactions. Another study, by Kilo et al. [164], used tracer diffusion experiments and molecular dynamics simulations to study the diffusion with YSZ containing 5-25% yttria. This study found that, for yttria concentrations >10%, the decrease in diffusion coefficient with increasing dopant concentration was as a result of jumps of oxygen vacancies close to the lower valent $Y^{3+}$ cations being less likely than jumps closer to $Zr^{4+}$ cations.

The increase of dopant concentration leads to an increase in interactions between these dopants and the oxygen vacancies they generate. Two yttrium atoms tend to be situated in the nearest neighbour (NN) position to one another and next nearest neighbours (NNN) to oxygen vacancies [166**?** ], whereas the oxygen vacancies prefer the NN position to the zirconium ions. This is consistent with previous experimental [167–169] and computational [166, 170, 171] studies that found the $Y^{3+}$ ions adopt a 8-fold O-coordination, with the

$Zr^{4+}$ O-coordination being reduced from the 8-fold it adopts in $ZrO_2$, to 7-fold in the doped material.

Various surfaces of YSZ have been investigated, both experimentally and computationally [14, 172**?** ] to try understand the effect their presence has on the ionic conductivity within the system. A study by Iskandarov and Umeno used molecular dynamics with an interatomic potential [**?** ] to investigate the investigate the effect of the (110) and (111) surfaces on oxygen diffusion within YSZ [14]. This study found that the (110) surface caused a segregation of vacancies towards the surface and the (111) surface resulted in a migration of vacancies away from the surface to the bulk region. The higher oxygen vacancy concentration of the (110) surface resulted in increased ionic diffusion at the surface, while the (111) surface experienced a decrease in the ionic diffusion in that region. Balducci et al.'s study of the (110) and (111) surfaces of cubic-$ZrO_2$ [173] found that oxygen vacancies tended to segregate toward both these surfaces. There is discrepancy within literature as to the exact effect of different surface orientations on the segregation of oxygen vacancies, and by extension the effect on ionic diffusion within the region. This will be addressed here.

This study will investigate YSZ with 8%, 10% and 12% dopant concentration. These dopant concentrations were selected to be be investigated in this study to determine the dopant concentration that results in maximum conductivity. The same surfaces as examined for $CaF_2$ were generated and studied here for YSZ, so that a comparison between the two fluorite structured materials could be made and the findings compared with literature results of YSZ surfaces. The surface effects on diffusion were considered as a function of depth, as for $CaF_2$, however for YSZ there is an additional element that must be considered, vacancy segregation.

## 4.2 Methodology

A $6 \times 6 \times 6$ supercell of bulk $ZrO_2$, containing 2592 atoms, was initially generated. This pure system was doped with 8%, 10% and 12% yttria, and oxygen atoms were randomly removed to generate charge compensating oxygen vacancies, to preserve the charge neutrality of the system. METADISE was used to cleave six surfaces (the (100), (110), (111), (210), (310) and the (221)) from the pure, undoped bulk $ZrO_2$ supercell, ensuring each surface slab was a minimum of 35Å deep and each had a 40Å vacuum gap inserted (as for $CaF_2$, see Figure 3.1). These surfaces were then doped with 8%, 10% and 12% yttria. The number of each atom type and oxygen vacancies for the bulk and surfaces for 8%, 10% and 12% dopant concentration are given in Table 4.1.

TABLE 4.1: Number of O, Zr and Y atoms and O vacancies for the bulk YSZ system and each of the YSZ surfaces, with 8%, 10% and 12% dopant concentration

| | % | O | Zr | Y | $O_{vac}$ | | % | O | Zr | Y | $O_{vac}$ |
|---|---|---|---|---|---|---|---|---|---|---|---|
| **Bulk** | 8 | 1659 | 726 | 138 | 69 | **(210)** | 8 | 1751 | 766 | 146 | 73 |
| | 10 | 1642 | 692 | 172 | 86 | | 10 | 1733 | 730 | 182 | 91 |
| | 12 | 1624 | 656 | 208 | 104 | | 12 | 1715 | 694 | 218 | 109 |
| **(100)** **(110)** | 8 | 1843 | 806 | 154 | 77 | **(310)** | 8 | 1920 | 840 | 160 | 80 |
| | 10 | 1824 | 768 | 192 | 96 | | 10 | 1900 | 800 | 200 | 100 |
| | 12 | 1805 | 730 | 230 | 115 | | 12 | 1880 | 760 | 240 | 120 |
| **(111)** | 8 | 1936 | 848 | 160 | 80 | **(221)** | 8 | 1728 | 756 | 144 | 72 |
| | 10 | 1915 | 806 | 202 | 101 | | 10 | 1710 | 720 | 180 | 90 |
| | 12 | 1895 | 766 | 242 | 121 | | 12 | 1692 | 684 | 216 | 108 |

The doped bulk systems were run at 973K, 1173K, 1373K and 1573K and the surfaces were run at 1173K, 1373K and 1573K. Three different configurations for each dopant concentration were generated by randomly replacing zirconium with yttrium and removing oxygen atoms to generate oxygen vacancies. Each configuration was run at each temperature (see Figure 4.1, where all "config 1" etc. have the same inital starting configuration), allowing for a comparison to be made between the temperature effects on the system. Averaging results over three runs is done to take into account the statistical nature of MD.

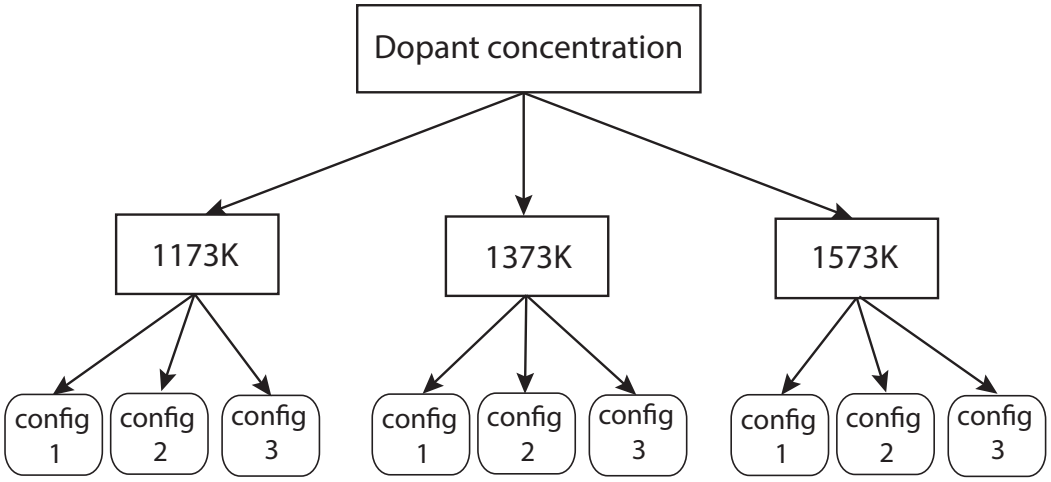


FIGURE 4.1: Schematic of how the YSZ systems were doped. There were three configurations run for each temperature, where the three configurations were consistent across all temperatures to allow for comparison of the temperature effects on the system.

### 4.2.1 Simulation Information

The surfaces were initially all run at 1573K for 20ps to allow the random vacancy positions the time and energy to reposition themselves into an energy favourable position, determined by the surface effects propagating into the slab.

The same method was applied to the bulk systems as to the surface slabs (after the surfaces had completed their initial 20ps 1573K run) and is as follows:

- Each system was temperature scaled to the desired temperature every 0.1ps for 10ps.
- The system was then equilibrated at this temperature for 30ps.
- The production run lasted 3ns for the bulk 973K and 1ns for the remaining systems investigated

All simulations were carried out using a timestep of 4fs and a short range cut-off of 12Å. The bulk simulations were run using the isothermal-isobaric ($NPT$) ensemble and the surface slabs were run using the canonical ($NVT$) ensemble (using volumes scaled by the thermal expansion coefficients calculated from the bulk).

### 4.2.2 Potential Parameters

The potential parameters used for simulations of yttria-stabilised zirconia were derived by Burbano et al. [47] and were obtained from fitting to *ab initio* simulations. The parameters used in this study are shown in Table 4.2.

TABLE 4.2: YSZ Potential parameters used, all given in atomic units. The parameters $b_{O^{2-}-X}$ have the same value as $b_{X-O^{2-}}$ and short-range parameters not given are equal to zero

Repulsive and dispersive parameters

| | $A_{ij}$ | $a_{ij}$ | $B_{ij}$ | $b_{ij}$ | $C_6$ | $C_8$ | $b_6$ | $b_8$ |
|---|---|---|---|---|---|---|---|---|
| O - O | 7.15 | 18.52 | 50000 | 1.00 | 83 | 1240 | 1.30 | 1.70 |
| Y - O | 118.0 | 1.38 | 50000 | 1.50 | 21 | 264 | 1.60 | 2.08 |
| Zr - O | 89.79 | 1.29 | 50000 | 1.75 | 21 | 271 | 1.62 | 2.10 |

Polarisabilities and damping parameters

| | $\alpha$ | $b_{O^{2-}-X}$ | $c_{O^{2-}-X}$ | $c_{X-O^{2-}}$ |
|---|---|---|---|---|
| $O^{2-}$ | 13.97 | 2.18 | 3.03 | - |
| $Y^{3+}$ | 2.31 | 1.47 | 1.08 | -0.60 |
| $Zr^{4+}$ | 2.38 | 1.74 | 1.56 | -0.60 |

## 4.3 Bulk

The physical properties of bulk yttria-stabilised zirconia were investigated and compared with literature to ensure the validity of the potential used and to establish a baseline with which the surface effects could be compared.

### 4.3.1 Thermal Expansion

#### 4.3.1.1 Lattice Constants

The lattice constants of cubic YSZ, doped with 8%, 10% and 12% yttria for the temperature range 973K - 1573K, were determined from the length of one side of the cubic bulk system after the $NPT$ MD simulation. Figure 4.2 shows that the lattice constants compared well with those found in literature [10–12]. The lattice constants are seen to increase with both temperature and yttria concentration. The increased thermal energy input into the system causes greater lattice distortions and a corresponding expansion in the volume of the system. The cause of the increase in lattice constant with yttria concentration can be examined by studying the Zr- O and Y-O partial RDFs.

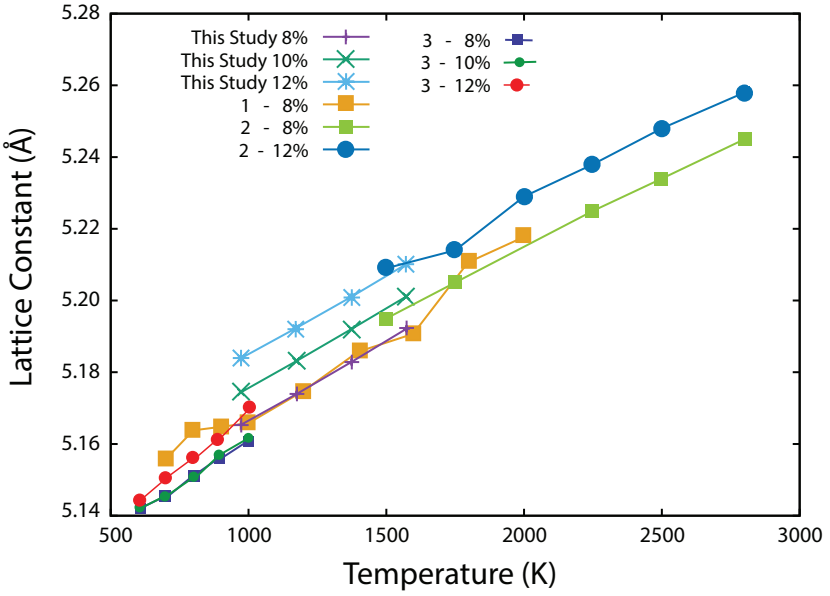


FIGURE 4.2: Lattice constants of YSZ as a function of temperature for 8, 10 and 12% yttria content from this study compared to literature values for 8% and 12% doped YSZ, designated as 1 [10], 2 [11] and 3 [12]

#### 4.3.1.2 Radial Distribution Functions

Figure 4.3 demonstrates the cation - anion and anion - anion partial RDFs for all dopant concentrations investigated at the highest temperature studied, 1573K. All partial RDFs can be seen to maintain long range order, indicating that the crystalline structure is maintained throughout the simulation.

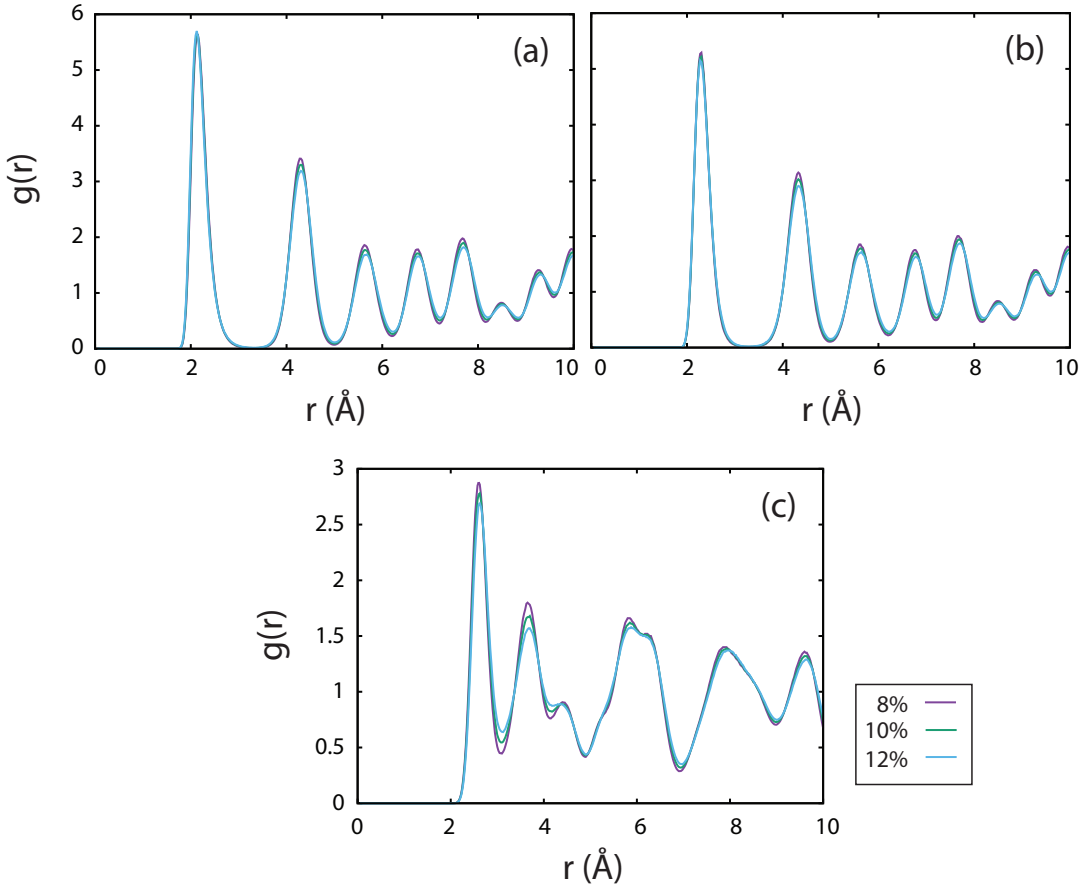


FIGURE 4.3: Zr-O, Y-O and O-O partial RDFs (averaged over 3 configurations) for 8, 10 and 12% YSZ at 1573K

The lattice constant of bulk YSZ was seen to increase with increasing dopant concentration (observed in Figure 4.2). The Zr-O and Y-O partial RDFs for each yttria concentration were examined to determine whether differing anion-cation interactions were the cause of this change in lattice constant. Figures 4.3(a) and (b) shows no discernible difference in the shapes of either the Zr-O or Y-O partial RDFs, respectively, with yttria content. Of particular interest is the interatomic distance of the first peak, which indicates the nearest neighbour distance, remains approximately stationary with varying dopant concentration.

The peak position for the Zr-O and Y-O partial RDFs shift to the right with increasing dopant concentration, indicating longer interatomic distances. The change in peak position, however, is extremely small and therefore not considered to be the cause of the change in lattice constant. The differences in interatomic distances between the $Zr^{4+}$ and $Y^{3+}$ cations to the $O^{2-}$ anions can be used to explain the substantial change in lattice constant. The Zr-O distance was found to be 2.1Å, which was shorter than the Y-O distance of 2.3Å, agreeing with those found within literature [174]. The cause of this change can largely be explained by the difference size of the cations; 0.84 Å for $Zr^{4+}$ and 1.04Å for $Y^{3+}$ [175].

#### 4.3.1.3 Thermal Expansion Coefficients

The thermal expansion of the bulk system was calculated using Equation 3.1. A plot of $\frac{L-L_0}{L_0}$ against temperature for bulk YSZ (shown in Figure 4.4) demonstrates linear behaviour, signifying that the expansion coefficient is constant for each concentration across the temperature range 973K - 1573K. The linear thermal expansion coefficients calculated for each dopant concentration are given in Table 4.3. 8% YSZ has the highest linear expansion coefficient, and 12% the lowest.

This trend was observed in an experimental study by Biswas et al. [12] in which YSZ with 8% - 12% dopant concentration was studied by in situ high temperature X-ray diffraction in the temperature range of 373K - 1273K. Biswas et al. found that the thermal expansion coefficient increased with temperature for all dopant concentrations studied. With increasing dopant concentration, the thermal expansion was found to decrease for a given temperature, and range from 9.65 to 9.03 $\times$ $10^{-6}$ / K for 8-12% YSZ. Other studies, both experimental and computational have also investigated the thermal expansion coefficients of YSZ and are reported to be in the range (6.8 - 10.8) $\times$ $10^{-6}$ / K [157, 174, 176–181]. The agreement with both the trends observed, and the values calculated for the thermal expansion coefficients from this study, with literature. indicate that this model has successfully modelled both the temperature and dopant concentration dependence on the structure and behaviour of bulk YSZ.

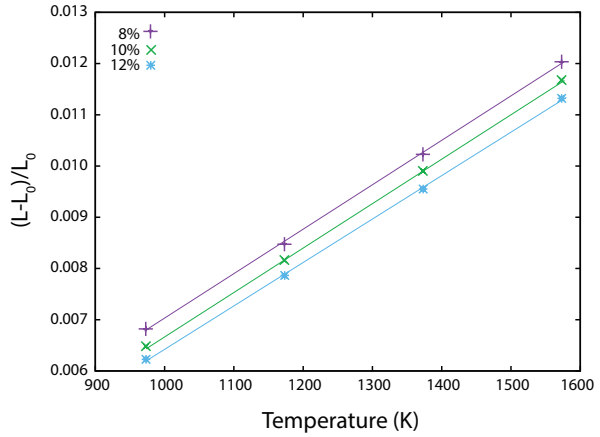


FIGURE 4.4: Bulk linear expansion of 8%, 10% and 12% YSZ, for the temperature range 973K - 1573K. All curves exhibit one slope each, indicating one expansion coefficient for each dopant concentration across this temperature range

TABLE 4.3: Thermal expansion coefficients (TEC) for each dopant 8, 10 and 12% dopant concentration of YSZ, determined from the slopes from Figure 4.4

| **Dopant Concentration** | **TEC ($\times$ $10^{-6}$ / K)** |
|---|---|
| **8%** | 8.692 $\pm$ 0.011 |
| **10%** | 8.667 $\pm$ 0.016 |
| **12%** | 8.489 $\pm$ 0.018 |

### 4.3.2 Diffusion

The mean squared displacements (MSDs) of the oxide ions, averaged over the three configurations for 8%, 10% and 12% YSZ, at 1573K, for the 1ns simulations, are demonstrated in Figure 4.5. The curves of all three dopant concentrations can be seen to possess the same initial slope, which then diverges at $\approx$ 200ps, with higher dopant concentration resulting in lower diffusivity. The slope of 12% YSZ becomes noticeably less steep for the final $\approx$ 700ps, compared to its inital slope. The decrease in diffusivity with increased dopant concentration can be seen from this figure to be time dependent, with the effect caused by the dopant ions taking time to manifest itself. The MSDs of the cations were also investigated and it was confirmed that they exhibited no diffusive behaviour for the temperatures or dopant concentrations studied.

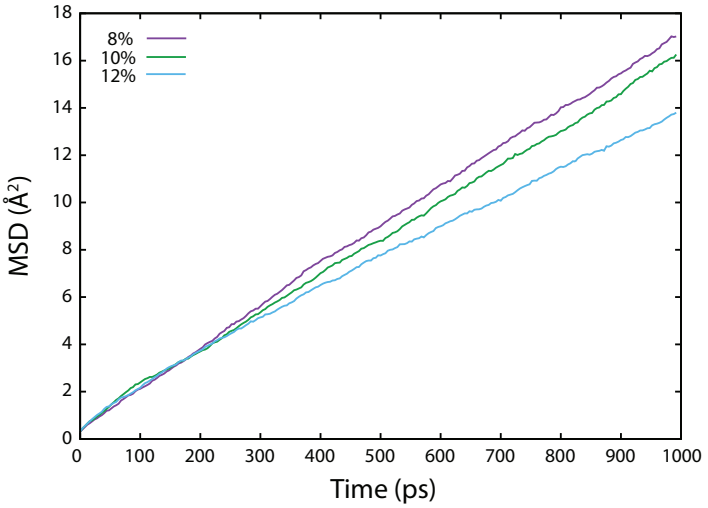


FIGURE 4.5: MSDs (averaged over 3 configurations) for 8%, 10% and 12% YSZ at 1573K

The trend exhibited by the diffusion coefficients for 8%, 10% and 12% YSZ are given numerically in Table 4.4 and are shown in Figure 4.6. For all dopant concentrations, the diffusion coefficient of the system increases with increasing temperature, agreeing with what was found for the diffusion coefficient of $CaF_2$. Additionally, across the entire temperature range studied (973K - 1573K), the bulk system with 8% yttria dopant concentration demonstrates the highest diffusion coefficient and 12% the lowest. Within the literature, either 8% or 10% are given as the dopant concentration that result in the system with the highest ionic conductivity, with any increase in dopant content reported to have a detrimental effect on the conductivity [13, 157, 162–164].

TABLE 4.4: Diffusion coefficients ($\times 10^{-7}$ cm$^2$/s) of YSZ for a range of temperatures and yttria concentrations

| | **8%** | **10%** | **12%** |
|---|---|---|---|
| **973K** | 0.0765 ± 0.0099 | 0.0699 ± 0.0039 | 0.0561 ± 0.0145 |
| **1173K** | 0.3423 ± 0.0633 | 0.3115 ± 0.0262 | 0.2947 ± 0.0290 |
| **1373K** | 1.1582 ± 0.0621 | 1.0078 ± 0.0460 | 0.9285 ± 0.0758 |
| **1573K** | 2.7866 ± 0.0478 | 2.6053 ± 0.1283 | 2.2016 ± 0.1540 |

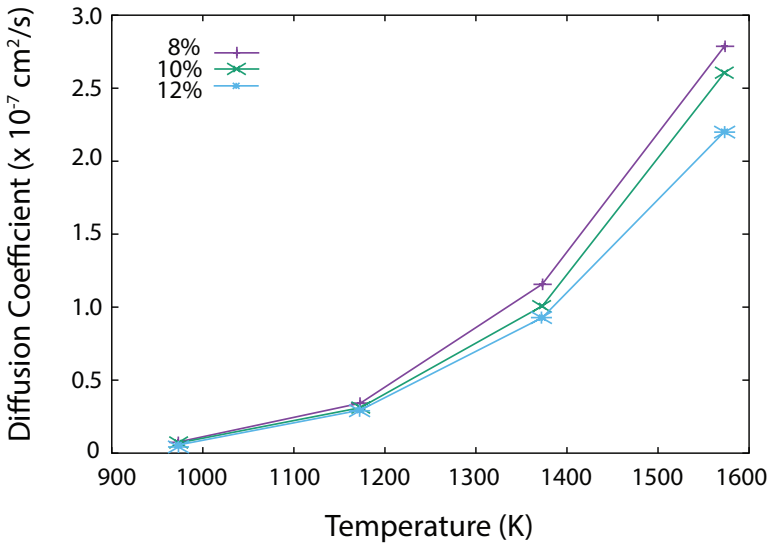


FIGURE 4.6: Diffusion coefficients for bulk YSZ for 8%, 10% and 12% YSZ from Table 4.4

### 4.3.3 Ionic Conductivity

Using the diffusion coefficients from the MSDs and the Nernst-Einstein equation (Equation 2.25), the ionic conductivities of the YSZ bulk system for all dopant concentrations at various temperatures were calculated and given in Table 4.5. The range of conductivities is consistent with previous experimental [13, 182, 183] and theoretical [14, 164, 181] studies. The experimental study by Kondoh et al. [183] found the conductivity range for 8% YSZ in the temperature range 1073K - 1573K to be 0.025 - 0.55 S/cm. Lau et al. [181] carried out a molecular dynamics study, based on the shell model [141], of 3 - 12% doped YSZ and found that the maximum ionic conductivity occurred at 8% dopant concentration, with values ranging from 0.005 - 0.07 S/cm for the temperature range 800K - 1200K.

TABLE 4.5: Ionic conductivities, $\sigma$ (S/cm), for 8%, 10% and 12% doped YSZ for the temperature range 973K-1573K

| | **8%** | **10%** | **12%** |
|---|---|---|---|
| **973K** | 0.0033 ± 0.0004 | 0.0029 ± 0.0001 | 0.0023 ± 0.0006 |
| **1173K** | 0.0120 ± 0.0022 | 0.0108 ± 0.0009 | 0.0101 ± 0.0010 |
| **1373K** | 0.0346 ± 0.0018 | 0.0296 ± 0.0011 | 0.0272 ± 0.0021 |
| **1573K** | 0.0724 ± 0.0010 | 0.0667 ± 0.0028 | 0.0559 ± 0.0037 |

Figure 4.7 plots ln $\sigma$T as a function of reciprocal temperature for 8%, 10% and 12% dopant concentration YSZ calculated from this study, to visualise the ionic conductivity changes with dopant concentration. Some literature data has been included to highlight their similarity with conductivities found in this study.

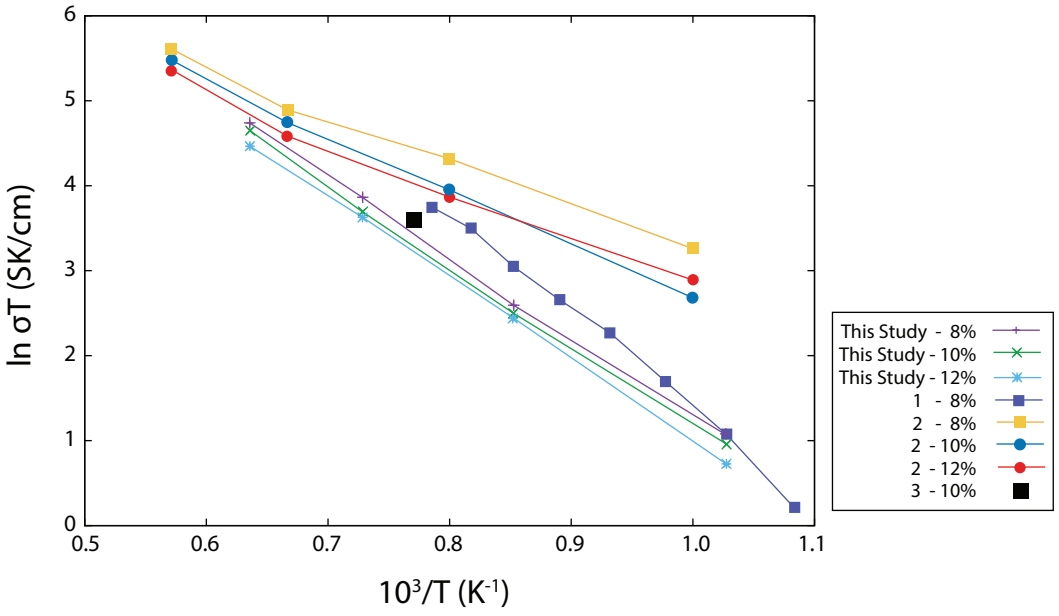


FIGURE 4.7: Ionic conductivities of doped YSZ calculated in this study and from literature, denoted as 1 [13], 2 [14] and 3 [15]

The experimental ionic conductivities are up to 0.64% higher than that calculated in this study for 8% doped YSZ, with the difference decreasing with increasing temperature. These values are much closer to experimental values than those of bulk $CaF_2$, which were approximately 25% lower. The oxide ions in YSZ diffuse via a vacancy mechanism, for which the Haven ratio equals the tracer correlation factor, which was assumed to be one, indicating uncorrelated atomic motion of the charge carriers (see Section 2.3.1.3). The close agreement with experimental results indicates that this assumption in Equation 2.25 is valid.

For all temperatures, the 8% dopant concentration was seen to exhibit the highest ionic conductivity compared to other concentrations, and increasing that concentration had an adverse effect on the conductivity, consistent with literature [13, 157, 162–164, 181].

#### 4.3.3.1 Activation Energy

As the ionic conductivity is linear across the entire temperature range studied (from Figure 4.7), it is constant for each dopant concentration. The activation energies for the 8%, 10% and 12% doped YSZ systems are given in Table 4.6.

The activation energy can be seen to increase with increasing yttria concentration. An increase in $E_A$ causes a reduction in the conductivity of the diffusing oxide ions [160, 184]. The system doped with 8% yttria exhibited the lowest activation energy, which then increased with increasing dopant concentration. This is consistent with the 8% doped system exhibiting the highest diffusivity and ionic conductivity.

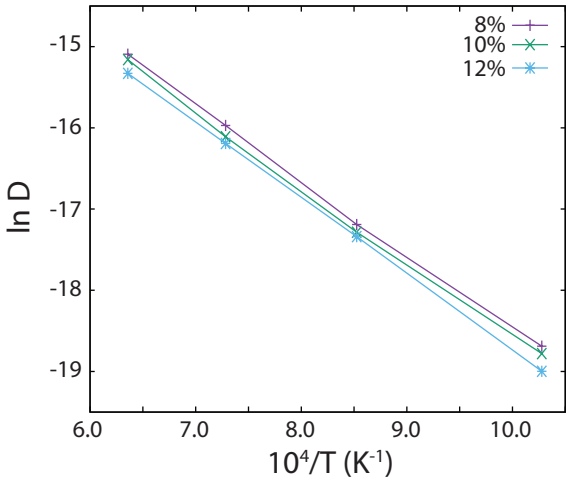


FIGURE 4.8: Arrhenius plot of the diffusion of 8%, 10% and 12% YSZ for the temperature range 973K - 1573K

TABLE 4.6: Activation energies, $E_A$, of 8%, 10% and 12% doped YSZ across the temperature range 973K - 1573K, given in kJ/mol and eV

| | $\mathbf{E_A}$ **(kJ/mol)** | $\mathbf{E_A}$ **(eV)** |
|---|---|---|
| **8%** | 76.452 ± 0.390 | 0.792 ± 0.004 |
| **10%** | 76.479 ± 0.101 | 0.793 ± 0.001 |
| **12%** | 77.767 ± 0.008 | 0.806 ± 0.0001 |

Activation energies for 8 - 10% YSZ have previously been reported by theoretical studies to be in the range of 0.37 - 1.0 eV [14, 157, 164, 181, 185, 186], while experimental studies have reported a slightly higher range of 0.70 - 1.2 eV [13, 183, 187–190]. The $E_A$ values found here are within the range of both theoretical and experimental studies, highlighting the ability of the potential and method used in this work to accurately predict bulk behaviour.

### 4.3.4 Vacancy Analysis

The ionic diffusion within YSZ is associated with atomic defects within the system. As such, any interactions between these defects will have an impact on the diffusivity of the material. It has been suggested that the vacancy ordering within YSZ is determined by: vacancy-vacancy > dopant-vacancy >> dopant-dopant interactions [165]. The dopant-vacancy interactions and vacancy-vacancy interactions will therefore be examined in detail here. The $Zr^{4+}$-dopant interaction is also considered to demonstrate how the addition of $Y^{3+}$ cations alters the cation-vacancy ordering.

#### 4.3.4.1 Cation - Vacancy Ordering

The dopant cation-vacancy partial RDFs demonstrate how the vacancies within the system order themselves in relation to the dopant $Y^{3+}$ cations. This can be compared to the Zr - O partial RDF of the pure $ZrO_2$ system, as it represents a random vacancy distribution [47]. The lattice constants will be slightly different, as the concentration of dopants within the system affects this, as has already been demonstrated. Dopant cations with a radius smaller than the cation they are replacing are expected to have vacancies in the nearest neighbour (NN) position, whereas dopants that are larger are expected to have vacancies in the next nearest neighbour (NNN) position [166**?** –170]. The $Y^{3+}$ cation has been reported to be larger than $Zr^{4+}$ cation (1.04Å compared to 0.84 Å [175]).

8% doped YSZ was selected to be exhibited here, as it is the dopant concentration that demonstrates the maximum ionic conductivity, and is therefore the most suitable for use in efficient oxide-ion diffusion based devices. The $Y^{3+}$ - vacancy partial RDF of 8% YSZ is given in Figure 4.9. It exhibits a considerable decrease in peak height for the NN position, compared to the random distribution and to the enhanced NN peak of the $Zr^{4+}$-vacancy partial RDF. The NNN position of the $Y^{3+}$ - vacancy partial RDF is seen to be much more popularly occupied, compared to the random distribution and compared to the NNN of the $Zr^{4+}$-vacancy partial RDF. This indicates that oxygen vacancies tend to occupy the NN position of $Zr^{4+}$ cations and the NNN position of $Y^{3+}$ cations. This is in agreement with that found using theoretical studies [166, 191, 192], nuclear magnetic resonance (NMR) [193] and extended x-ray absorption magnetic resonance (EXAFS) [167, 168] experiments.

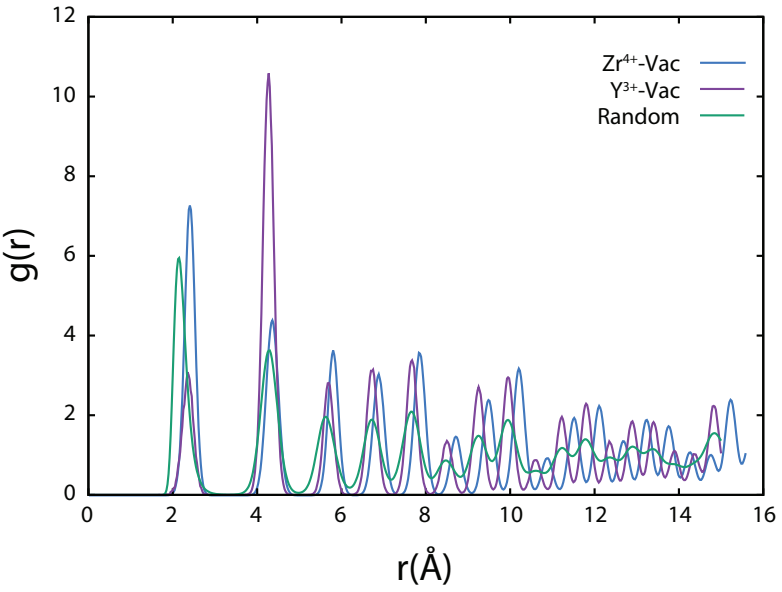


FIGURE 4.9: Cation-vacancy partial RDFs for $Zr^{4+}$ and $Y^{3+}$, compared with random distribution, of 8% dopant concentration bulk YSZ, at 1373K

Integrating the peaks of the $Y^{3+}$-vacancy partial RDF, shown in Figure 4.9, gives the number of vacancies that are coordinated to the dopant cations and are reported in Table 4.7. The coordination of the 8% doped YSZ bulk system at 1173K and 1573K are also provided, to enable comparison of temperature effects.

TABLE 4.7: Number of vacancies surrounding a $Y^{3+}$ dopant cation and a $Zr^{4+}$ cation in the nearest neighbour (NN) and next nearest neighbour (NNN) position for 8% doped YSZ at 1173K, 1373K and 1573K. The coordination of oxygen atoms surrounding a $Zr^{4+}$ cation in the pure $ZrO_2$ system is included as it represents a random distribution.

| | | **NN** | **NNN** |
|---|---|---|---|
| **1173K** | $Y^{3+}$-Vac | 0.639 | 2.848 |
| | $Zr^{4+}$-Vac | 1.419 | 1.216 |
| **1373K** | $Y^{3+}$-Vac | 0.794 | 3.293 |
| | $Zr^{4+}$-Vac | 1.722 | 1.447 |
| **1573K** | $Y^{3+}$-Vac | 0.856 | 3.480 |
| | $Zr^{4+}$-Vac | 1.740 | 1.585 |
| **Random** | | 1.309 | 1.094 |

Compared to the random distribution, for all temperatures studied, there is a definite decrease (of ≈ 35 - 50%) in the number of oxygen vacancies positioning themselves in the NN position to the $Y^{3+}$ ions. This is accompanied by an increase (of ≈ 10 - 30%) in the number of oxygen vacancies positioning themselves in the NN position to the $Zr^{4+}$ ions. The number of vacancies coordinating in the NNN position to the $Y^{3+}$ and $Zr^{4+}$ cations also changes with respect to the random distribution. The $Y^{3+}$ cations see a large increase (of ≈ 160 - 220%), while the $Zr^{4+}$ cations sees a smaller increase (of ≈ 10 - 45%), compared to the random distribution. Comparing the vacancy coordination numbers of the $Zr^{4+}$ and $Y^{3+}$ cations highlights the preferential placement of oxygen vacancies in the NN position of the $Zr^{4+}$ and the NNN of the $Y^{3+}$ cations. The decrease in coordination number for the NNN compared to the NN position of the $Zr^{4+}$ cation is significantly less extreme than the increase seen for the $Y^{3+}$ dopant cation (with a ≈ 15% decrease, compared to a ≈ 320% increase). This indicates that the $Y^{3+}$ dopant cations have a much more substantial influence on the ordering of oxygen vacancies in their vicinity. An increase in temperature, within the range considered, can be seen to result in an increase in the coordination number of vacancies in both the NN and NNN positions of both cations. The temperature does not, however, effect the relative change experienced by the doped system compared to the random distribution.

This data indicates that the oxygen vacancies tend to position themselves in the first O-coordination sphere of $Zr^{4+}$ and the second O-coordination sphere of $Y^{3+}$. With increasing dopant concentration, the binding tendencies of $Zr^{4+}$ cations to oxygen vacancies in the NN position becomes weaker. This was observed in a previous MD study of YSZ [194], and was postulated to occur as a result of it becoming more difficult for the oxygen vacancies to avoid the dopant cations as the concentration of $Y^{3+}$ cations, and correspondingly the concentration of oxygen vacancies, increases.

#### 4.3.4.2 Vacancy - Vacancy Ordering

It has previously been shown that with cation-vacancy ordering, there is accompanying vacancy-vacancy ordering in fluorite-structured materials [194–197]. The vacancy-vacancy partial RDF demonstrates how the vacancies order themselves with respect to one another, and can be compared to the O - O partial RDF from pure $ZrO_2$, which represents a random vacancy distribution. Figure 4.10 presents the average vacancy-vacancy partial RDF over the three configurations for 8% doped YSZ at 1373K and the random distribution. The vacancies display a high degree of long range ordering, as indicated by the sharp peaks extending to large interatomic distances. The labels on the peaks e.g. $\langle 100 \rangle$, $\langle 110 \rangle$ etc. indicate the different directions along the simple cubic anion sublattice, along which vacancy pairs can order. The tendency of the vacancies to order along certain directions, with respect to the random distribution, do not change as a function of the dopant concentrations, nor as a function of the temperatures, studied here.

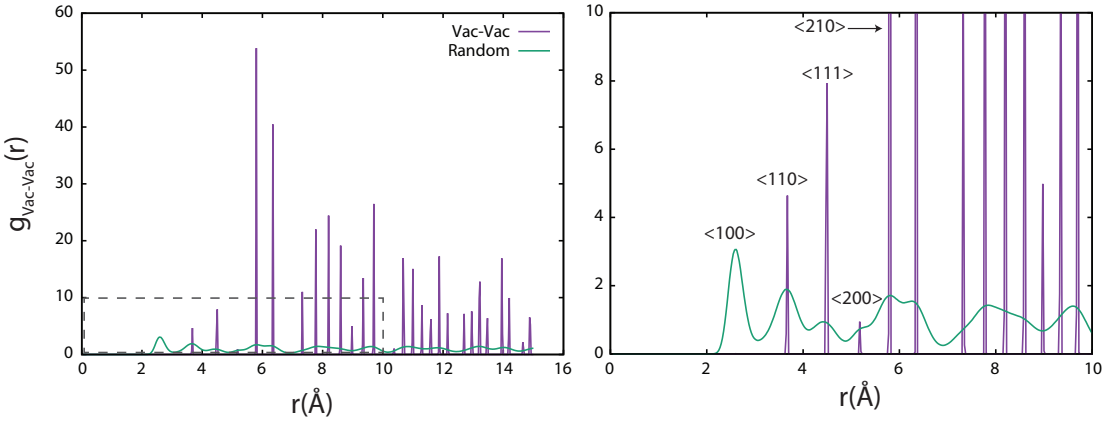


FIGURE 4.10: Vacancy-vacancy partial RDF ($g_{Vac-Vac}$) compared with random distribution, of 8% dopant concentration bulk YSZ, at 1373K. The image on the right is a zoomed in representation of the dashed box from the left figure. The labels indicate different directions along the simple cubic anion sublattice

The $\langle 100 \rangle$ peak is non-existent in the vacancy-vacancy partial RDF and is not present for any dopant concentration at any temperature studied. This underpopulation at short interatomic distance arises as a result of the repulsive Coulombic forces present between the vacancies due to the +2 lattice-relative charge they carry. This repulsion has been seen previously in fluorite structured materials [47, 194, 196, 198]. These studies, however, found that the repulsive forces extended to the $\langle 110 \rangle$ peak, which is inconsistent with the findings in this

study. This increase, compared to the random distribution, is found to persist across all dopant concentrations and temperatures under investigation here.

Of agreement with literature results, is the increase in peak height in the ⟨111⟩ direction, relative to the random distribution [196, 199] The ⟨200⟩ position is a particularly unfavourable direction, outside the range of influence of Coulombic repulsive forces, for vacancies to order along, in agreement with that found in [194]. The ⟨210⟩ peak is the highest peak in the vacancy-vacancy RDF, in agreement with a study by Parkes et al. [200] who used density functional theory to determine that the lowest energy dopant structures have oxygen vacancy pairs preferentially aligned along the ⟨210⟩ direction.

The peaks of the vacancy-vacancy partial RDF can be integrated, to give the number of vacancies coordinated around another vacancy. The coordination numbers for the first three peaks observed in Figure 4.10 are given in Table 4.8. The coordination number for the 1173K and 1573K 8% doped YSZ bulk system are also included, to identify temperature effects.

TABLE 4.8: Number of vacancies surrounding another vacancy along the ⟨100⟩, ⟨110⟩ and ⟨111⟩ directions of the 8% doped YSZ bulk system at 1173K, 1373K and 1573K

| | **⟨100⟩** | **⟨110⟩** | **⟨111⟩** |
|---|---|---|---|
| **1173K** | 0.0001 | 0.0701 | 0.1201 |
| **1373K** | 0.0001 | 0.0952 | 0.1270 |
| **1573K** | 0.0006 | 0.1373 | 0.1359 |

The ⟨100⟩ direction can be seen, for all temperatures, to be severely neglected. The coordination number clearly demonstrates the preference of vacancy pairs to align along the ⟨111⟩ directions, with less of a tendency to order along the ⟨110⟩ direction. An increase in temperature can be seen to consistently increase the vacancy-vacancy coordination number along all three directions, as has been observed in a previous MD study of YSZ [198], without affecting the relative occupation of the directions.

The short-range repulsion between vacancies is prevalent across all dopant concentrations and temperatures studied. As the dopant concentration is increased in YSZ, so too does the vacancy concentration increase. These vacancies will attempt to minimise their interactions with one another by ordering across the lattice. This ordering limits the mobility of the vacancies by correlating their motion [201] and as such, has a detrimental effect on the ionic conductivity of the material, as demonstrated in Figure 4.7.

## 4.4 Surfaces

The (100), (110), (111), (210), (221) and (310) YSZ surfaces, doped with 8%, 10% and 12% yttria were investigated by examining the 2-dimensional planar diffusion along slices of the surface slab, parallel to the surface plane. The surface effects on the ionic diffusion were examined and compared to other dopant concentrations of the same surface orientation, other surface orientations and to that of the bulk.

### 4.4.1 Surface Stability

The surface energies of all six surface orientations, for all three dopant concentrations, were calculated and the surface energies for the surfaces doped with 8% yttria are given in Table 4.9, listed according to their relative stability.

TABLE 4.9: Calculated surface energies ($Jm^{-2}$), $\gamma$, for the YSZ surface orientations studied, with 8%, dopant concentration, listing according to their order of stability

| | **8%** |
|---|---|
| **(111)** | 0.127 |
| **(221)** | 0.249 |
| **(110)** | 0.300 |
| **(210)** | 0.317 |
| **(310)** | 0.332 |
| **(100)** | 0.350 |

The 10% and 12% doped surface orientations demonstrated the same trend in surface orientation as for the 8% doped surfaces, with the exception of the (100) and (310) 12% doped surface. These surfaces demonstrated the opposite trend to that experienced by their 8% and 10% doped counterparts. The relative stability ordering found here, if the (221) surface is excluded, is (111) > (110) > (210) > (310) > (100), which agrees with that found for the $CaF_2$ surfaces. For all dopant concentrations of YSZ, the (221) surface possesses the second lowest surface energy, while for the $CaF_2$ surfaces, it was found to exhibit the second highest. This indicates that the (221) YSZ surface has a much greater stability, relative to the other surface orientations, than its $CaF_2$ counterpart. This could be as a result of oxygen vacancy segregation within the YSZ surface slabs.

The (111) surface of fluorite structured materials has been well documented as being the most stable surface orientation [64, 143–145, 202**?** ]. Xia et al.'s [172] study of $ZrO_2$ surfaces found a relative stability ordering of (111) > (110) > (100) > (310), in agreement with the 12% dopant concentration from this study. Having determined the (111) and (110) surfaces to be the most stable, they calculated the surface energies for 0 - 50% dopant concentration. The surface energies of both of these surfaces were found to be reduced from their undoped $ZrO_2$ energies, which signifies that they were both stabilised by yttrium doping. The relative stabilities of the (111) and (110) were found to remain constant. Balducci et al. [173] studied three cubic-$ZrO_2$ surfaces using atomistic models and found a relative stability of (111) > (110) > (310). The findings from both of these studies are consistent with the relative surface energies found here.

Jiang et al's [146] study of $CeO_2$ found a relative stability order of (111) > (110) > (210) > (100) > (310), agreeing with Xia et al.'s study and consistent with the 12% doped system from this study. The relative order of $UO_2$ surfaces from Williams et al. [64] was determined to be (111) > (221) > (310) > (210), which disagrees with the relative stability of the (310) and (210) surfaces in this study. The order does, however, correspond better with the YSZ surfaces than with those of $CaF_2$, where only the (111) surface's relative stability corresponded.

Despite all of these materials possessing the fluorite structure, there remains disagreement as to the relative order of stability of surface orientations. The base structure can, therefore, not be used to wholly determine the stability ordering, as the composition of the material is seen to exert a considerable influence. The order of stability for the YSZ surfaces generated here, however, can be seen to be consistent with a number of fluorite structured systems, indicating the validity of the method and potential parameters used.

### 4.4.2 Vacancy Segregation

The surface orientations were all run at a high temperature (1573K) to allow the oxygen vacancies, which were randomly distributed, to reposition themselves within the surface slab. This migration is effected by the orientation of the surface. The surface energy is believed to play a part in determining the extent of vacancy segregation, where a higher surface energy would indicate greater vacancy segregation to that surface [14].

Figure 4.11 demonstrates the number of oxygen vacancies in each of the slices of the 8% YSZ (111) surface slab, averaged over three initial random configurations for the surface slab. The atomic structure of the (111) surface slab is also included to demonstrate the layers within the slab from which the number densities were calculated. The vacancy density for the inital structure is randomly spread out, with no systematic preference for positioning. After 20ps of 1573K temperature scaling, the vacancies show a much greater degree of ordering. There is a definite increase in vacancy density for the two uppermost surface slices, with a decrease observed in the subsurface layers, in agreement with literature findings [173]. The slices within the bulk regions of the surface slab exhibit roughly the same density of vacancies.

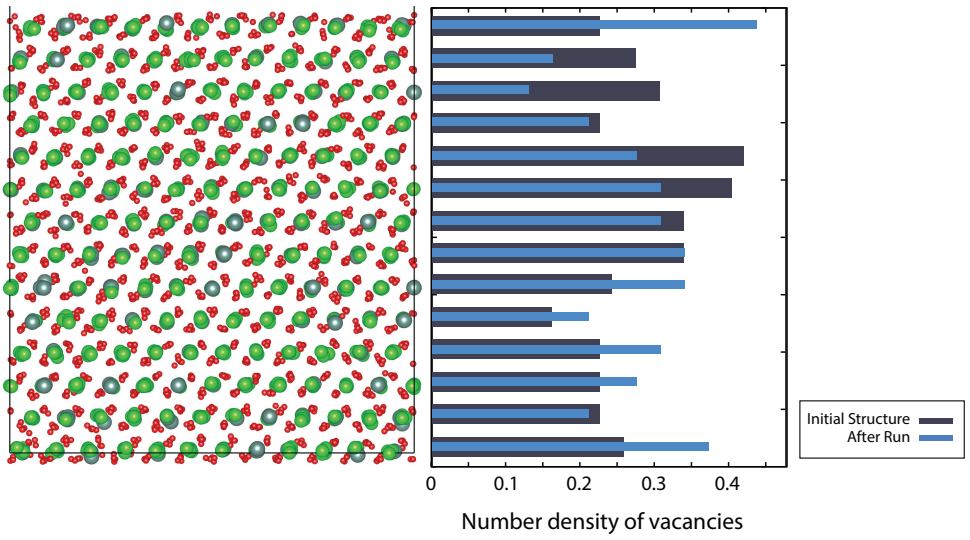


FIGURE 4.11: Number density of oxygen vacancies for each slice of the 8% YSZ (111) surface slab. Demonstrating the movement of vacancies from their inital, random positions after the 20ps 1573K simulation. The atomic structure of the (111) surface slab after the 1573K run is given to demonstrate the slices, the green sphere are $Zr^{4+}$ cations, the grey are $Y^{3+}$ cations and the small red spheres are $O^{2-}$ anions)

A similar investigation into the vacancy segregation was carried out for all surface orientations. Figure 4.12 presents the number density of oxygen vacancies within each slice of all of the surface slab orientations, all doped with 8% yttria, for the initial structure compared to that after 20ps 1573K run. All of the data presented here is averaged over three randomly generated configurations for each surface slab.

The post-MD run for the (100), (110), (111), (210) and (310) surface orientations all display a definite increase in oxygen vacancy concentration in the surface layers, with a roughly equal concentration of vacancies within the bulk regions of the slabs. The (110) surface also demonstrates a marked reduction in vacancy concentration in its subsurface layers compared to both the surface layers and the concentration levels within the bulk of the slab. The high vacancy concentration for the surface layers, accompanied by a depletion in subsurface layers has been previously reported [14] and found to result in an increase in oxygen diffusion at the surface. The (221) surface slab exhibits a decreased concentration of oxygen vacancies in its surface layers after the MD run, compared to its subsurface layers. This is the only surface studied that exhibited a migration of oxygen vacancies away from the surface layer.

The number density of vacancies present in the surface slices for all orientation can be compared to the surface stability previously determined for 8% doped YSZ; (111) > (221) > (110) > (210) > (310) > (100). The (111) and (221) surface orientations possess the lowest surface energies, consistent with them demonstrating the lowest vacancies concentration at their surfaces. The (210) and (310) surface orientations possess the highest surface energies and can be seen to demonstrate the highest vacancy concentrations in their surface layers.

### 4.4.3 Depth Analysis of Diffusion

The diffusion of each of the surface slabs was investigated as a function of depth to identify the surface effects of each surface orientation at all three dopant concentrations. The diffusion depth profile of the (100) surface, doped with 8% yttria at 1373K is given in Figure 4.13, as is its average atomic structure. The (100) surface was selected to be discussed in detail, as from Table 4.9, it was found to have the highest surface energy, and therefore is expected to be the least stable surface orientation.

The average position of the $O^{2-}$ ions within the (100) surface slab clearly demonstrate enhanced displacement in areas which display high diffusion coefficients (indicated by the large black arrows). The diffusion coefficient of these regions is less than that determined for the bulk for 8% YSZ at 1373K. The subsurface layers, which have the lowest diffusion coefficients, have the least disordered anion sublattice (indicated by the small grey arrows). These regions exhibit significantly reduced diffusion coefficients ($\approx$ 80%) compared to the bulk values. The depth profile of the $CaF_2$ surfaces exhibited enhanced diffusion at the surfaces for each orientation, coupled with a return to bulk-like diffusion coefficients within the centre of the slab. This is not the case here. The diffusion coefficient at the surfaces and within the bulk exhibit the highest values, however these The surface slab

The trend in diffusion coefficient observed for the (100) surface slab can be compared with its vacancies number density depth profile, demonstrated in Figure 4.12a. The uppermost surface slices possess the highest diffusion coefficient and have the highest number density of vacancies. There is a sharp decrease in diffusion coefficient observed in the third layer at both (100) surfaces, with a drop of $\approx 80\%$ from that of the second-to-surface layer. This drop is consistent with a decrease (of $\approx 45\%$) in number density of oxygen vacancies within these slices.

Figure 4.14 shows the diffusion depth profiles for all of the surface orientations, doped with 8% yttria, at 1373K. This plot highlights the effect different surface orientations have on the ionic diffusion. From this, only the (111) surface can be seen to exhibit diffusion coefficients higher than bulk levels at its surface. The remaining surfaces all exhibit diffusion coefficients that are smaller than those for bulk YSZ. The lowest diffusion coefficient for the (100), (110) and (310) surfaces is located in their subsurface layers.

The diffusion coefficients at the surfaces of all surface slab orientations for 8%, 10% and 12% dopant concentration are given in Table 4.10. The average diffusion coefficients of the bulk system for the corresponding dopant concentration are also stated, for comparison. All data in Table 4.10 was calculated for 1373K, and was found to exhibit the same trend in diffusion as for 1173K and 1573K, for each surface orientation.

TABLE 4.10: Average diffusion coefficients ($\times 10^{-7}$ cm$^2$/s) of the top and bottom surface of all YSZ surface orientations with 8%, 10% and 12% dopant concentration, all calculated at 1373K

| **Surface Orientation** | **8%** | **10%** | **12%** |
|---|---|---|---|
| **(100)** | 1.047 ± 0.038 | 0.936 ± 0.019 | 1.120 ± 0.015 |
| **(110)** | 0.373 ± 0.068 | 0.342 ± 0.084 | 0.429 ± 0.005 |
| **(111)** | 3.250 ± 0.131 | 2.607 ± 0.186 | 1.757 ± 0.253 |
| **(210)** | 0.386 ± 0.182 | 0.437 ± 0.206 | 0.490 ± 0.233 |
| **(310)** | 0.528 ± 0.089 | 0.427 ± 0.037 | 0.541 ± 0.047 |
| **(221)** | 0.624 ± 0.163 | 0.494 ± 0.019 | 0.570 ± 0.042 |
| **Bulk** | 1.158 ± 0.001 | 1.008 ± 0.001 | 0.929 ± 0.006 |

Figure 4.15 presents the number density of oxygen vacancies after the 20ps 1573K run for all surface orientations investigated (from Figure 4.12) with the diffusion coefficients (from Figure 4.14) to provide an indication of how the diffusivity of each slice is effected by the vacancy density. From this figure a very general trend can be detected, where a decrease in number density of vacancies corresponds to a decrease in the diffusion coefficient of that slice. This is seen mostly clearly in the third-to-surface layer of the (100) surface orientation and the second-to-surface layer of the (110) surface orientation. Likewise, a slice with increased vacancy number density generally demonstrates enhanced diffusivity, mainly exemplified by the (111) surface orientation.

The (111) surface orientation was seen to demonstrate an increase in diffusion at its surface, compared to bulk levels, for all dopant concentrations, across all temperatures studied. This surface orientation was found to have the lowest surface energy, as was also found for the $CaF_2$ surfaces, which has been postulated to indicate a low migration of vacancies to the surface [14]. The work carried out in this study found that there were more vacancies present at the surfaces than predicted by the random distribution and compared to the vacancy densities of the other slices within the surface slab. This increase in vacancy density was seen to correspond with an increase in diffusion coefficient, unlike in [14] where a decreased diffusivity was observed and was attributed to a depletion of oxygen vacancies. It was also the only YSZ surface orientation studied whose diffusivity surpassed that of the bulk system at its surfaces, with a diffusion coefficient $\approx 3$ times than that of the bulk (as seen in Figure 4.14).

Not all increases in vacancy number densities corresponded with an increase in diffusion coefficient, as demonstrated, in particular, by the surface layers of the (110), (210) and (310) surface orientations. While there was a slight increase in diffusivity, compared to the second-to-surface layer for all orientations, this increase was not comparable to that observed for the (111) surface. The vacancy concentration for these surface layers is much higher than that for the (111), which could act as a deterrent to diffusion, due to an over-abundance of oxygen vacancies, at the expense of mobile $O^{2-}$ anions.

The level of diffusivity for the surface layers of the (111) surface are not obtained by any other slice within the other surface orientations, even if the slice had an equivalent vacancy number density to that of the (111) surface slices. The increased diffusion coefficient is therefore not purely dependent on the concentration of oxygen vacancies, but also on the environment of that slice.

The (111) surface orientation for all three dopant concentrations was found to possess the lowest surface energy (as given in Table 4.9), and therefore, greatest stability. From Figure 4.14 and Table 4.10, this orientation exhibits the greatest increase in diffusion coefficient at its surfaces. Conversely, the (100) surface was found to have the highest surface energy for 8% and 10%, and second highest for 12%, dopant concentration. This surface exhibits the second greatest increase in diffusion coefficient at its surfaces. There is, therefore, no correlation between the relative surface energies and the relative increase or decrease in diffusion coefficient observed for the YSZ surfaces.

#### 4.4.3.1 Sectioned Activation Energy

The diffusion as a function of depth data, for all surface orientations, dopant concentrations and temperatures studied, were examined. The slices of the surface slabs determined to be influenced by surface effects. They were classified as those slices that experienced diffusion coefficients that was outside the calculated error of that calculated for bulk YSZ for the corresponding dopant concentration.

These "surface" slices were grouped to form "surface regions". The remaining slices, experiencing diffusion coefficients similar to (within calculated error of) bulk levels were grouped to form "bulk regions". A schematic of the different regions present in the surface slabs was given in Figure 3.14. The number of slices used to generate the surface and bulk regions for each surface orientation, for each dopant concentration is given in Table 4.11.

TABLE 4.11: Number of slices taken from the top and bottom surface used to generate the "surface section", and the number of slices from the centre of the slab, used to generate the "bulk-like section", for all surface orientations and dopant concentrations of YSZ

| **Surface Orientation** | **# Surface Slices** | **# Bulk Slices** |
|---|---|---|
| **(100)** | $5 \times 2$ | 7 |
| **(110)** | $3 \times 2$ | 6 |
| **(111)** | $3 \times 2$ | 8 |
| **(210)** | $4 \times 2$ | 6 |
| **(310)** | $4 \times 2$ | 5 |
| **(221)** | $3 \times 2$ | 7 |

The activation energy of the bulk and surface regions of each slab were calculated separately. The Arrhenius plot for the (100) 8%, the (111) 8% and the (111) 12% YSZ surfaces are given in Figure 4.16. These were selected as they demonstrate that the behaviour of the slope of the "bulk" and "surface" regions is dependent on both the surface orientation and dopant concentration of the slab. Figure 4.16 shows that the 8% (100) surface section has a steeper slope than its bulk section, while the (111) surface sections exhibits a flatter slope for 8% doped, with a steeper slope for 12% doped YSZ. The Arrhenius plot for the bulk YSZ system with 8% and 12% dopant concentration is also included in Figure 4.16 and shows strong similarities to the bulk sections of the surface slabs.

The activation energies for the "surface" and "bulk" regions for all surface orientations and dopant concentrations are given in Table 4.12. These values are comparable to those reported for similar systems obtained via simulations [171, 203] and experimental methods [162, 188, 189]. Figure 4.17 shows the activation energies for the "surface" and "bulk" regions of all surface orientations, doped with 8% yttria, with the activation energy of the 8% bulk system given by the dashed line for comparison.

There is no definite trend between the dopant concentrations studied as to which surface orientation exhibits the highest surface activation energy. Nor is there a trend within surface orientations as to which dopant concentration results in the highest surface activation energy. The extent of ionic diffusion within YSZ is dependent on the concentration of dopant cations, which in turn determines the number of oxygen vacancies present in the system. Unlike $CaF_2$, where the mobile $F^-$ anions use interstitial sites to diffuse, the mobile $O^{2-}$ anions in YSZ require the presence of oxygen vacancies, which, can themselves, also move within the system. The position of oxygen vacancies have been seen to be influenced by surfaces within the system, with the type and extent of the influence being determined by the orientation of the surface.

TABLE 4.12: Activation energies (kJ/mol) for the "surface" and "bulk" regions of all surface orientations and dopant concentrations of YSZ, the activation energies for the corresponding bulk system have been included for comparison.

| | 8% | |
|---|---|---|
| | **Surface $E_A$** | **Bulk $E_A$** |
| **(100)** | 97.077 ± 3.370 | 81.137 ± 0.194 |
| **(110)** | 81.755 ± 1.534 | 90.012 ± 0.798 |
| **(111)** | 68.124 ± 2.156 | 79.728 ± 1.931 |
| **(210)** | 80.192 ± 0.436 | 89.109 ± 0.149 |
| **(310)** | 77.334 ± 1.383 | 82.282 ± 1.379 |
| **(221)** | 83.185 ± 0.085 | 77.133 ± 0.509 |
| **Bulk** | 76.452 ± 0.390 | |

| | 10% | |
|---|---|---|
| | **Surface $E_A$** | **Bulk $E_A$** |
| **(100)** | 82.398 ± 3.370 | 77.451 ± 1.398 |
| **(110)** | 90.110 ± 2.493 | 86.770 ± 1.294 |
| **(111)** | 77.192 ± 0.758 | 77.192 ± 0.802 |
| **(210)** | 87.868 ± 2.876 | 87.868 ± 2.145 |
| **(310)** | 68.918 ± 0.900 | 68.918 ± 0.269 |
| **(221)** | 79.734 ± 3.033 | 79.734 ± 0.293 |
| **Bulk** | 76.479 ± 0.101 | |

| | 12% | |
|---|---|---|
| | **Surface $E_A$** | **Bulk $E_A$** |
| **(100)** | 90.193 ± 4.818 | 83.990 ± 1.180 |
| **(110)** | 89.630 ± 1.939 | 77.001 ± 0.240 |
| **(111)** | 79.434 ± 1.726 | 73.700 ± 1.908 |
| **(210)** | 78.627 ± 2.511 | 86.658 ± 1.230 |
| **(310)** | 76.079 ± 0.480 | 74.947 ± 0.470 |
| **(221)** | 79.734 ± 0.068 | 76.734 ± 1.094 |
| **Bulk** | 77.767 ± 0.008 | |

## 4.5 Summary

The YSZ bulk results section (Section 4.3) demonstrated that the method and potential used in this study was capable of reproducing experimental results, such as thermal expansion coefficients, ionic conductivities and activation energies. The information gathered about the bulk system, doped with 8%, 10% and 12% yttria was used to compared with different surface slab orientations.

The motion of oxygen anions within the YSZ bulk system is affected by the placement and concentration of vacancies and dopants. Section 4.3.4 investigated the cation-vacancy and vacancy-vacancy interactions, as these were previously found to have the most impact on the vacancy ordering within YSZ. The larger size of the $Y^{3+}$ dopant cation, compared to the $Zr^{4+}$, was found to result in the vacancies preferentially positioning themselves in the next nearest neighbour position to the $Y^{3+}$ cations, compared to their tendency to occupy the nearest neighbour position of the $Zr^{4+}$ cations.

Examination of the vacancy-vacancy ordering saw that the vacancies did not align along the $\langle 100 \rangle$ direction, as a result of repulsive forces between the vacancies at such small distances, consistent with literature [47, 194, 196, 198]. The $\langle 111 \rangle$ peak exhibited an enhanced height, compared to that of the random distribution, indicating that vacancies preferentially aligned in this direction. Increases in temperature were found to not effect the relative concentration of vacancies aligned along the different directions along the simple cubic anion sublattice, but did cause an increase in the vacancy-vacancy coordination for all directions.

The surface section (Section 4.4) examines the effect the (100), (110), (111), (210), (310) and (221) surfaces have on the 8%, 10% and 12% doped YSZ system. The relative surface stability for all three dopant concentrations was initially determined and found to be (111) > (221) > (110) > (210) > (310) > (100) for the 8% and 10% doped surfaces. The 12% doped surface stability differed by the relative stability of the (100) and (310) surfaces ((100) > (310)). This order of stability differed slightly from that determined for the $CaF_2$ surfaces, but was found to agree with other fluorite structured surfaces [64, 146, 172]. This highlights the fact that the method and potential used are capable of generating an accurate representation of different YSZ surface orientations.

The diffusion within YSZ requires oxygen vacancies to allow the movement of mobile $O^{2-}$ anions to occur. The presence of surfaces have been documented to cause a migration of vacancies, either toward, or away from, the surfaces, depending on the orientation of the surface [14, 172**?** ]. In order to interpret the diffusion within these surface slabs as a function of depth, the migration of oxygen vacancies must first be understood. The concentration of vacancies at the surface was found to be correlated with the stability of that surface, in agreement with that found by Iskandarov and Umeno [14]. Lower energy surfaces, such as the (111) and (221) surfaces, were found to exhibit lower vacancy concentrations than surfaces with higher surface energies, such as the (210) and (310) surfaces.

The diffusion of each surface slab as a function of depth was investigated in Section 4.4.3. Only the (111) surface orientation exhibited increased diffusion at its surfaces, compared to bulk levels. This is unlike that observed for the $CaF_2$ surfaces, where all orientations exhibited an increased diffusion coefficient for the surface layers. The (111) $CaF_2$ surface exhibited the smallest increase in diffusion coefficient, compared to the other orientations studied. The differences between the behaviour of the (111) surface in YSZ and $CaF_2$ could be as a result of the generation of oxygen vacancies and their requirement in the diffusion mechanism in YSZ. The diffusion depth profile was compared to the vacancies number density of the slices within each surface slab. In general, an increase in vacancy concentration was found to result in an increase in diffusion coefficient, however for the (110), (210) and (310) orientations, the high vacancy concentration at the surfaces did not result in a comparably high diffusion coefficient. This suggests that there was an over-abundance of oxygen vacancies and insufficient numbers of mobile $O^{2-}$ anions available to diffuse.

The activation energies for the surface slabs were examined by sectioning the slabs into "surface" and "bulk" regions (using the same method as for the $CaF_2$ surfaces). Unlike for the $CaF_2$ surfaces, there is no general trend across all orientations as to which region exhibited the higher activation energy, which could be attributed to the segregation of vacancies in YSZ surfaces that the $CaF_2$ surfaces do not experience.

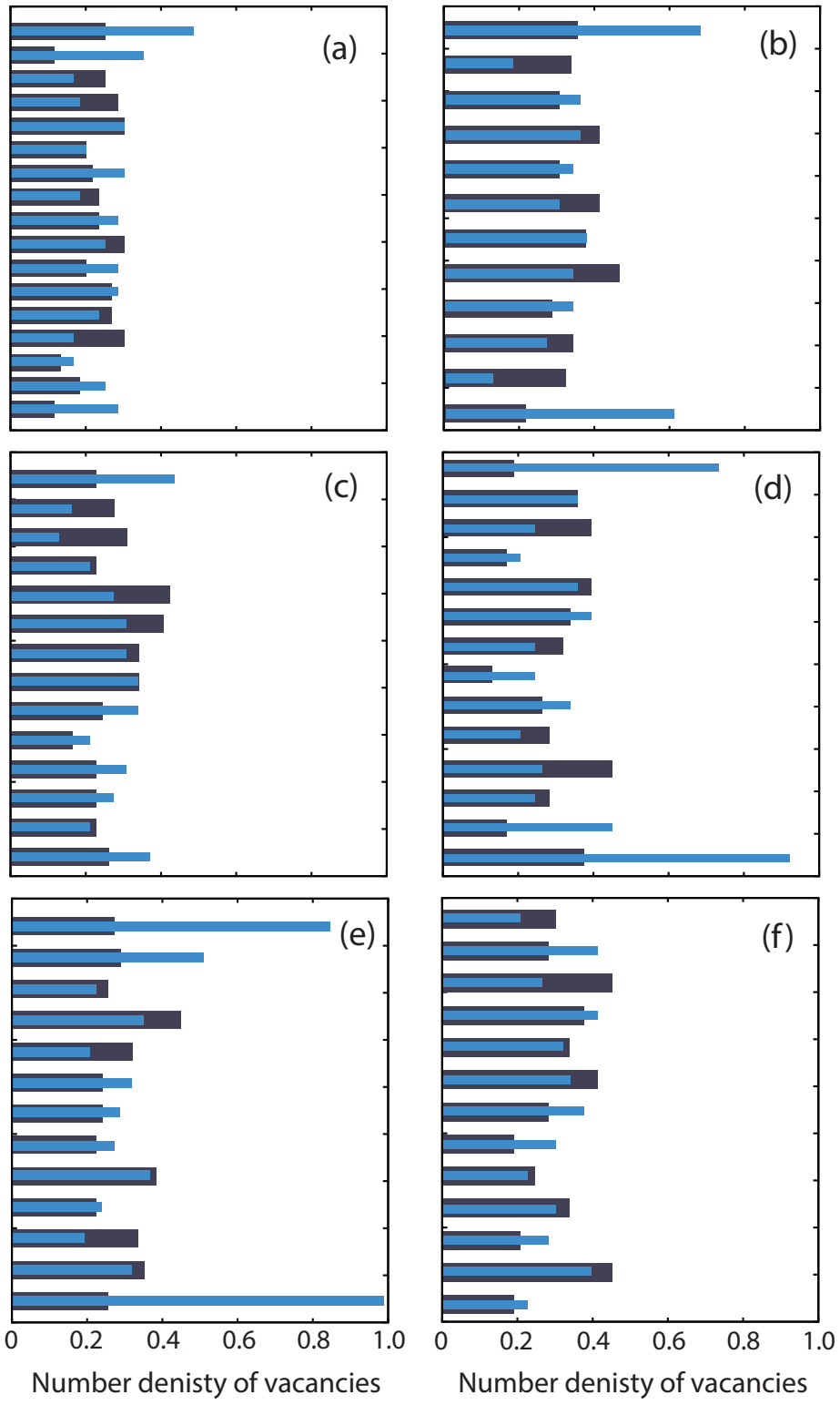


FIGURE 4.12: Number density of oxygen vacancies within each slice for all the surface orientations, doped with 8% yttria Demonstrating the movement of vacancies from their inital, random positions after the 20ps 1573K simulation.
(a) (100), (b) (110), (c) (111), (d) (210), (e) (310) and (f) (221).

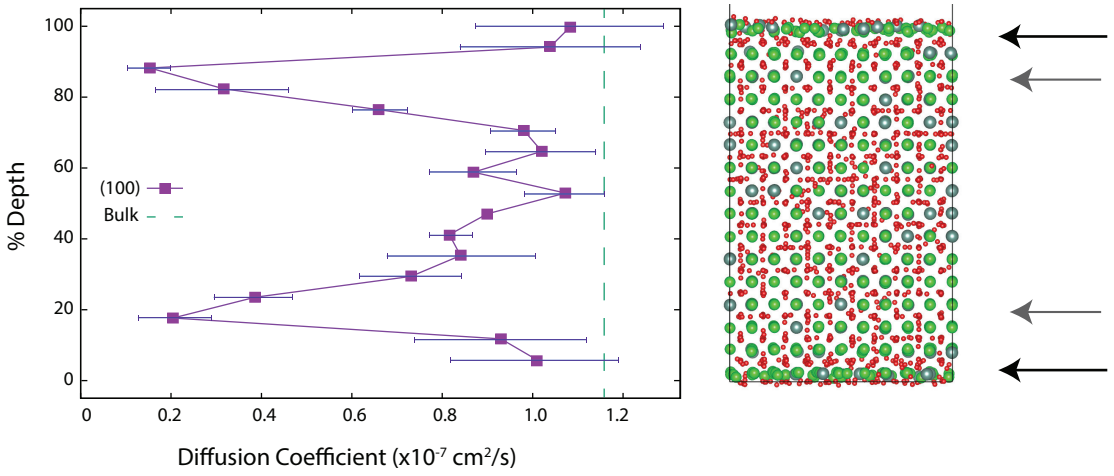


FIGURE 4.13: Diffusion depth profile of the (100) 8% YSZ surface at 1373K, with the average MD structure over the 1ns 1373K simulation ($O^{2-}$ - red, $Zr^{4+}$ - green, $Y^{3+}$ - grey). Large black arrows indicate areas with high diffusion coefficients, and smaller grey arrows indicate lower diffusion areas.

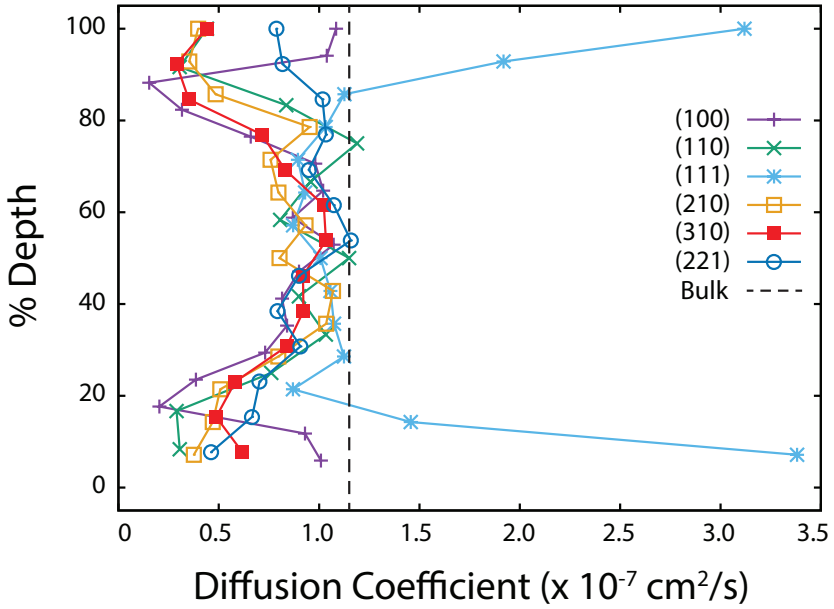


FIGURE 4.14: Comparison of diffusion depth profiles for all surfaces doped with 8% yttria at 1373K, the bulk diffusion coefficient for 8% YSZ at 1373K is included for comparison

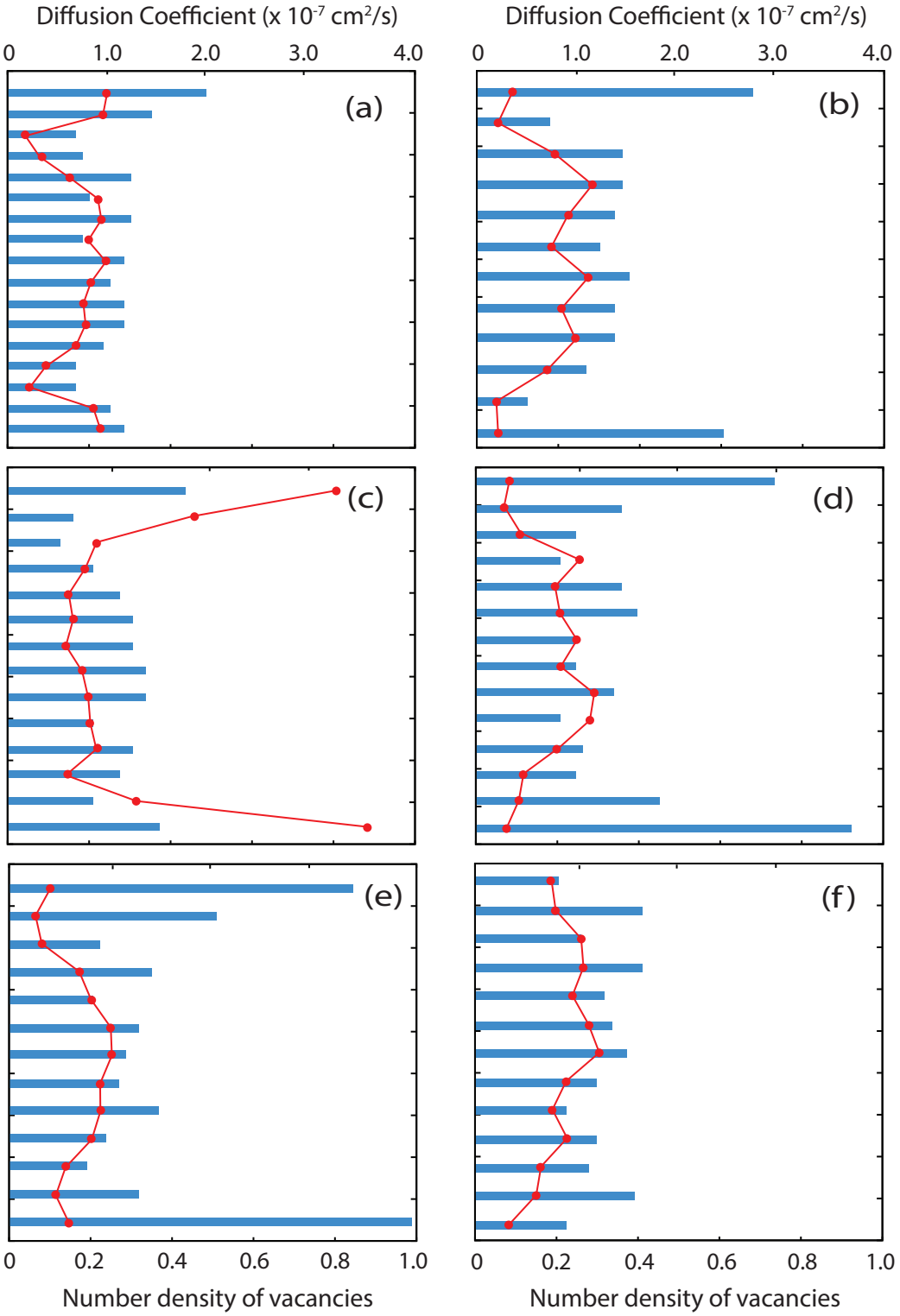


FIGURE 4.15: The number density of vacancies within each slice of the surface slabs, doped with 8% yttria after the 20ps 1573K run of the (a) (100), (b) (110), (c) (111), (d) (210), (e) (310) and (f) (221) surface orientation, compared to the diffusion coefficient of each slice from Figure 4.14

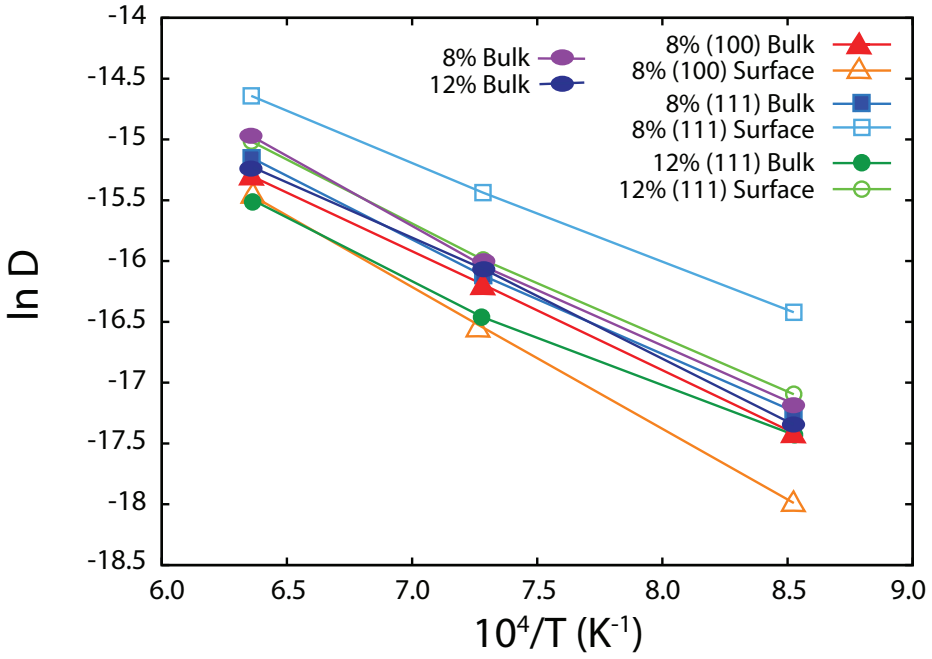


FIGURE 4.16: Arrhenius plot of the diffusion of the (100) 8%, the (111) 8% and the (111) 12% YSZ surface slabs, which are all separated into "surface" and "bulk" regions, at 1173K, 1373K and 1573K. The data from the bulk system with 8% and 12% dopant concentration is also included.

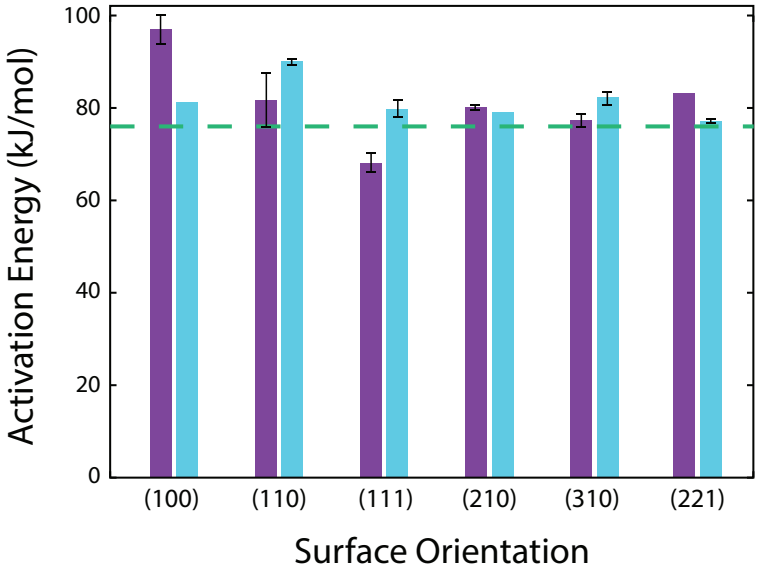


FIGURE 4.17: Activation energies of the surface sections (purple) and bulk sections (blue) of all YSZ surface slabs, doped with 8% yttria, compared to the activation energy of the bulk 8% YSZ system (green dashed line)

# Chapter 5: Conclusions and Future Work

## 5.1 Conclusions

The main motivation for this work was to investigate the effect multiple defects have on the ionic diffusion within fluorite-structured materials, using molecular dynamics with a highly accurate polarisable force field. Fluorite-structured materials are commonly used as the electrolyte in many electrochemical, diffusion based devices, which require a highly operating efficiency to be a feasible answer to the world's energy crisis. The diffusion process within these materials, and how it is effected by defects present within the system, must therefore be fully understood, before its process can be optimised.

$CaF_2$ was selected as a model fluorite structure due to its inherently fast ionic conduction. This allows for large amounts of data to be collected in a shorter time, compared to its oxide diffusing fluorite structured counterparts used in diffusion based devices, such as yttria-stabilised zirconia, which is the other material studied here.

The DIPPIM used was seen to correctly model both the structure and thermodynamic properties of bulk $CaF_2$ and YSZ by comparison with previous literature studies. This justifies its use for fluorite-structured materials. This clearly establishes that using interaction potentials to approximate the interactions of electrons, rather than considering them explictly, can give realistic material specific predictions, at a cheaper computational cost.

Strain is an important consideration when synthesising electrochemical devices as a result of lattice mismatch between different materials at component interfaces. Being able to accurately model the strain and understand the consequences it has on the ionic diffusion is key to unlocking the diffusion process across the device. Tensile strain applied to the bulk was observed to increase the diffusivity of the system, with 4% tensile strain exhibiting a large ($\approx 2\times$) increase in the diffusion coefficient, compared to the unstrained system, equivalent to a 150K increase in temperature. This phenomenon can be attributed a reduction in the system size, resulting in a more compact atomic structure which causes an increase in the movement of the mobile $F^-$ anions.

A common extended defect generated when synthesing bulk materials is the presence of surfaces. The lower coordination number of the atoms at the surface, compared to those within the bulk, can effect the diffusive properties in that region. The change in diffusivity is dependent on the orientation of the surface and the material being considered. All $CaF_2$ surface orientations experienced an increase in diffusion coefficient at their surfaces, with a return to bulk-level diffusivity within the centre of their slabs. This can be attributed to a decrease in activation energy at each surface. Unlike $CaF_2$, YSZ only exhibits enhanced diffusivity at the (111) surface. The discrepancy between the two materials can be attributed to the presence of mobile charge compensating vacacnies generated in YSZ, which can segregate within the surface slab, depending on the surface orientation.

The final extended defect considered for $CaF_2$ are tilt grain boundaries, which are generated by reflecting a surface to create its mirror image. For all boundary orientations, an increase in diffusivity was observed, of the same order of magnitude to that of the surfaces. This increase can be credited to the open structure of the grain boundaries, which generates facile diffusion pathways for the mobile $F^-$ ions.

Despite the many advantages of using $CaF_2$ as a model fluorite structure, its diffusive properties cannot be used as an indication as to how those of other, more complex, fluorite materials will perform, as observed by the comparison with YSZ. Nevertheless, the study of $CaF_2$ is beneficial for understanding the methods used to model the fluorite structure and how to analyse the fundamental diffusive properties within. YSZ has been previously used as the electrolyte in electrochemical devices, and the results found in this study can be used to optimise the working efficiency within this electrolyte.

## 5.2 Future Work

The continual rise in popularity of renewable sources as an energy source and their potential to rise above non-renewable sources depends on creating cheap, efficient energy conversion devices. Optimising the operating efficiency of these electrochemical devices is of vital importance. YSZ is a popular electrolyte used for these devices. This study investigated the properties of bulk YSZ and the effect of various surface orientation on the diffusivity properties. There are, however, other factors that can influence the diffusion of YSZ systems, such as introducing strain and the presence of grain boundaries.

The construction of electrochemical diffusion devices will involve the generation of interfaces between different materials, introducing strain into the system. Applying a 4% tensile strain to the $CaF_2$ bulk system resulted in an increase in diffusion coefficient equivalent to an increase in temperature of 150K. One of the drawbacks of using YSZ as the electrolyte in electrochemical devices is the high temperatures required for sufficient oxygen diffusion to occur. It would, therefore, be beneficial to carry out a similar study on the effects of strain on YSZ and compare the results with those within literature [66, 80, 84, 85, 142].

The interfaces between different materials will involve surfaces of these materials, and as a result of lattice mismatch, strain can be introduced into these surfaces. The combinatory effect of surfaces and strain on YSZ will provide a deeper insight into the true mechanism by which diffusion within these devices will occur. Computational modelling allows for the strain effect on different surface orientations to be determined so that the optimum surface orientation with appropriate strain applied can be determined.

The effect of grain boundaries within YSZ has not been investigated in this study, but the examination of $CaF_2$ grain boundaries and YSZ surfaces implies that YSZ grain boundaries will have a significant effect on the diffusion properties of the material. The application of strain to these grain boundaries may also be of benefit when attempting to fully understand the diffusion process. There are a large number of ways in which the diffusion process within multi-crystalline materials can be altered. Only when the presence of these defects on the diffusion of the material is fully understood can the operating efficiency of the electrochemical devices begin to be optimised.

# Bibliography


[1] L. E. Smart and E. A. Moore, *Solid State Chemistry: An Introduction*, Taylor and Francis, 3rd edn., 2005.

[2] A. Dent, P. Madden and M. Wilson, *Solid State Ionics*, 2004, **167**, 73–81.

[3] B. Voronin and S. Volkov, *J. Phys. Chem. Solids*, 2001, **62**, 1349–1358.

[4] A. Ivanov-Shitz, *Physical Properties of Crystals*, 2007, **52**, 129–140.

[5] B. Feng, H. Hojo, T. Mizoguchi, H. Ohta, S. D. Findlay, Y. Sato, N. Shibata, T. Yamamoto and Y. Ikuhara, *Applied Physics Letters*, 2012, **100**, 073109.

[6] H. Hojo, T. Mizoguchi, H. Ohta, S. D. Findlay, N. Shibata, T. Yamamoto and Y. Ikuhara, *Nano Lett*, 2010, **10**, 4668–4672.

[7] W. Tong, H. Yang, P. Moeck, M. Nandasiri and N. Browning, *Acta Mater.*, 2013, **61**, 3392–3398.

[8] B. Feng, I. Sugiyama, H. Hojo, H. Ohta, N. Shibata and Y. Ikuhara, *Scientific Reports*, 2016, **6**, 20288.

[9] E. Dickey, X. Fan and S. Pennycook, *J. Am. Ceram. Soc.*, 2001, **84**, 1361–1368.

[10] T. Arima, K. Fukuyo, K. Idemitsu and Y. Inagaki, *J. Mol. Liq.*, 2004, **113**, 67 – 73.

[11] R. L. González-Romero, J. J. Meléndez, D. Gómez-García, F. L. Cumbrera and A. Domínguez-Rodríguez, *Solid State Ionics*, 2012, **219**, 1–10.

[12] M. Biswas, C. Kumbhar and D. Gowtam, *ISRN Nanotechnology*, 2011, **2011**, year.

[13] C. Zhang, C.-J. Li, G. Zhang, X.-J. Ning, C.-X. Li, H. Liao and C. Coddet, *Mater. Sci. Eng. B*, 2007, **137**, 24–30.

[14] A. Iskandarov and Y. Umeno, *Solid State Ionics*, 2015, **279**, 46 – 52.

[15] *Solid Oxide Fuel Cells: Materials Properties and Performance*, ed. J. W. Fergus, 2009.

[16] J. Conti, P. Holtberg, J. A. Beamon, S. Napolitano, A. M. Schaal, J. T. Turnure and L. Westfall., *International Energy Outlook*, U.S. Energy Information Administration, Washington, DC, 2016.

[17] D. Wuebbles and A. Jain, *Fuel Process. Technol.*, 2001, **71**, 99 – 119.

[18] J. Semanza and B. Menne, *Lancet Infect Dis.*, 2009, **9**, 365 – 375.

[19] S. Shafiee and E. Topal, *Energy Policy*, 2009, **37**, 181 – 189.

[20] D. Brett, A. Atkinson, N. Brandon and S. Skinner, *Chem. Soc. Rev.*, 2008, **37**, 1568–1578.

[21] A. Jacobson, *Chem. Mater*, 2009, **22**, 660–674.

[22] F. M. L. Figueiredo and F. M. B. Marques, *Wiley Interdisciplinary Reviews: Energy and Environment*, 2013, **2**, 52–72.

[23] N. Mahato, A. Banerjee, A. Gupta, S. Omar and K. Balani, *Prog. Mater. Sci.*, 2015, **72**, 141–337.

[24] J. Hansen, *Faraday Discuss*, 2015, **182**, 9 – 48.

[25] N. Baltes, F. Beyle, S. Freiner, F. Geier, M. Joos, K. Pinkwart and P. Rabenecker, *Talanta*, 2013, **116**, 474 – 481.

[26] T. Liu, X. Zhang, Y. L. and J. Yu, *Solid State Ionics*, 2015, **283**, 91–102.

[27] H. Wiemhofer, H. Bremes, U. Nigge and W. Zipprich, *Solid State Ionics*, 2002, **150**, 63 – 77.

[28] R. Ramamoorthy, P. Dutta and S. Akbar, *J. Mater. Sci.*, 2003, **38**, 4271–4282.

[29] G. Korotcenkov, *Mat. Sci. Eng. B*, 2007, **139**, 1 – 23.

[30] M. Buzzeo, C. Hardacre and R. Compton, *Anal. Chem.*, 2004, **76**, 4583–4588.

[31] A. Stambouli and E. Traversa, *Renew. Sust. Energ. Rev.*, 2002, **6**, 433–455.

[32] K. Kawajiri and T. Inoue, *J. Clea. Prod.*, 2016, **112**, 4065–4070.

[33] S. Singhal, *Solid State Ionics*, 2000, **135**, 305–313.

[34] J. Fergus, *J. Power Sources*, 2006, **162**, 30–40.

[35] R. M. Ormerod, *Chem. Soc. Rev.*, 2003, **32**, 17–28.

[36] S. Badwal, *Solid State Ionics*, 2001, **143**, 39–46.

[37] L. J. Clark, R. Wolf, D. Granger and T. Z., *J Appl Physiol.*, 1953, **6**, 189–193.

[38] J. Riegel, H. Neumann and H. Wiedenmann, *Solid State Ionics*, 2002, **152**, 783 – 800.

[39] S. Elliott, *The Physics and Chemistry of Solids*, Wiley, 1998.

[40] G. Prabhatasree, N. Choudhury and S. Chaplot, *Transactions of the Indian Institute of Metals*, **62**, 141 – 147.

[41] S. Tsurekawa, T. Tanaka and H. Yoshinaga, *Mat. Sci. Eng. A-Struct.*, 1994, **176**, 341–348.

[42] M. Ladd, *Bonding, Structure and Solid-State Chemistry*, Oxford University Press, 2016.

[43] R. Tilley, *Defects in Solids*, John Wiley & Sons, 2008.

[44] C. Kittel, *Introduction to Solid State Physics*, Wiley, 8th edn., 2005.

[45] F. Kröger and H. Vink, *Relations between the Concentrations of Imperfections in Crystalline Solids*, Academic Press, 1956, vol. 3.

[46] H. Mehrer, *Diffusion in Solids*, Springer, 2007.

[47] M. Burbano, S. Nadin, D. Marrocchelli, M. Salanne and G. W. Watson, *Phys. Chem. Chem. Phys.*, 2014, **16**, 8320–8331.

[48] J. Hook and H. Hall, *Solid State Physics*, John Wiley & Sons, 2nd edn., 1974.

[49] H. Fredriksson and U. Akerlind, *Physics of Functional Materials*, Wiley, 2008.

[50] E. M. McCash, *Surface Chemistry*, Oxford University Press, 2001.

[51] W. Zhang, *J. Cryst. Growth*, 2006, **297**, 169–179.

[52] G. Somorjai and Y. Li, *Surface Chemistry and Catalysis*, Wiley, 2nd edn., 2010.

[53] P. W. Tasker, *J. Phys. C: Solid State Phys.*, 1979, **12**, 4977–4984.

[54] F. Bertaut, *Compt. Rendu.*, 1958, **246**, 3447.

[55] S. Parker, P. Lawrence, C. Freeman, S. Levine and J. Newsam, *Catal. Lett.*, 1992, **15**, 123–131.

[56] M. Abramowski, S. Redfern, R. Grimes and S. Owens, *Surf. Sci.*, 2001, **490**, 415–420.

[57] M. Abramowski, R. Grimes and S. Owens, *J. Nucl. Mater.*, 1999, **275**, 12–18.

[58] S. Vyas, R. Grimes, D. H. Gay and A. L. Rohl, *J. Chem. Soc., Faraday Trans.*, 1998, **94**, 427–434.

[59] J. Harding, *Computer Modelling in Inorganic Crystallography*, Academic Press, 1997.

[60] N. Ashcroft and N. Mermin, *Solid State Physics*, Harcourt College Publishers, 1976.

[61] D. Duffy, *J. Phys. C: Solid State Phys.*, 1986, **19**, 4393–4412.

[62] M. Kronberg and F. Wilson, *T. Am. I. Min. Met. Eng.*, 1949, **185**, 501–514.

[63] N. Fletcher, *Crystal interface models – a critical survey, in Advances in Materials Research*, Wiley, New York, 5th edn., 1971.

[64] N. Williams, M. Molinari, S. Parker and M. Storr, *J. Nucl. Mater.*, 2014, **458**, 45–55.

[65] L. Van Brutzel and E. Vincent-Aublant, *J. Nucl. Mater.*, 2008, **377**, 522–527.

[66] K. Wen, W. Lv and W. He, *J. Mater. Chem. A.*, 2015, **3**, 20031 – 20050.

[67] M. Rushton, A. Chroneos, S. Skinner, J. Kilner and R. Grimes, *Solid State Ionics*, 2013, **230**, 37–42.

[68] W. Araki, M. Kuribara and Y. Arai, *Solid State Ionics*, 2011, **193**, 5 – 10.

[69] A. Fick, *Phil. Mag. and Jour. Sci.*, 1855, **10**, 31 – 39.

[70] R. Brown, *Phil. Mag.*, 1828, **4**, 161.

[71] A. Einstein, *Ann. Phys.*, 1905, **17**, 549.

[72] C. Wert and C. Zener, *Phys. Rev.*, 1949, **76**, 1169–1175.

[73] S. Bukkuru, M. Warrier and A. Rao, AIP Conference Proceedings, 2015.

[74] K. Vieregge and C. Herzig, *J. Nucl. Mater.*, 1990, **175**, 29–41.

[75] G. Gilmer and H. Farrell, *J. Appl. Phys.*, 1976, **47**, 4373–4380.

[76] L. Luther, *J. Chem. Phys.*, 1965, **43**, 2213–2218.

[77] R. De Souza, M. Pietrowski, U. Anselmi-Tamburini, S. Kim, Z. A. Munir and M. Martin, *Phys. Chem. Chem. Phys.*, 2008, **10**, 2067–2072.

[78] G. Knöner, K. Reimann, R. Roewer, U. Soedervalland and H. Schaefer, *Proc. Natl. Acad. Sci. U.S.A.*, 2003, **100**, 3870 – 3873.

[79] W. Shen and J. Hertz, *J. Mater. Chem. A*, 2015, **3**, 2378 – 2386.

[80] M. Oka, H. Kamisaka, T. Fukumura and T. Hasegawa, *Phys. Chem. Chem. Phys.*, 2015, **17**, 29057–29063.

[81] G. Dezanneau, J. Hermet and B. Dupe, *Int. J. Hydrogen Energy*, 2012, **37**, 8081 – 8086.

[82] W. Araki and Y. Arai, *Solid State Ionics*, 2011, **190**, 75 – 81.

[83] R. De Souza, A. Ramadan and S. Horner, *Energy Environ. Sci*, 2012, **5**, 5445–5453.

[84] M. Burbano, D. Marrocchelli and G. Watson, *J. Electroceram.*, 2013, **32**, 28–36.

[85] W. Lv, N. Feng, Y. Niu, F. Yang, K. Wen, M. Zou, Y. Han, J. Zhao and W. He, *Solid State Ionics*, 2016, **289**, 168–172.

[86] K. Wen, K. Zhang, W. Wang, J. Lin, W. Lv, B. Wang, Z. Wang, J. Dickerson, X. Guo and W. He, *J, Power Sources*, 2015, **285**, 37–42.

[87] J. Garcia-Barriocanal, A. Rivera-Calzada, M. Varela, Z. Sefrioui, E. Iborra, C. Leon, S. Penneycook and J. Santamaria, *Science*, 2008, **321**, 676–680.

[88] T. Pennycook, M. Varela, M. Beck, J. Garcia-Barriocanal, F. Bruno, C. Leon, J. Santamaria, S. Pantelides and S. Pennycook, *Microsc. Microanal.*, 2010, **16**, 100–101.

[89] D. Pergolesi, E. Fabbri, S. Cook, V. Roddatis, E. Traversa and J. Kilner, *ACS Nano*, 2012, **6**, 10524–10534.

[90] A. Kushima and B. Yildiz, *J. Mater. Chem.*, 2010, **20**, 4809–4819.

[91] B. Alder and T. Wainwright, *J. Chem. Phys.*, 1957, **27**, 1208–1209.

[92] B. Alder and T. Wainwright, *J. Chem. Phys.*, 1959, **31**, 459–466.

[93] M. J. Castiglione, M. Wilson and P. A. Madden, *J. Phys.: Condens. Matter*, 1999, **11**, 9009.

[94] P. P. Ewald, *Ann. Phys.*, 1921, **369**, 253–287.

[95] A. Y. Toukmaji and J. A. B. Jr., *Comput. Phys. Commun.*, 1996, **95**, 73 – 92.

[96] N. Wilson, M. Wilson, P. Madden and M. Pyper, *J. Chem. Phys.*, 1996, **105**, 11209–11219.

[97] N. Pyper, *J. Phys.: Condens. Matter*, 1995, **7**, 9127–9145.

[98] H. Yukawa, *Proc. Phys. Math. Soc. Jpn.*, 1935, **17**, 48–57.

[99] D. Marrocchelli, M. Salanne, P. Madden, C. Simon and P. Turq, *Mol. Phys.*, 2009, **107**, 443–452.

[100] K. T. Tang and J. P. Toennies, *J. Chem. Phys.*, 1984, **80**, 3726–3741.

[101] A. D. Buckingham, *Adv. Chem. Phys.*, 1967, **12**, 107.

[102] P. Madden and M. Wilson, *Chem. Soc. Rev.*, 1996, **25**, 339–350.

[103] M. Hestenes and E. Stiefel, *J. Res. Nat. Bur. Stand.*, 1952, **49**, 409–436.

[104] L. Verlet, *Physical Review*, 1967, **159**, year.

[105] L. Verlet, *Physical Review*, 1968, **165**, 201 – 214.

[106] M. P. Allen and D. J. Tildesley, *Computer Simulation of Liquids*, Oxford University Press, 1989.

[107] G. Martyna, D. Tobias and M. Klein, *J. Chem. Phys.*, 1994, **10**, 4177–4189.

[108] J. W. Gibbs, *Elementary principles in statistical mechanics*, Charles Scribner's Sons, 1902.

[109] W. Smith and M. Gillan, CCP5 Newsletter, 1996, pp. 61–71.

[110] H. Brinkman, W. Briels and H. Verweij, *Chem. Phys. Lett.*, 1995, **247**, 386–390.

[111] G. Murch, *Solid State Ionics*, 1982, **7**, 177–198.

[112] N. Dudney, W. West and J. Nanda, *Materials and Energy: Handbook of Solid State Batteries*, World Scientific, 2nd edn., 2015, vol. 6.

[113] R. Ure, *J. Chem. Phys.*, 1957, **26**, 1363–1373.

[114] E. Barsis and A. Taylor, *J. Chem. Phys.*, 1966, **45**, 1154–1162.

[115] H. Matzke, *J Mater Sci*, 1970, **5**, 831–836.

[116] A. Rahman, *J. Chem. Phys.*, 1976, **65**, 4845–4848.

[117] G. Farrington and J. Briant, *Fast Ion Transport in Solids*, 1979.

[118] P. Cheeseman and C. Angell, *Solid State Ionics*, 1981, **5**, 597–600.

[119] M. Gillan, *Physica B*, 1985, **131**, 157–174.

[120] C. Catlow and M. Norgett, *J. Phys. C: Solid State Phys.*, 1973, **6**, 1325–1339.

[121] G. Jacucci and A. Rahman, *J. Chem. Phys.*, 1978, **69**, 4117–4125.

[122] G. Evangelakis and V. Pontikis, *Phys. Rev. B*, 1991, **43**, 3180–3187.

[123] M. Dixon and M. Gillan, *J. Phys. C: Solid State Phys.*, 1978, **11**, 165 – 169.

[124] W. Puin, S. Rodewald, R. Ramlau, P. Heitjans and J. Maier, *Solid State Ionics*, 2000, **131**, 159 – 164.

[125] P. Nerikar, C. Stanek, S. Phillpot, S. Sinnott and B. Uberuaga, *Phys. Rev. B*, 2010, **81**, 064111.

[126] C. Maunier and V. Pontikis, *Colloque De Physique*, 1990, **51**, 245–250.

[127] P. Nerikar, K. Rudman, T. Desai, D. Byler, C. Unal, K. McClellan, S. Phillpot, S. Sinnott, P. Peralta, B. Uberuaga and C. R. Stanek, *J. Am. Ceram. Soc.*, 2011, **94**, 1893–1900.

[128] K. Govers and M. Verwerft, *J. Nucl. Mater.*, 2013, **438**, 134–143.

[129] N. Shibata, F. O. O. Yamamoto and Y. Ikuhara, *Philos. Mag.*, 2004, **84**, 2381–2415.

[130] C. Fisher and H. Matsubara, *J. Eur. Ceram. Soc.*, 1999, **19**, 703–707.

[131] Y. Lei, Y. Ito, N. Browning and T. Mazanec, *J. Am. Ceram. Soc.*, 2002, **85**, 2359–2363.

[132] A. Marinopoulos, *J. Phys.: Condens. Matter*, 2011, **23**, 1–8.

[133] G. W. Watson, E. T. Kelsey, N. H. de Leeuw, D. J. Harris and S. C. Parker, *J. Chem. Soc., Faraday Trans.*, 1996, **92**, 433–438.

[134] G. Watson, *Ph.D. thesis*, Bath University, 1994.

[135] B. Schumann and H. Neumann, *Cryst. Res. Technol.*, 1984, **19**, 13–14.

[136] V. Kuzmin, G. Ivanova, O. Morozova and B. Savchenko, *Izmerit. Tekhn.*, 1979, **8**, 48.

[137] S. Sharma, *Proc. Indian Acad. Sci. A*, 1950, **31**, 261.

[138] T. Radhakrishnan, *Proc. Indian Acad. Sci. A*, 1951, **33**, 22.

[139] D. Sirdeshmukh and V. Deshpande, *Indian J. Pure Appl. Phys.*, 1964, **2**, 405.

[140] C. Catlow, J. Comins, F. Germano, R. Harley, W. Hayes and I. Owen, *J. Phys. C: Solid State Phys.*, 1981, **14**, 329–335.

[141] P. Lindan and M. Gillan, *J. Phys.: Condens. Matter*, 1991, **3**, 3929–3939.

[142] A. Tarancón and A. Morata, *Comput. Mater. Sci.*, 2015, **103**, 206–215.

[143] P. Maldonado, J. Godinho, L. Evins and P. Oppeneer, *J. Phys. Chem. C*, 2013, **117**, 6639–6650.

[144] V. Puchin, A. Puchina, M. Huisinga and M. Reichling, *J. Phys.: Condens. Matter*, 2001, **13**, 2081–2094.

[145] J. Conesa, *Surf. Sci.*, 1995, **339**, 337–352.

[146] Y. Jiang, J. B. Adams and M. van Schilfgaarde, *J. Chem. Phys.*, 2005, **123**, 064701.

[147] P. Dholabhai, J. Aguiar, L. Wu, T. Holesinger, T. Aoki, R. Castro and B. Uberuaga, *Phys. Chem. Chem. Phys*, 2015, **17**, 15375–15385.

[148] F. Yuan, B. Liu, Y. Zhang and W. Weber, *J. Phys. Chem.*, 2016, **120**, 6625–6632.

[149] M. Yoshiya and T. Oyama, *J. Mater. Sci.*, 2011, **46**, 4176–4190.

[150] Y. Ikuhara, *J Electron Microsc*, 2011, **60**, S173–S188.

[151] J. Dawson and I. Tanaka, *J. Mater. Chem. A*, 2014, **2**, 1400–1408.

[152] D. Wolf, *Philos. Mag. A.*, 1984, **49**, 823–844.

[153] S. Badwal, *Solid State Ionics*, 1992, **52**, 23–32.

[154] H. Scott, *J. Mater. Sci.*, 1975, **10**, 1527 – 1535.

[155] V. Stubican, R. Hink and S. Ray, *J. Am. Ceram. Soc.*, 1978, **61**, 17 – 21.

[156] J. R. Kelly and I. Denry, *Dent. Mater.*, 2008, **24**, 289–298.

[157] R. Devanathan, W. Weber, S. Singhal and J. Gale, *Solid State Ionics*, 2006, **177**, 1251 – 1258.

[158] N. Padture, M. Gell and E. Jordan, *Science*, 2002, **296**, 280.

[159] V. Kharton, E. Naumovich and A. Vecher, *J. Solid State Electrochem.*, 1999, **3**, 61–81.

[160] A. Nakamura and J. W. Jr., *The Electrochemical Society*, 1986, **133**, 1542–1548.

[161] Y. Arachi, H. Sakai, O. Yamamoto, Y. Takeda and N. Imanishai, *Solid State Ionics*, 1999, **121**, 133 – 139.

[162] M. Kilo, C. Fundenberger, C. Argirusis, A. Taylor, G. Borchardt, M. Weller and R. A. Jackson, *Radiat. Eff. Defects Solids*, 2002, **157**, 1077 – 1083.

[163] F. Shimojo, T. Okabe, F. Tachibana, M. Kobayashi and H. Okazaki, *J. Phys. Soc. Jpn.*, 1992, **61**, 2848–2857.

[164] M. Kilo, C. Argirusis, G. Borchardt and R. A. Jackson, *Phys. Chem. Chem. Phys.*, 2003, **5**, 2219 – 2224.

[165] A. Bogicevic and C. Wolverton, *Phys. Rev. B*, 2003, **67**, 024106.

[166] G. Stapper, M. Bernasconi, N. Nicoloso and M. Parrinello, *Phys. Rev. B*, 1999, **59**, 797 – 810.

[167] P. Li, I. Chen and J. Penner-Hahn, *Phys. Rev. B.*, 1993, **48**, 10074 – 10081.

[168] C. Catlow, A. Chadwick, G. Greaves and L. Moroney, *J. Am. Ceram. Soc.*, 1986, **69**, year.

[169] M. Cole, C. Catlow and J. Dragun, *J. Phys. Chem. Solids*, 1990, **51**, 507 – 513.

[170] P. Dalach, D. Ellis and A. van de Walle, *Phys. Rev. B*, 2010, **82**, 144117.

[171] M. Khan, M. Islam and D. Bates, *J. Mater. Chem.*, 1998, **8**, 2299 – 2307.

[172] X. Xia, R. Oldman and R. Catlow, *Chem. Mater.*, 2009, **21**, 3576–3585.

[173] G. Balducci, J. Kaspar, P. Fornasiero, M. Graziani and M. Islam, *J. Phys. Chem. B*, 1998, **102**, 557 – 561.

[174] H. Hayashi, T. Saitou, N. Maruyama, H. I. I. Kawamura and M. Mori, *Solid State Ionics*, 2005, **176**, 613 – 619.

[175] R. Shannon, *Acta Crystallogr. A*, 1976, **32**, 751 – 767.

[176] S. V. Ushakov, A. Navrotsky, R. Weber and J. Neuefeind, *J. Am. Ceram. Soc.*, 2015, **98**, 3381 – 3388.

[177] E. Kisi and C. Howard, *J. Am. Ceram. Soc.*, 1998, **81**, 1682 – 1684.

[178] M. Ezersky, I. Kozlova, R. Popilsky and I. Demonis, *Neorg. Mater.*, 1968, **4**, 1599.

[179] E. Lukin, A. Borovkova and E. Khudak, *Neorg. Mater.*, 1974, **10**, 1911.

[180] E. Keler and A. Andreeva, *Ogneupory*, 1963, **5**, 224.

[181] K. Lau and B. Dunlap, *J. Phys.: Condens. Matter*, 2011, **23**, 035401.

[182] S. Hull, *Rep. Prog. Phys.*, 2004, **67**, 1233 – 1314.

[183] J. Kondoh, S. Kikuchi, Y. Tomii and Y. Ito, *J. Electrochem. Soc.*, 1998, **145**, 1527 – 1536.

[184] J. Kondoh, S. Kikuchi, Y. Tomii and Y. Ito, *J. Electrochem. Soc.*, 1998, **145**, 1550 – 1560.

[185] R. Pornprasertsuk, P. Ramanarayanan, C. B. Musgrave and F. B. Prinz, *J. Appl. Phys.*, 2005, **98**, year.

[186] M. Sakib Khan, M. Saiful Islam and D. R. Bates, *J. Mater. Chem.*, 1998, **8**, 2299–2307.

[187] C. Yang, W. Wei and A. Roosen, *Materials Chemistry and Physics*, 2003, **81**, 134 – 142.

[188] P. Manning, J. Sirman, R. D. Souza and J. Kilner, *Solid State Ionics*, 1997, **100**, 1–10.

[189] P. Manning, J. Sirman and J. Kilner, *Solid State Ionics*, 1996, **93**, 125–132.

[190] H. Solomon, C. Monty, M. Filal, G. Petot-Ervas and C. Petot, *Solid State Phenomena*, 1995, **41**, 103 – 112.

[191] M. O. Zacate, L. Minervini, D. J. Bradfield, R. W. Grimes and K. E. Sickafus, *Solid State Ionics*, 2000, **128**, 243–254.

[192] H. Lee, F. Prinz and W. Cai, *Acta Mater.*, 2010, **58**, 2197 – 2206.

[193] K. Kawata, H. Maekawa, T. Nemoto and T. Yamamura, *Solid State Ionics*, 2006, **177**, 1687 – 1690.

[194] D. Marrocchelli, P. A. Madden, S. T. Norberg and S. Hull, *Chem. Mater.*, 2011, **23**, 1365–1373.

[195] M. Burbano, S. T. Norberg, S. Hull, S. G. Eriksson, D. Marrocchelli, P. A. Madden and G. W. Watson, *Chem. Mater.*, 2012, **24**, 222–229.

[196] S. Hull, S. T. Norberg, I. Ahmed, S. G. Eriksson, D. Marrocchelli and P. Madden, *J. Solid State Chem.*, 2009, **182**, 2815 – 2821.

[197] C. Gopal and A. van de Walle, *Phys. Rev. B*, 2012, **86**, year.

[198] S. T. Norberg, S. Hull, I. Ahmed, S. G. Eriksson, D. Marrocchelli, P. Madden, P. Li and J. Irvine, *Chemistry of Materials*, 2011, **23**, 1356–1364.

[199] D. Marrocchelli, P. Madden, S. Norberg and S. Hull, *J. Phys.: Condens. Matter*, 2009, **21**, year.

[200] M. Parkes, D. Tompsett, M. d'Avezac, G. Offer, N. Brandon and N. Harrison, *Phys. Chem. Chem. Phys.*, 2016, **18**, year.

[201] F. Pietrucci, M. Bernasconi, A. Laio and M. Parrinello, *Phys. Rev. B*, 2008.

[202] G. Ballabio, M. Bernasconi, F. Pietrucci and S. Serra, *Phys. Rev. B*, 2004, **70**, year.

[203] V. Sizov, M. Lampinen and A. Laaksonen, *Solid State Ionics*, 2014, **266**, 29 – 35.